Doctoral Dissertation
博士論文

Helicity dependent photocurrent in strong spin-orbit coupling materials

(強いスピン軌道相互作用を持つ物質におけるヘリシティ依存光電流)

A Dissertation Submitted for the Degree of Doctor of Philosophy, July 2020
令和2年7月博士(理学)申請

Department of Physics, Graduate School of Science,
The University of Tokyo
東京大学大学院理学系研究科物理専攻

FAN DI
樊　締

Abstract

Spintronics, in which the spin degree of freedom of electrons is used for various functions, is a booming field of research in recent decays. With the new knowledge of the strong spin-orbit coupling (SOC) materials, the research has been focused on injecting, manipulating and detecting spin in these new playgrounds. Recent discovery of topological insulators (TIs) further promotes the developments of spintronics in strong spin-orbit coupling materials. Besides the developments of spintronics in materials aspect, new techniques using optical angular momentum for manipulating spin of electrons are also a great advance in the field. Compared with conventional electrical methods for spin manipulation, optical approaches could provide remote and contact-free spin injection and manipulation. Especially, the combination of optical angular momentum and TIs draws lots of attentions on the helicity dependent photocurrent (HDP), a new way to produce non-reciprocal photocurrent. It is said that HDP is spin-polarized and could be controlled by experimental scheme such as polarization, wavelength, and angle of incidence of illumination light. This special phenomenon not only provides a new possibility for device applications but also opens up a new way for the study of topological surface states (TSSs).

We study the HDP in strong spin-orbit coupling materials in this thesis. We first show that silicon, as a material with weak spin-orbit interaction, exhibits no HDP as expected. Then we investigate thin films of well-studied topological insulator Bi_2Se_3. With our *in-situ* growth/measurement system in ultrahigh vacuum, we have demonstrated that the HDP in Bi_2Se_3 films is strongly related with the TSSs under illumination of light certain wavelength. HDP that contains circular photogalvanic effect (CPGE) and circular photon drag effect (CPDE) mechanisms is observed in this experiment. HDP due to CPGE is generally believed to be related with the asymmetric excitation at spin splitting bands due to selection rules, which would generate a spin-polarized photocurrent as a result. However, HDP due to CPDE is not necessarily generated from exciting electrons in spin splitting bands, because even the excitation in the spin degenerate bands the momentum transfer from photons will lead to an asymmetric distribution of excited carriers in k space and results in a photocurrent. In addition, HDP reveals different properties depending on the experimental geometry and illumination wavelength, but not all of them are related with the spin manipulation. With further investigation of the HDP at oblique incidence on thickness dependence of the Bi_2Se_3 film, we found that HDP originated from CPGE changed its sign when the thickness of the Bi_2Se_3 film increased from 4 QL to 7 QL. We believe this observation suggests that HDP from CPGE is strongly related with TSSs of Bi_2Se_3, and the HDP due to CPGE would reverse the flowing direction when TSSs evolving from Rashba surface states to helical Dirac cone surface states. When the TSSs evolves from Rashba states to a helical Dirac cone surface states, the outer subband of the Rashba states is gone. With the same spin injected into this system by a circularly polarized photon, the dominating band of the spin-to-charge conversion changes from the outer Rashba band to inner Rashba band. Therefore this reversing of HDP is inevitable when the HDP originate from TSSs. Moreover, we observed an HDP at the edge of the sample under normal incidence. Normally, CPGE or CPDE mechanism are forbidden by the symmetry of Bi_2Se_3. The HDP we observed at the edge of the sample is due to the inverse spin Hall effect (ISHE) acting on

the out-of-plane spin component which is excited by a circularly polarized light at normal incidence. With finite element method simulation, we understand that an electric dipole is formed at the edge due to the charge accumulation by the current of ISHE, and it is this dipole potential that causes the HDP we measured. By shinning the opposite edge of the sample, an electrical dipole with opposite polarity is generated, and the HDP flows in opposite direction.

Next, we have shown the HDP is also observed in Bi(111) films, a trivial but strong SOC material, though the outcome is not as promising as in Bi_2Se_3 films in the aspect of spin manipulation and the intensity of HDP. CPDE rather than CPGE is responsible for the HDP we observed at 635 nm illumination. The high extinction coefficient of bismuth is very high especially at long wavelength. As a result, we almost observe no photocurrent at 1550 nm illumination. This result suggests that though heavy metals also possess strong SOC, the high extinction coefficient will make the light absorption in them very difficult, thus they are not good candidates for the optical spin orientation. Finally, we examined a series of TIs, $(Bi_xSb_{1-x})_2Te_3$, in which the Fermi level position can be tuned by changing the Bi and Sb compounds ratio. CPGE and CPDE mechanisms are also observed to be responsible for the generation of the HDP. We find that HDP is strongly influenced by the Fermi level position at 1550 nm, however, does not change much at 635 nm. This result further supports the conclusion that HDP could be related with TSSs of the TI at certain wavelength. HDP at normal incidence is also observed in this experiment, but only the bulk insulating sample exhibits such phenomenon. Similar to the case in Bi_2Se_3, we believe that ISHE is the explanation for the HDP at normal incidence. Moreover, we found that HDP due to ISHE is more sensitive to Fermi level position than HDP of CPGE, this is probably due to the fact that out-of-plane spin component only exists at the position far from the Dirac point of TSSs but in-plane spin generally exists in a wide energy range of the helical Dirac cone.

Through the whole study, we conclude that HDP generally exists in materials with strong SOC, but the HDP shows different properties, is originated from different mechanisms, and depends on the specific experimental arrangements. These findings suggest that we need to be careful when concluding the mechanism and origin of the HDP. In addition, TIs show better responds to the circularly polarized light than normal materials in the aspect of HDP which related with the complex spin texture of the materials. We have observed the HDP due to CPGE at all our TI samples at 1550 nm illumination but not on bismuth. Moreover, HDP due to CPGE in TIs could indeed reveal the TSSs feature of TIs. Both the thickness dependence and the Fermi level position dependence experiments suggest that HDP is related with TSSs of TIs, and the variation of such HDP could even reveal the evolution of the TSSs. Besides, out-of-plane spin component can be injected into TIs by optical methods when hexagonal warping effect occurs. With the conclusion that we previous have, HDP of 1550 nm is related with TSSs, and we can conclude that hexagonal warping part of the TSSs could be the origin of the out-of-plane spin. Our study proves several speculations in the field, and our new finding may initiate new applications or researches for spintronics.

Abbreviation list

ACPGE	Anomalous Circular Photogalvanic Effect
AOI	Angle of Incidence
ARPES	Angle Resolved Photoemission Spectroscopy
BCB	Bulk Conduction Band
BL	Bilayer
BVB	Bulk Valence Band
CD	Circular Dichroism
CPDE	Circular Photon Drag Effect
CPGE	Circular Photogalvanic Effect
HDP	Helicity-dependent Photocurrent
IREE	Inverse Rashba-Edelstein Effect
ISHE	Inverse Spin Hall Effect
LCP	Left-handed Circular Polarization
LPDE	Linear Photon Drag Effect
LPGE	Linear Photogalvanic Effect
LEED	Low-Energy Electron Diffraction
MBE	Molecular Beam Epitaxy
ML	Monolayer
NIR	Near Infrared
PDE	Photon Drag Effect
PGE	Photogalvanic Effect
QL	Quintuple Layer
QWP	Quarter Waveplate
RCP	Right-handed Circular Polarization
RHEED	Reflection High-Energy Electron Diffraction
RT	Room Temperature
SGE	Spin Galvanic Effect
SHE	Spin Hall Effect
SHG	Second Harmonic Generation
SIA	Space Inversion Asymmetric
SIS	Space Inversion Symmetry
SOC	Spin-orbit Coupling
SOI	Spin-orbit Interaction
SR	Surface Resonance
SRARPES	Spin Resolved Angle Resolved Photoemission Spectroscopy
SS	Surface State
TI	Topological Insulator
TRIM	Time Reversal-invariant Momenta
TRS	Time Reversal Symmetry
TSS	Topological Surface State
UHV	Ultra-high Vacuum
2DEG	Two-Dimensional Electron Gas
2PP	Two Photon Photoemission

Contents

Chapter 1

Introduction

1.1 Research background

1.1.1 Strong spin-orbit coupling materials

When we carefully examine the red spectral line of the hydrogen spectrum, we can find a closely spaced doublet. This is the well-known fine structure and is one of the first experimental evidences for electron spin. Following the Bohr Theory, we could easily calculate the wavelength of 656.47 nm for this red spectrum line, a.k.a. the H-alpha line. However, we could not get the explanation for the splitting unless we take the interaction between electron spin and its orbital motion into account. This is when the spin-orbit interaction (SOI, or spin-orbit coupling SOC) beginning to draw people's attention. Such interaction is weaker than the Columb interaction yet has a great ability to modify materials' physical properties.

After decades of research, researchers realize that in low dimensional materials spin possesses better characters than charges in aspects of coherency and dissipation. This motivates pioneers to set off new techniques for device applications, i.e. manipulating spin degree of freedom, which leads to the newly raising field: spintronics[1, 2]. Spintronics is the study of spin manipulation, transportation and spin-charge interconversion to realize spintronic devices and the quantum computer. The famous spin field effect transistor, as shown in Fig.1.1 proposed by Datta and Das [3] shows one of the basic concepts of spintronic devices.

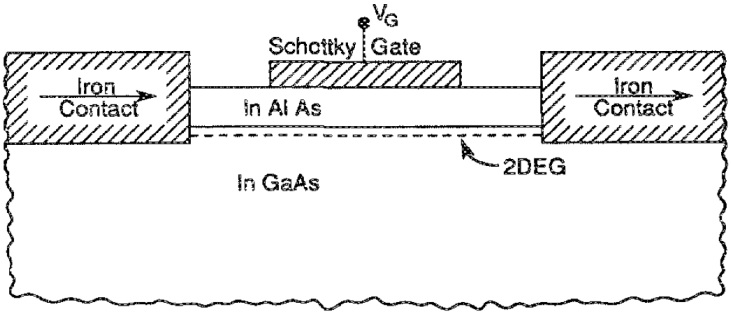

Figure 1.1: Concept of a spin field effect transistor (FET) based on Rashba SOC, figure is extracted from ref.[3]. Two iron contacts act as polarizer (left) and analyzer (right) individually. A Schottky gate is used to modulate the spin-orbit-coupling constant of the two-dimensional electron gas (2DEG), which will shift the phase of the injected spin. As a result, spin detected at the analyzer and the resulting current are controlled by the gate.

As shown in the conceptual model, SOC is the key feature to manipulate spin, by simply applying an external electric field to tune the strength of the SOC. Materials that possess Rashba or Dresselhaus SOC are the crucial ingredients for the spin FET. Recently, a new topological phase of matters, topological insulator (TI) [4] has been discovered. This topological phase is also induced by SOC and exhibiting extraordinary properties which are promising for device applications.

For a certain material, gapped band structures can be classified topologically by considering the equivalence classes of their Bloch Hamiltonian $H(\mathbf{k})$ that can be continuously deformed into one another without closing the energy gap [5]. These classes are distinguished by a topological invariant $n \in \mathbb{Z}$ ($\mathbb{Z}$ denotes the integers) called the Chern invariant, or Chern number which is closely related to Berry's phase. The SOI allows a different topological class, $\mathbb{Z}_2$, with an insulating band structures when the time reversal symmetry (TRS) holds [6].

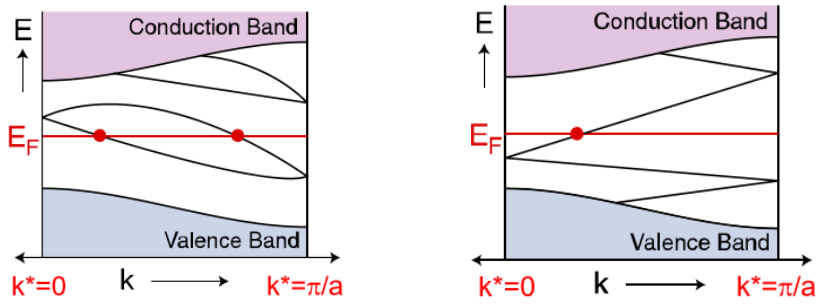

Figure 1.2: Fermi level crossover, figures are from ref.[5]. (a) Even number of interceptions infers topologically trivial; (b) odd number of interceptions infers topologically nontrivial.

Intense attention has been focused on this new kind of materials soon af-

ter the first theoretical prediction [7] and experimental realization of a 2D TI in HgTe/CdTe quantum wells [8]. Due to scattering events, conventional materials face the energy dissipation during carrier transport process. However, 2D TIs contain 1D edge states, which are protected by TRS could prohibit backscattering. This property signals that TIs could be used as low dissipation devices. Other characters of TIs such as the insulating bulk with a metallic surface, highly spin polarized and spin-momentum locked surface states and its robustness against impurities, suggest that TIs may surpass ordinary materials in the device application of spintronics.

1.1.2 Photocurrent

Photocurrent is the generation of an electric current by a light illumination. It is mostly generated with the help of an internal electric field which resides in a heterojunction. In addition, photocurrent can be created when asymmetric distribution of photoexcited carriers are produced by means of photon momentum transfer and asymmetric scattering, relaxation or excitation.

Presence of the SOC in materials gives a chance of the asymmetric excitation by circularly polarized illumination. Taking into account of the innegligible SOC would modify the normal dipole selection rules to new so-called relativistic dipole selection rules which describe the spin dependent transition by circular polarization. The circularly polarized photon can couple to the spin degree of freedom of electrons via total angular momentum [9]. This spin selective excitation opens up the opportunity for optical spin orientation. Many pioneer works have been done to use circularly polarized light to inject spin into materials [10].

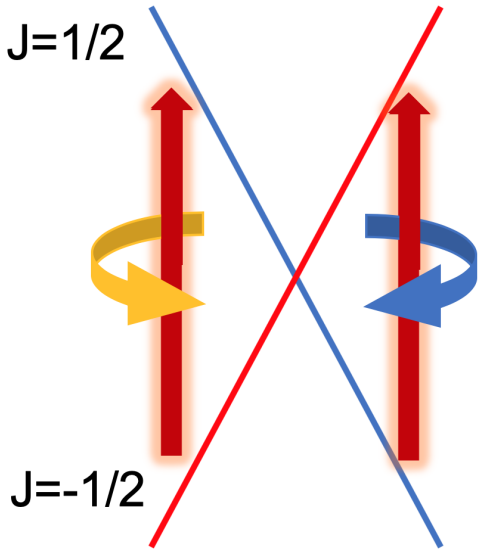

Figure 1.3: Spin selective excitation by circularly polarized light. Certain helicity could excite one branch of the topological surface states (TSSs) only because of the helical spin structure, the asymmetric distribution of carries in the momentum space will lead to a zero-bias photocurrent. The direction of the photocurrent is determined by the spin via the spin-momentum locking TSSs.

Moreover, spin-momentum locking bands in TIs and Rashba SOC could further ensures that photocurrent with the same spin flows in unanimous direction, i.e. spin polarized current can be generated. When we shine circularly polarized light onto a sample such as quantum wells with SOI [11, 12], topological insulators [13, 14] and spin-valley coupling systems [15, 16], a zero bias current can be induced. This phenomenon of current generation by circularly polarized light is usually ascribed to so-called circular photogalvanic effect (CPGE), a branch of photogalvanic effect (PGE) [17]. Such mechanism enables the light helicity $\rightarrow$ spin $\rightarrow$ charge current control chain which is a straightforward process for spintronics, since it fulfills the spin detection and manipulation at the same time.

However, there are some disagreements among those previous researches. The phenomenological theory of CPGE is well established, so for a sample with a certain symmetry the photocurrent behaviors can be predicted by the CPGE theory. For example, the incident angle (θ) dependence of the CPGE photocurrent for a crystal with C_{3v} symmetry should behave as a function of $\sin 2\theta$ as shown in Fig. 1.4(a). However, there are some researches claim the HDP they observed to be CPGE even the incident angle dependence is clearly not to be $\sin 2\theta$ with the sample of C_{3v} symmetry. Some even hastily claim that the HDP they observed to be CPGE without further investigation. It needs to mention that other mechanisms, like circular photon drag effect (CPDE), can also contribute to the HDP. In addition, the CPDE has a weaker symmetry requirement and can even exist in materials without strong SOC.

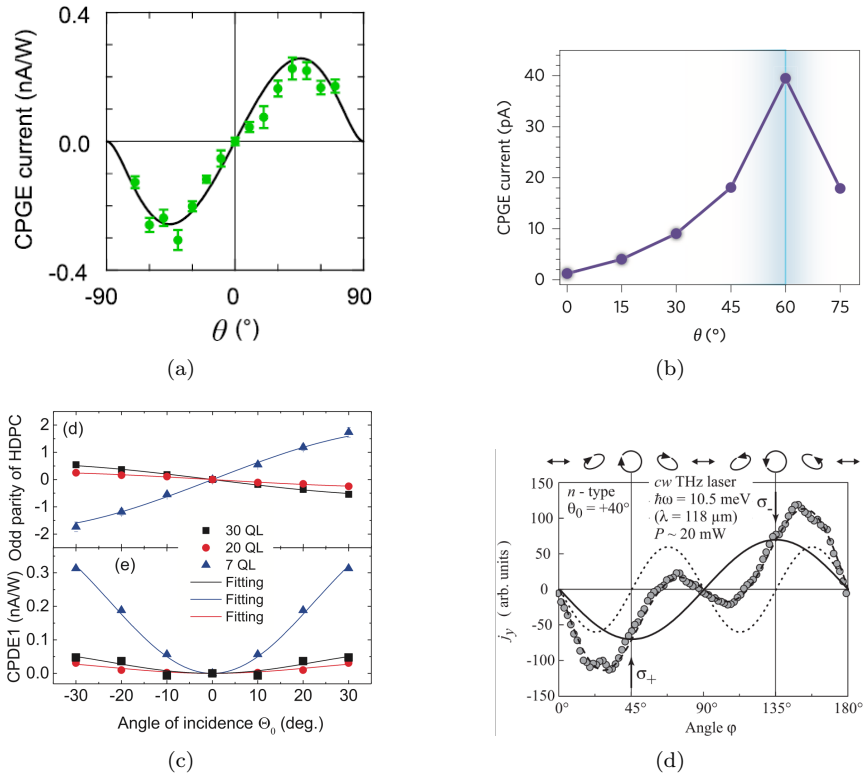

Figure 1.4: (a) Typical incident angle dependence of the CPGE HDP for a $(Bi_{0.16}Sb_{0.84})_2Te_3$ with C_{3v} symmetry, figure is acquired from ref.[14]. (b) Incident angle dependence of the claimed CPGE HDP in WSe_2, figure is acquired from ref.[11]. Though WSe_2 also shows C_{3v} symmetry, the incident angle dependence deviates from the $\sin 2\theta$ shape as in (a). (c) Incident angle dependence of the CPDE HDP observed in Sb_2Te_3, which is also C_{3v} symmetry, the incident angle dependence is symmetrical to 0° incidence, figure is acquired from ref.[18]. It can be seen that the incident angle dependence of WSe_2 in (b) is more similar to this case. (d) Polarization dependent photocurrent observed in graphene, which is a C_{6v} symmetry sample with a weak SOC. The HDP is due to the CPDE, figure is acquired from [19].

Besides, there are many experiments did on the same material with different wavelengths illumination, however, all of those researches claimed that the HDP observed in their experiments are due to CPGE. For example, many experiments were done in Bi_2Se_3 with different wavelengths of 632.8 nm and 650 nm [20], 795 nm [13], 1064 nm [21], 1550 nm [22] and 0.3∼40 THz [23]. Despite those experiments were done in different setups with different wavelengths, all of them claim that the HDP observed in their experiments are due to CPGE and related with the TSSs of Bi_2Se_3. It needs a second thought that whether it is true that CPGE has a such broad band response, and whether the HDP related with the TSSs or not, since the bulk band gap of Bi_2Se_3 is just 0.3 eV.

1.2 Research purpose

Motivated by these pioneering works, this thesis will explore more possibility on the helicity dependent photocurrent (HDP) in materials with SOC. Based on the current information in this field, we would like to investigate some questions which are unsettled.

1. *Does HDP commonly exist in strong SOC materials?*

2. *A lot of researches have been done in TIs with different wavelengths of laser. As a result, they all observed HDP and claimed the TSSs could be the origin. Is that correct that HDP can be observed in TIs almost at any wavelength and originated from TSSs?*

3. *The previous reports based on Rashba SOC materials and TIs reveals that incident angle dependence of HDP is originated from the in-plane spin nature of those surface states. Is it certain that the out-of-plane spin cannot be injected into those materials?*

With our *in situ* measurement system we are going to investigate HDP in a Si(111) substrate, a topological insulator Bi_2Se_3 thin film, a Rashba system Bi/Si(111) thin film and a series of Fermi level controlled topological insulator $(Bi_{0x}Sb_{1-x})_2Te_3$ thin film. Mainly focusing on the well-studied Bi_2Se_3 with comparison with other materials, we will try to answer these three questions in this thesis.

1.3 Structure of this thesis

Chapter 2 will introduce the theoretical background of this whole research and review the up-to-date experiments of HDP. Chapter 3 will introduce some key apparatuses and techniques used in our *in-situ* measurement system. Chapter 3 will give an introduction of the materials used in this research and review the current understanding of those materials. Chapter 4 will be divided into 5 sections. The first section is the mathematical calculation of the experimental results. The second section is the photocurrent measured on a Si(111) substrate as a control experiment. The third section will start from the growth of Bi_2Se_3 to the results of HDP measured in Bi_2Se_3. The main conclusion of this thesis will be based on the results from this section. The fourth section is the results and discussion based on Bi/Si(111). The fifth section will introduce the growth and the experimental results of $(Bi_xSb_{1-x})_2Te_3$. Finally, conclusions will be given in chapter 5. We will try to answer the questions we brought up at the beginning and will further bring up a few questions to be researched in the future.

Chapter 2

Theoretical background

2.1 Spin-orbit interaction and Rashba effect

In quantum physics, the Kramers degeneracy theorem [24] states that in every electronic system with time reversal symmetry (TRS) and space inversion symmetry (SIS), spin-up state and spin-down state possess the same energy. The derivation is straightforward. For time reversal symmetry,

$$|E_{k,\uparrow}\rangle = |E_{-k,\downarrow}\rangle \tag{2.1}$$

For space inversion symmetry,

$$|E_{k,\uparrow}\rangle = |E_{-k,\uparrow}\rangle \tag{2.2}$$

When the system possesses both TRS and SIS, we have

$$|E_{k,\uparrow}\rangle = |E_{k,\downarrow}\rangle \tag{2.3}$$

This theorem gives us the idea that if we break the symmetry of TRS, SIS, or both, Eqn.2.3 is not necessarily held so that we may produce spin non-degenerated states. A textbook example is Zeeman effect, by applying a magnetic field one breaks the TRS and lifts the spin degeneracy. Another case is by breaking the SIS, as observed from 2D electron gas (2DEG) in quantum well heterostructure, like $\mathrm{GaAsAl}_x\mathrm{Ga}_{1-x}\mathrm{As}$ [25], or on a metal surface, like Au [26]. With magnetic field, we makes the energy for spin-up and -down different. But why does the SIS breaking lift the spin degeneracy? We should seek the answer from spin-orbit coupling (SOC).

Spin-orbit interaction is a relativistic effect [27]. If an electron is moving in an electric field $\boldsymbol{E}$ with a speed $\boldsymbol{v}$, in the rest frame of the electron, it will experience a magnetic field $\boldsymbol{B}$,

$$\boldsymbol{B} = \gamma(\boldsymbol{v} \times \boldsymbol{E})/c^2 \tag{2.4}$$

where γ is the relativistic factor. In this magnetic field the electron acquires an energy due to the coupling between the electron's spin and the magnetic field

$$H_{SOC} = \frac{\mu_B}{2mc^2}\sigma \cdot (\boldsymbol{p} \times \boldsymbol{E}) \tag{2.5}$$

here, σ denotes the electron spin (represented by Pauli matrices). In atoms, where an electron moves in a closed orbital semiclassically, we need a correction of factor 1/2, known as Thomas correction [28].

Writing $p = \hbar k$, $E = -\nabla V$, we can write the SOC Hamiltonian as,

$$\hat{H} = \alpha \left(\nabla V \times \boldsymbol{k}\right) \cdot \sigma \tag{2.6}$$

Here, $\boldsymbol{k}$ is the Bloch wave vector. When we consider the SOC at the surface, i.e. the case of quasi-2DEG, electrons are free in the surface plane. *Because of the transition at the surface-vacuum interface*, the lattice potential $V_\perp$ has a gradient $\nabla V = \mathrm{d}V/\mathrm{d}z\hat{e}_z$, where the $\hat{e}_z$ is the unit vector of surface normal direction. Consequently, we will have the Hamiltonian written as

$$H_{SOC} = \alpha_R \left(\hat{e}_z \times \boldsymbol{k}\right) \cdot \sigma \tag{2.7}$$

so-called the Rashba term [29]. Now we can see that the breaking of SIS with SOC, one can also lift spin degeneracy. Also, from ref.[27], the authors got an explanation for the Rashba factor α_R using the tight binding model.

$$\alpha_R = 6\alpha\eta/w \tag{2.8}$$

The α_R is proportional to the surface potential gradient η, and atomic spin-orbit parameter α which is decided by the atomic number Z. So, we can almost say that the heavier the atom is, the larger splitting we get. However, by comparing the results between silver and gold, we will know this is not so simple.

In the paper by LaShell *et al* [26], it was noticed that the electric field could not be naively identified with the gradient of surface potential. When digging in deeper, people finally get that it is *the gradient of the surface-state wave function decaying into the bulk near the position of the nucleus* that determines the size of the Rashba splitting [30]. And in their simulation of band structures they find out that *only when both the potential gradient and wave function gradient are large, can we get a sizable splitting.* The gradient of the wave function is realized by the formation of hybrid states with orbitals, e.g. the surface states are l-character dominated (l is the orbital angular momentum), then the gradient means the hybridization of l- and $l \pm 1$-character. Thus, they reach to a conclusion that a surface state of purely p- or d-character shows no Rashba splitting at all, as in the silver case.

To get a taste of spin splitting band when Rashba effect occurs, we can solve Eqn.2.7. For simplicity, let us consider an infinite 2DEG. The Hamiltonian of such 2DEG can be written as kinetic energy + SOC energy,

$$H_0 = \frac{\hbar^2 k^2}{2m^*} + H_R \tag{2.9}$$

where H_R is the Rashba Hamiltonian,

$$\begin{aligned} H_R &= \alpha_R \left(\hat{e}_z \times \boldsymbol{k}\right) \cdot \sigma \\ &= \begin{vmatrix} 0 & 0 & \hat{e}_z \\ k_x & k_y & k_z \\ \sigma_x & \sigma_y & \sigma_z \end{vmatrix} = \alpha_R \left(k_x\sigma_y - k_y\sigma_x\right) \end{aligned} \tag{2.10}$$

then we have

$$H_0 = \frac{\hbar^2(k_x^2 + k_y^2)}{2m^*} + \alpha_R \left(k_x\sigma_y - k_y\sigma_x\right) \tag{2.11}$$

Using Pauli matrices and rewrite this Hamiltonian in matrix form,

$$\sigma_x = \begin{pmatrix} 0 & 1 \\ 1 & 0 \end{pmatrix}, \quad \sigma_y = \begin{pmatrix} 0 & -i \\ i & 0 \end{pmatrix}, \quad \sigma_z = \begin{pmatrix} 1 & 0 \\ 0 & -1 \end{pmatrix} \tag{2.12}$$

$$H = \begin{pmatrix} \frac{\hbar^2}{2m^*}\left(k_x^2 + k_y^2\right) & -\alpha(ik_x + k_y) \\ \alpha(ik_x - k_y) & \frac{\hbar^2}{2m^*}\left(k_x^2 + k_y^2\right) \end{pmatrix} \tag{2.13}$$

then we can find out the eigenvalues of the 2DEG

$$E_\pm = \frac{\hbar^2 k^2}{2m^*} \pm \alpha k, \quad k = |k| \tag{2.14}$$

Generally, time-independent Schrödinger equations takes form of $\hat{H}|\psi\rangle = E|\psi\rangle$. The eigenstates of this 2×2 matrix in Eqn.2.13 are of 2×1 vector form. Usually we can use a spinor to represent an arbitrary orientated spin, by superposition of spin-up $|\uparrow\rangle = \begin{pmatrix} 1 \\ 0 \end{pmatrix}$ and spin-down $|\downarrow\rangle = \begin{pmatrix} 0 \\ 1 \end{pmatrix}$.

$$|\chi\rangle = a_1 \begin{pmatrix} 1 \\ 0 \end{pmatrix} + a_2 \begin{pmatrix} 0 \\ 1 \end{pmatrix} = \begin{pmatrix} a_1 \\ a_2 \end{pmatrix} \tag{2.15}$$

The normalization requires $a_1^2 + a_2^2 = 1$. And the wave function of the spinor is

$$|\psi\rangle = e^{i\boldsymbol{k}\cdot\boldsymbol{r}} \begin{pmatrix} a_1 \\ a_2 \end{pmatrix} \tag{2.16}$$

To find out the eigenstates for these eigenvalues in Eqn.2.14, plugging the eigenvalues back into matrix-form Schrödinger equation.
For E_+ we have

$$\frac{a_2}{a_1} = \frac{ik_x + k_y}{\sqrt{k_x^2 + k_y^2}} = i(\cos\theta_k + i\sin\theta_k) = ie^{i\theta_k} \tag{2.17}$$

similarly, for E_- we have,

$$\frac{a_2}{a_1} = \frac{-ik_x + k_y}{\sqrt{k_x^2 + k_y^2}} = -ie^{i\theta_k} \tag{2.18}$$

where $\theta_k = \arctan(k_y/k_x)$. Then we have the eigenstates like,

$$|\psi_+\rangle = \tfrac{1}{\sqrt{2}} \begin{pmatrix} 1 \\ ie^{i\theta_k} \end{pmatrix} e^{i\boldsymbol{k}\cdot\boldsymbol{r}} = e^{i\boldsymbol{k}\cdot\boldsymbol{r}} \tfrac{1}{\sqrt{2}} (|\uparrow\rangle + ie^{i\theta_k} |\downarrow\rangle) \,, \tag{2.19}$$

$$|\psi_-\rangle = \tfrac{1}{\sqrt{2}} \begin{pmatrix} 1 \\ -ie^{i\theta_k} \end{pmatrix} e^{i\boldsymbol{k}\cdot\boldsymbol{r}} = e^{i\boldsymbol{k}\cdot\boldsymbol{r}} \tfrac{1}{\sqrt{2}} (|\uparrow\rangle - ie^{i\theta_k} |\downarrow\rangle) \tag{2.20}$$

Take an example, for electrons of $|\psi_+\rangle$ state with $+\hbar\boldsymbol{k_x}$ momentum, $\theta_k = 0$, $|\psi_+\rangle$ infers the spinor state $|\uparrow\rangle + ie^{i\theta_k} |\downarrow\rangle = \begin{pmatrix} 1 \\ i \end{pmatrix}$ which is the spin $|y, +\rangle$ (spin up in y-direction, one of the eigenstates of σ_y), and for $-\hbar\boldsymbol{k_x}$ state, $\theta_k = 180°$, spinor is $\begin{pmatrix} 1 \\ -i \end{pmatrix}$ which is spin $|y, -\rangle$. We can see that the spin degeneracy is

lifted, and the spin direction is perpendicular to the momentum, so-called *spin-momentum locking*. Plotting these eigenvalues we would see the spin-splitting bands, which are similar as observed at Au(111) by ARPES, as shown in Fig.2.1.

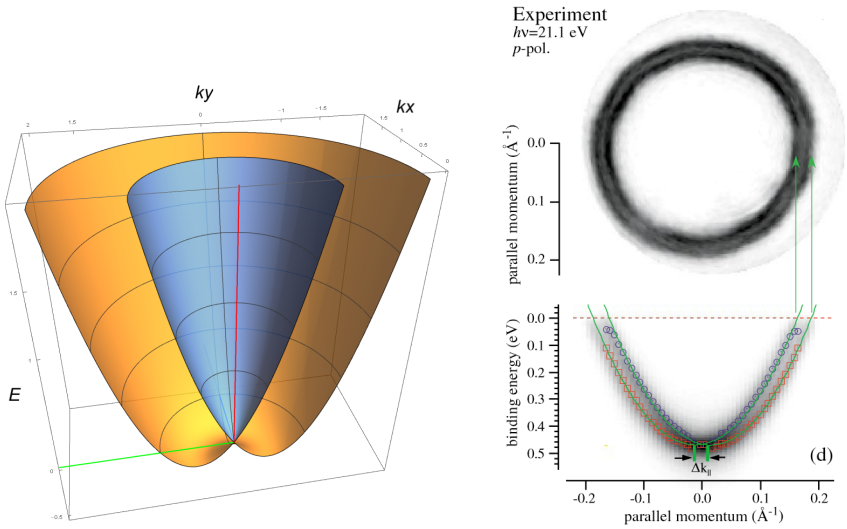

(a) (b)

Figure 2.1: (a) A schematic spin-splitting band structure induced by Rashba effect. Two colors denote different eigenstates of electron, blue for $|\psi_+\rangle$, yellow for $|\psi_-\rangle$. (b) Au(111) ARPES data acquired from ref.[31]

In addition, we can calculate the Berry's phase from the wave functions of the Rashba state in Eqn.2.20. Berry's phase is a geometrical phase when a quantum mechanical system undergoes an adiabatic evolution on a closed path in the parameter space [32, 33, 34]. Although Berry's phase is encoded in the delicate electron wave functions, the influence of this phase is profound. For example, Berry's phase in anomalous Hall metals determines the anomalous Hall conductivity [35, 36], and nontrivial Berry's phase suppresses the backscattering in topological materials [37] or simply leads to the weak anti-localization [38].

First, we need to take the time derivative of the wave function

$$\frac{\partial}{\partial t}|\psi_\pm\rangle = \frac{1}{\sqrt{2}}\begin{pmatrix}1\\ \pm\frac{\partial\theta_k}{\partial t}ie^{i\theta_k}\end{pmatrix}e^{i\mathbf{k}\cdot\mathbf{r}} + i\frac{\partial\mathbf{k}}{\partial t}\cdot\mathbf{r}|\psi_\pm\rangle + i\mathbf{k}\cdot\frac{\partial\mathbf{r}}{\partial t}|\psi_\pm\rangle \tag{2.21}$$

After integrating over a whole periodicity T, the second and the third terms of this equation should be zero because the sate go back to the initial point in the parameter space [39]. Therefore, Berry's phase depends on the θ_k terms only.

$$\gamma_\pm(t) = \frac{1}{2}\int_0^T \frac{\partial\theta_k}{\partial t}e^{i\theta_k}dt = \pi. \tag{2.22}$$

Surprisingly, a nontrivial Berry's phase is acquired from a Rashba sub-band structure. It has been predicted that when both Rashba and Dresselhaus spin-orbit interactions are presented, each sub-band obtain a Berry's phase $\Phi_B =$

$\frac{\alpha^2-\beta^2}{|\alpha^2-\beta^2|}\pi$, α represents for Rashba factor and β for Dresselhaus [40, 41]. Such nontrivial Berry's phase has already been observed experimentally on Rashba systems like bismuth [42] and BiTeI [43].

All these properties introduced above can be simply arisen by breaking of SIS. Typically three kinds of SIS breaking can occur, i.e. bulk inversion asymmetry (BIA), structure inversion asymmetry (SIA) and interface inversion asymmetry (IIA) in structure [44]. BIA occurs in the materials where inequivalent atoms sit in the lattice points, like in GaAs of zinc blende structure. SIA usually refers to the surface-vacuum situations. And IIA represent the heterostructure. In general, SIA would lead to Rashba effect, yet BIA and IIA lead to Dresselhaus effect which is out of the theme of this thesis. Microscopically, SIA originates from the inversion asymmetry of the confining potential and yields the Rashba term in the Hamiltonian. In particular, the SIA (also BIA) coupling of the electron wave vector and spin causes a Larmor precession in an internal k-dependent effective magnetic field for electrons moving through a semiconductor structure [45].

2.2 Dirac equation and topological insulator

In 1928, an equation for relativistic quantum mechanical wave function is written down by P. A. M. Dirac [46, 47].

$$H = cp \cdot \alpha + mc^2\beta \tag{2.23}$$

where m is the rest mass of the particle, c is the speed of light and α_i and β are the Dirac matrices that satisfying

$$\alpha_i^2 = \beta^2 = 1 \tag{2.24}$$
$$\alpha_i\alpha_j = -\alpha_i\alpha_j \tag{2.25}$$
$$\alpha_i\beta = -\beta\alpha_i \tag{2.26}$$

In 2D case, the Dirac matrices take the same form of the Pauli matrices, where $\alpha_x = \sigma_x$, $\alpha_y = \sigma_y$ and $\beta = \sigma_z$. In 3D case, α and β are written as follows,

$$\alpha_i = \begin{pmatrix} 0 & \sigma_i \\ \sigma_i & 0 \end{pmatrix}, \ (i = x, y, z) \tag{2.27}$$

and

$$\beta = \begin{pmatrix} \sigma_0 & 0 \\ 0 & -\sigma_0 \end{pmatrix}. \tag{2.28}$$

The solution to this equation is the well-known relativistic energy-momentum relation

$$E^2 = m^2c^4 + p^2c^2. \tag{2.29}$$

This equation has two solutions for positive energy E_+ and two for negative energy

$$E_\pm = \pm\sqrt{m^2c^4 + p^2c^2}. \tag{2.30}$$

This equation implies the existence of antimatters, i.e. particle with negative energy or mass, which was experimentally confirmed several years after this equation. It is one of the main achievements of modern theoretical physics.

The relationship between the Dirac equation and the topological insulator can be seen from a solution of the bound state at the interface between a positive mass region and a negative mass region. Consider a 1D example for simplicity

$$m(x) = \begin{cases} -m_1, & x \leqslant 0 \\ +m_2, & x > 0 \end{cases} \quad m_1, m_2 > 0 \tag{2.31}$$

The Dirac Hamiltonian read:

$$H_{1D} = \hbar v k_x \begin{pmatrix} 0 & 1 \\ 1 & 0 \end{pmatrix} + m(x) v^2 \begin{pmatrix} 1 & 0 \\ 0 & -1 \end{pmatrix}. \tag{2.32}$$

The eigenvectors of the equation $H\Psi(x) = E\Psi(x)$ is

$$\Psi^+(x) = \begin{pmatrix} \frac{\hbar v \kappa_+}{E - m_2 v^2} \\ 1 \end{pmatrix} e^{i\kappa_+ x} \text{ and } \Psi^-(x) = \begin{pmatrix} \frac{\hbar v \kappa_-}{E + m_1 v^2} \\ 1 \end{pmatrix} e^{i\kappa_- x}, \tag{2.33}$$

where

$$\kappa_+ = \frac{\sqrt{E^2 - m_2^2 v^4}}{\hbar v} \text{ and } \kappa_- = \frac{\sqrt{E^2 - m_1^2 v^4}}{\hbar v}. \tag{2.34}$$

At $x = 0$, two wave functions should be equal, solve that and we have $E = 0$. The solution for zero energy, therefore, is

$$\Psi(x) = \frac{1}{\sqrt{2}} \sqrt{\frac{2v m_1 m_2}{\hbar(m_1 + m_2)}} \begin{pmatrix} -i \\ 1 \end{pmatrix} e^{\frac{-|m(x)x|v}{\hbar}}. \tag{2.35}$$

The solution of this bound state can be plot as Fig.2.2. The state is peaked at the interface.

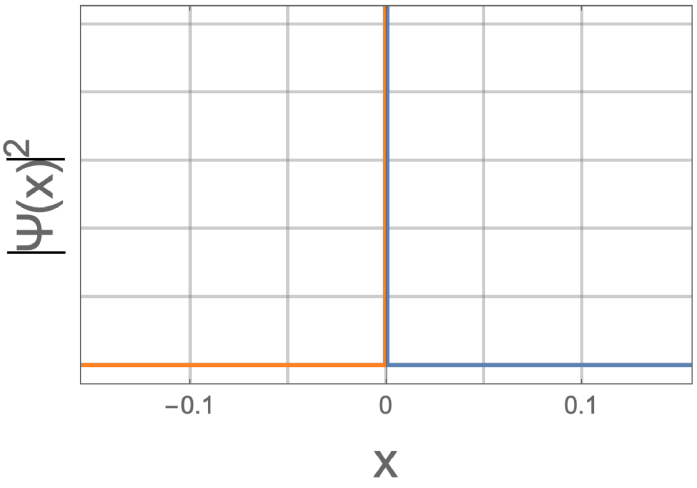

Figure 2.2: Interface state acquired from the Eqn.2.35. Orange and blue plots indicate states at $x > 0$ or $x \leqslant 0$. It decays too fast that looks like a Delta function.

This solution exists even when $m_2 \to \infty$. In this case, $\Psi(x) \to 0$ for $x > 0$. If the vacuum is treated as a system with an infinite positive mass, a system of a negative mass with an open boundary condition forms a bound state near the boundary [48]. That is, the edge states and surface states exist at the interface of systems with positive and negative masses. This is the source of some popular pictures for topological insulator. However, the symmetry between the positive and negative energy (mass) particles in the Dirac equation reflects that there is no topological distinction between particles with positive and negative masses [49].

To explore the topological insulator, a quadratic correction $-Bp^2$ is introduced to lift the energy (mass) symmetry in the Dirac equation so that it is topological distinguishable [48].

$$H = v\boldsymbol{p} \cdot \alpha + (mv^2 - B\boldsymbol{p}^2)\beta. \tag{2.36}$$

Here, B is a coefficient with the dimension of $1/m$. In 3D, we consider an x-y plane at $z = 0$. Using 1D solutions of the bound states we can derive an effective model for the surface states. Consider p_x- and p_y-dependent part as perturbation to 1D $H_{1D}(x)$,

$$\Delta H_{3D} = vp_x\alpha_x + vp_y\alpha_y - B(p_x^2 + p_y^2)\beta. \tag{2.37}$$

The effective Hamiltonian for the surface states can be derived based on the 1D results [48]

$$H_{eff} = vsgn(B)(p_x\sigma_x + p_y\sigma_y). \tag{2.38}$$

This Hamiltonian shows a similar structure as the one derived from the low-energy effective model by H. Zhang *et al.*[50].

$$H_{surf}(k_x, k_y) = \begin{pmatrix} 0 & A_2k_- \\ A_2k_+ & 0 \end{pmatrix} \tag{2.39}$$

with $k_\pm = k_x \pm ik_y$.

The eigenvalues of this Hamiltonian plotting in the E-k_xk_y space is exactly the Dirac cone as shown in Fig.2.3. The eigenstates of this Hamiltonian can be calculated similar to Eqn.2.15∼Eqn.2.20. They take the form of

$$|\psi_\pm\rangle = \frac{1}{\sqrt{2}} \begin{pmatrix} 1 \\ \pm ie^{i\theta_k} \end{pmatrix} e^{i\boldsymbol{k}\cdot\boldsymbol{r}} \tag{2.40}$$

As a result, we can see that the topological surface states (TSSs) is also in a fashion of spin-momentum locking. In addition, Berry's phase of the TSSs is the same as in Eqn.2.22, which is π. This nontrivial Berry's phase also ensures those properties discussed previously occurs on a topological insulator.

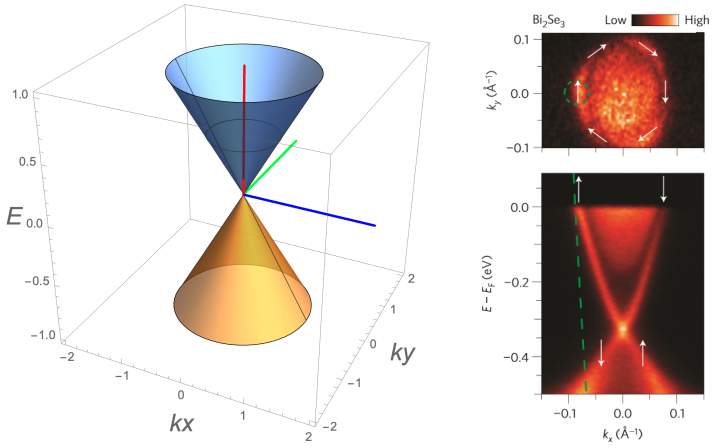

(a) (b)

Figure 2.3: (a) Surface states of a 3D $\mathbb{Z}_2$ topological insulator, blue and yellow colors denote $|\psi_+\rangle$ and $|\psi_-\rangle$. (b) Topological surface states of Bi_2Se_3 shown by ARPES. Arrows indicate different spin polarization, extracted from ref. [51]

Spin-momentum locking of the TSSs and the nontrivial π Berry's phase are the hallmarks for topological insulators (TIs). Experimentally, the guiding principle to find a TI is to search for insulators where conduction bands and valence bands have the opposite parity, and a 'band inversion' occurs when the strength of spin-orbit coupling is tuned [50]. As shown in the Fig.2.4, the first generation topological insulator $Bi_{1-x}Sb_x$ was achieved by changing the composition ratio of bismuth and antimony [52]. Both bismuth and antimony have an electron pocket at three equivalent L points. The valence and conduction bands at L point, derived from antisymmetric (L_a) and symmetric orbitals (L_s), have a small energy gap δ. At antimony concentration of $x \approx 0.04$, the band gap δ between L_a and L_s closes and a truly massless 3D Dirac point is realized.

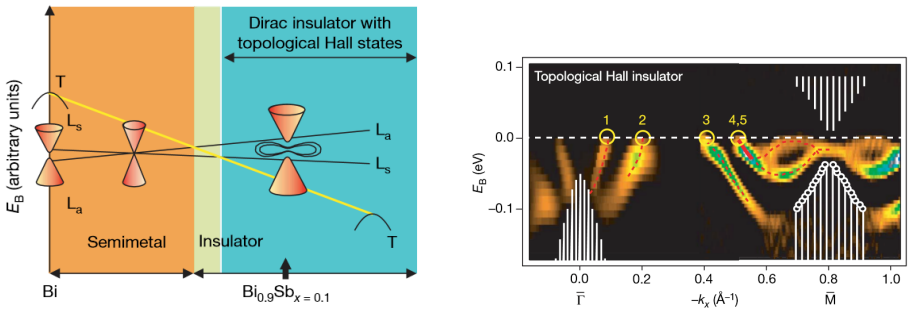

(a) (b)

Figure 2.4: $Bi_{1-x}Sb_x$ band evolution and ARPES data extracted from ref. [52]. (a) Band evolution of $Bi_{1-x}Sb_x$, from a semimetal to a topological insulator. (b) ARPES data of $Bi_{0.9}Sb_{0.1}(111)$. Surface band cross the Fermi level five times between $\bar{\Gamma}$ and $\bar{M}$ point.

2.3 Hexagonal warping

Soon after the semiconducting alloy Bi_xSb_{1-x} was confirmed to be a topological insulator, a family of materials Bi_2X_3 (x =Se or Te) was found to be topological insulators with a single helical Dirac cone surface state. As already shown in Fig.2.3(a), the era of the second generation topological insulator started with the ARPES verification of the undoubled Dirac fermion in Bi_2Se_3 by D. HsieH et al. [53]. Everything is as beautiful as the previous computational results suggested until the ARPES measurement shows that, for Bi_2Te_3 [54], a slightly different "cone" exists.

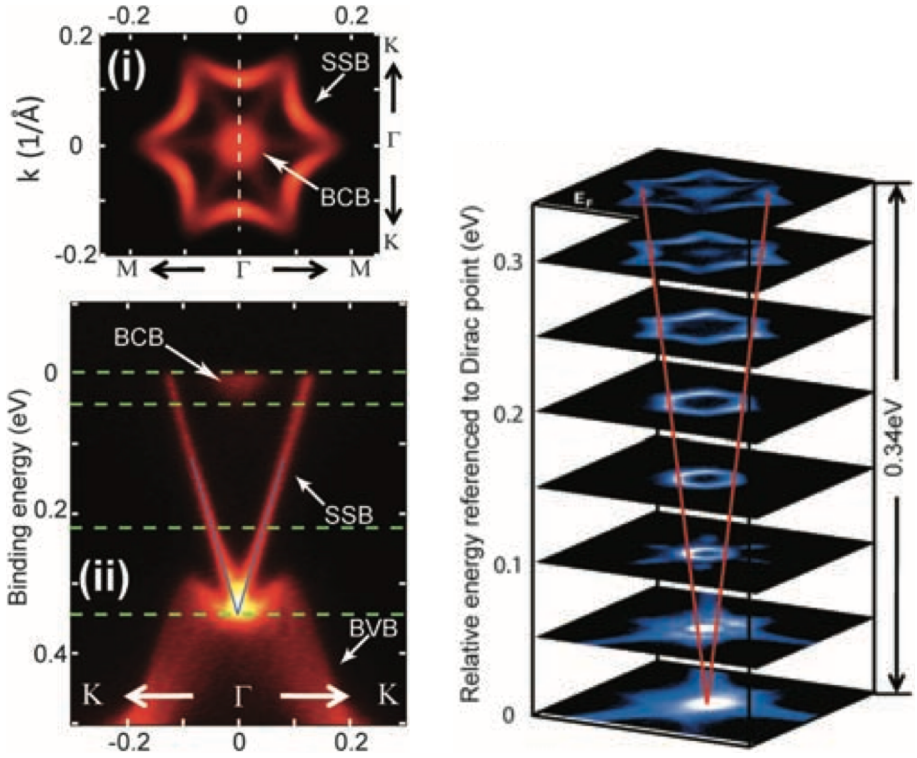

Figure 2.5: Bi_2Te_3 band evolution and ARPES data. Figures are from ref. [54]. (a) Band dispersion and the Fermi surface of Bi_2Te_3. (b) Constant-energy contours shows the hexagonal warping band structure.

At that time, the hexagram shape of the surface state is explained by the band repulsion of the snowflake-shape bulk electron pocket. To find a theoretical explanation, Liang Fu used $k \cdot p$ theory and found an unconventional hexagonal warping term which is the results of the symmetry requirements [55]. In his Letter, he found that in order to satisfy C_{3v} symmetry, additional term $H_w = \frac{\lambda}{2}(k_+^3 + k_-^3)\sigma_z$ must be included in the Hamiltonian. Although the Hamiltonian is threefold invariant, the band structure is actually six-fold symmetric because of the presence of time-reversal symmetry.

The Hamiltonian used by Fu is

$$H(k) = E_0(k) = v_k(k_x\sigma_y - k_y\sigma_x) + \frac{\lambda}{2}(k_+^3 + k_-^3)\sigma_z. \tag{2.41}$$

It is worth mentioning that the pseudo-spin σ_i is proportional to the electron's spin: $\langle s_z\rangle \propto \langle\sigma_z\rangle$ and $\langle s_{x,y}\rangle \propto \langle\sigma_{x,y}\rangle$. The eigenvalue of this Hamiltonian is

$$E_\pm(k) = E_0(k) \pm \sqrt{v_k^2k^2 + \lambda^2k^6\cos^2(3\theta)}. \tag{2.42}$$

As a result, we have the warped Dirac cone.

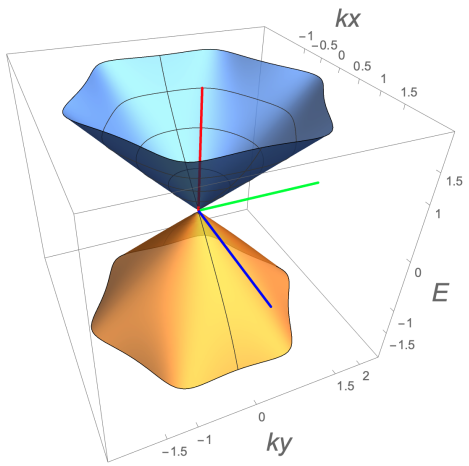

Figure 2.6: Eqn.2.42 plots in $E - k_xk_y$ space. Hexagonal warped Dirac cone is similar to the experimental observed as shown in Fig.2.5(b).

In fact, this hexagonal warping term can be applied into other SOC systems which possess C_{3v} symmetry, like Rashba surface states. This is due to the fact that both topological surface states and Rashba surface states are the products of the SOI. Therefore the Hamiltonians of TSSs and Rashba SSs are basically the same, except that the effective Hamiltonian of TIs reflects the topological nontrivial band structures of the bulk but that of Rashba materials corresponds to trivial bulk topologies [56].

$$H_{HW} = b(k_x\sigma_y - k_y\sigma_x) + \frac{k^2}{2m_s} + \frac{c}{2}(k_+^3 + k_-^3)\sigma_z \tag{2.43}$$

Here, $b = \alpha_R$ if the system is a Rashba material and $b = \hbar v_F$ if the system is a TI. m_s is the effective mass and c is the factor related with the hexagonal warping. For a more accurate expression, a unit vector $\boldsymbol{n}$ which denotes the surface normal direction should be added into the first term of this equation $b(k_x\sigma_y - k_y\sigma_x)\cdot\boldsymbol{n}$. It is clear, during our deduction of Rashba surface states in the first section of this chapter, that the lattice potential gradient ∇V, i.e. surface normal direction $\boldsymbol{n}$ here, determines the spin-momentum locking direction. We did not mention this in the deduction of TSSs at previous section because the TSSs are introduced by interfacing positive and negative masses, here we pointed it out.

This means that the spin-momentum locking of TSSs, similar as Rashba states, is opposite between top and bottom surfaces. In the rest of the deduction we mainly take the top surface states which $\boldsymbol{n} = +1$.

With this equation, we can plot the Rashba surface states under the hexagonal warping effect.

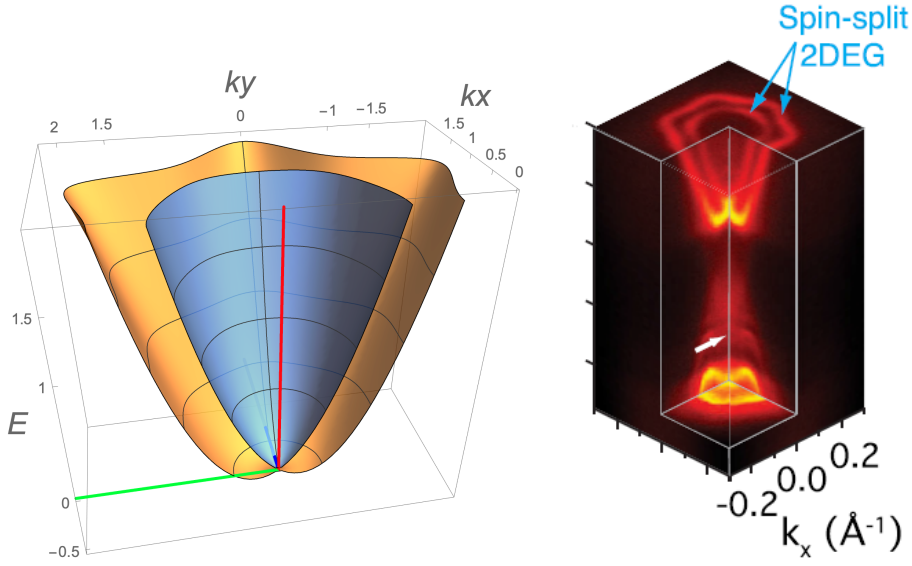

(a) (b)

Figure 2.7: (a). Energy dispersion from Eqn. 2.43. (b). Spin-splitting 2DEG above the topological surface states of Bi_2Se_3. Arrow indicates the Dirac point position. Figure (b) is from [57].

Hexagonal warping has some serious impacts on the properties of a material. In Fu's letter [55], three examples were listed. First, as shown in Eqn. 2.43, Hamiltonian couples to σ_z, the spin polarization of surface states would have an out-of-plane component $s_z \propto \langle \sigma_z \rangle$. Individual spin components can be solved

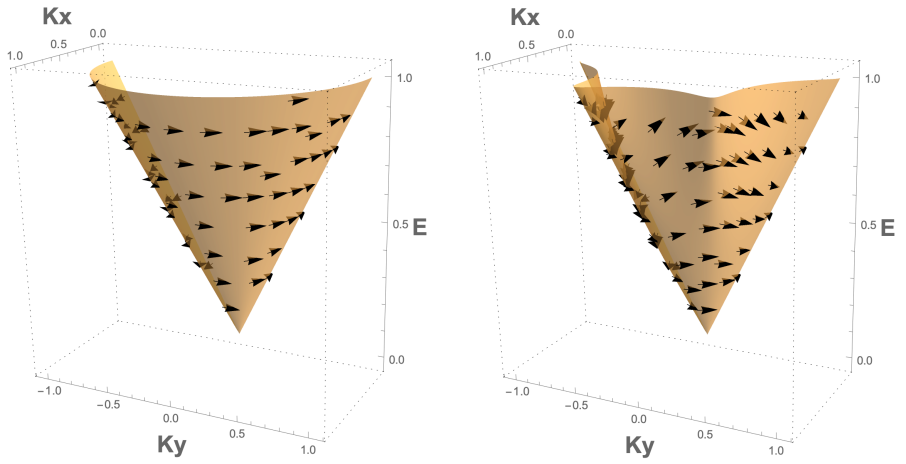

(a) (b)

Figure 2.8: Spin textures for a upper half Dirac cone (a) without and with (b) hexagonal warping. Black arrows denote the spin direction of that position. Spin is perfectly in-plane when there is no hexagonal warping effect. When hexagonal effect is taken into account, out-of-plane spin emerges. In addition, out-of-plane spin is much apparent at higher energy position (far from the Dirac point) than lower energy position (close to the Dirac point). Besides, no out-of-plane component exists at the vertexes of the hexagram (ΓM direction) but takes maximum at the concave center (ΓK direction). In addition, the out-of-plane components at two adjacent concave areas are opposite.

from the eigenstates of the Hamiltonian in Eqn. 2.41:

$$\begin{aligned} S_x &= \frac{\hbar}{2}\langle u(\boldsymbol{k},\pm)|\sigma_x|u(\boldsymbol{k},\pm)\rangle \\ &= \pm\frac{\hbar}{2}\frac{-\hbar v_k k_y}{\sqrt{\lambda^2(k_x^3-3k_xk_y^2)^2+\hbar^2v_k^2k^2}} \end{aligned} \tag{2.44}$$

$$\begin{aligned} S_y &= \frac{\hbar}{2}\langle u(\boldsymbol{k},\pm)|\sigma_x|u(\boldsymbol{k},\pm)\rangle \\ &= \pm\frac{\hbar}{2}\frac{\hbar v_k k_x}{\sqrt{\lambda^2(k_x^3-3k_xk_y^2)^2+\hbar^2v_k^2k^2}} \end{aligned} \tag{2.45}$$

$$\begin{aligned} S_z &= \frac{\hbar}{2}\langle u(\boldsymbol{k},\pm)|\sigma_x|u(\boldsymbol{k},\pm)\rangle \\ &= \pm\frac{\hbar}{2}\frac{\lambda(k_x^3-3k_xk_y^2)}{\sqrt{\lambda^2(k_x^3-3k_xk_y^2)^2+\hbar^2v_k^2k^2}} \end{aligned} \tag{2.46}$$

Here, results for an upper half Dirac cone ($u(\boldsymbol{k},+)$) are shown in Fig. 2.8.

The out-of-plane spin polarization is also momentum-dependent and can reach up to 25% of the in-plane component along ΓK direction in Fig. 2.5(a) according to the ARPES measurement [58].

Second, hexagonal warping gives rise to a novel mechanism for gap opening

at the Dirac point. Since out-of-plane component s_z exist, even applying an in-plane magnetic field could generate a mass term in the Hamiltonian, which opens up an energy gap.

Third, hexagonal warping in topological surface states would lead to two types of Friedel oscillation patterns, since multiple pairs of stationary points exist on the non-convex constant energy contour and inter-pair scattering is allowed [59]. However, *this does not mean that back scattering is allowed when hexagonal warping term exist.* The opposite spin is still coupled with opposite momentum.

Besides these effects firstly predict by Fu, more phenomena are noticed as time goes by. For example, Wu *et al* found that scattering events across a TI junction will shows a strong angle dependence [60]; Li *et al* found that the hexagonal warping term extends the topological region of the vortex line and leads to Majorana zero modes, this could happen even in the energy regions out of topological surface states [61].

2.4 Spin and charge interplay

When speaking of the spin charge interplay, one would immediately think of the famous spin Hall effect (SHE) and the inverse spin Hall effect (ISHE). The SHE was theoretically predicted by Dyakonov and Perel early in 1971 [62], but experimentally realized 30 years later in 2004 by Kato [63]. Since ISHE and SHE allow spin and charge interconversion without ferromagnet or external magnetic field, they attract attentions in spintronic applications. The mechanism of SHE or ISHE can be divided into two parts: intrinsic and extrinsic.

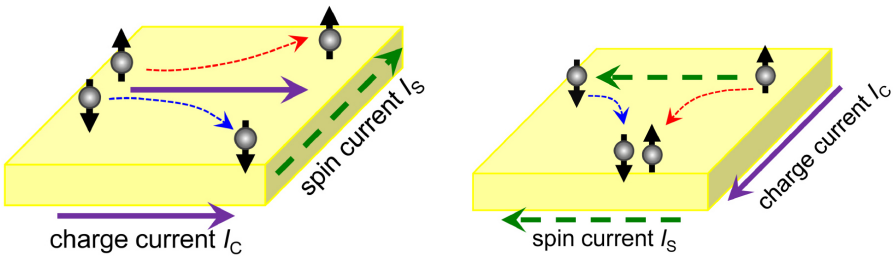

Figure 2.9: (a) SHE and (b) ISHE. Figures are from [64].

The intrinsic mechanism is based on the band structure, which was proposed by Karplus and Luttinger in 1954 [65] to explain anomalous Hall effect (AHE). This theory is reformulated by Berry's phase explanation [66] and works well for explaining the SHE in 3d transition metals, which is the trajectory dependent phase factor acquired from the d-orbitals. So far the intrinsic mechanism has been reported to dominate over extrinsic mechanisms in 4d and 5d transition metals [67, 68]. For the intrinsic mechanism, the spin Hall resistivity ρ_{SHE} is proportional to ρ_{xx}^2.

The extrinsic mechanism is based on the impurity scattering, it is caused by SOI between the spin of conduction electrons and the impurities. Two kinds of mechanisms, i.e. skew scattering [69] and side jump [70] compose the extrinsic

mechanism. They are all spin dependent scattering events at the impurity site, but the skew scattering is inelastic, and the impurities are in the lattice, whereas side jump is elastic. In addition, the side jump spin Hall conductivity arising from the electron-phonon scattering is conventionally regarded to be temperature (T) independent, although the phonon density varies with T [71] thus recent research suggests otherwise [72]. Moreover, side jump effect is said to be proportional to the impurity concentrations [73], whereas the screw scattering is not. The spin Hall resistivity ρ_{SHE} of skew scattering is proportional to the resistivity ρ_{imp} induced by the impurities, but that of the side jump effect is proportional to ρ_{imp}^2 or $\rho_{imp}\rho_{total}$. The most important spin Hall angle θ_{SHE} is defined as

$$\theta_{SHE} = \frac{\rho_{SHE}}{\rho_{imp}} = a + b\rho_{imp}(\text{or}\rho_{total}) \tag{2.47}$$

Here a and b are the coefficients of the skew scattering and the side jump.

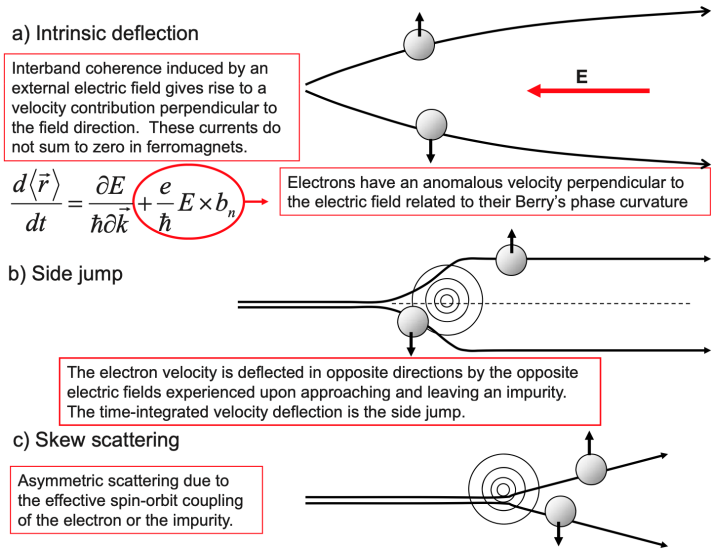

Figure 2.10: Three main mechanisms of AHE. Figures are from [74].

It can be seen that the SHE and AHE share the same mechanisms, indeed, SHE, ISHE and AHE are essentially the same thing if a system possess inversion symmetry [75]. However, they will become individual effects when the symmetry argument no longer holds. For example, in a 2DEG system the inversion symmetry is broken and the Rashba type SOI would suppresses the extrinsic contribution of SHE drastically [76, 77]. It is said that in the pure Rashba model the SHE and AHE would vanish but only a finite ISHE remains [75].

2DEG with symmetry breaking is indeed an interesting system. Though the spin-orbit coupling lifts the spin degeneration, there is no current or spontaneous spin polarization in equilibrium. However, there are approaches other than SHE and ISHE for spin and charge current interconversion. First, considering the simplest situation in which only one spin-momentum locking Fermi surface presents. By applying an electrical field along x-direction the Fermi surface shifts along $\boldsymbol{k_x}$ direction by δk (Fig. 2.11).

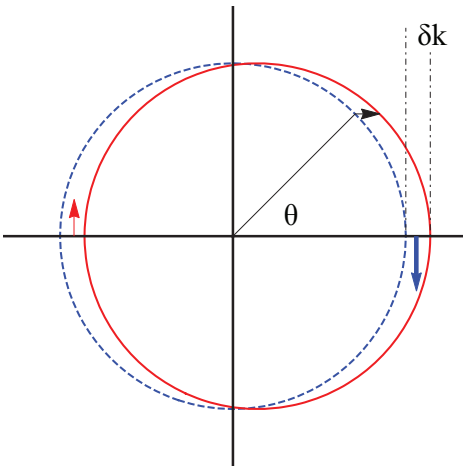

Figure 2.11: Fermi surface in non-equilibrium distribution, black arrow shows shifted direction. Dashed line—equilibrium; solid line—non-equilibrium. Thicker blue arrow means promoted spin, thinner red one means restrained spin.

We simply use Drude model to calculate the current and spin polarization in such non-equilibrium states.

$$J = nev \tag{2.48}$$

In general, the electron concentration is given in terms of the density of states (DOS) $N(E)$:

$$n = \int_0^\infty f(E)N(E)dE \tag{2.49}$$

Here we take an approximation by changing the Fermi-Dirac distribution function into a step function,

$$f(E) = \frac{1}{\exp[(E - E_\mathrm{F})/k_\mathrm{B}T] + 1} \approx \begin{cases} 1, & (E \leqslant E_\mathrm{F}) \\ 0, & (E > E_\mathrm{F}) \end{cases} \tag{2.50}$$

Then we can calculate the electron concentration simply by integrating the Fermi surface

$$n = \frac{2}{4\pi^2} \int_{|\mathbf{k}|<k_\mathrm{F}} d\mathbf{k}. \tag{2.51}$$

In the case of Fig. 2.11, what we need to do is to integrate the shifted area of the Fermi disc. Noted that in spin-splitting systems, only one state is allowed per unit k-space, however, the shift of Fermi disc happens on both sides which would preserve the factor 2 of DOS for a spin-splitting system.

$$n = \frac{2}{4\pi^2} \int_{-\frac{\pi}{2}}^{\frac{\pi}{2}} \delta k \, \cos\theta \, k \, d\theta \tag{2.52}$$

When the shift of Fermi surface is tiny, we can obtain

$$\begin{aligned} J_x &= \int_{-\frac{\pi}{2}}^{\frac{\pi}{2}} \frac{2}{4\pi^2} \, e \, \delta k \, \cos\theta \, k \, v_F \, \cos\theta \, d\theta \\ &= \frac{e \, v_\mathrm{F} \, \delta k \, k}{4\pi}. \end{aligned} \tag{2.53}$$

Here, k is the same value as k_F in equilibrium. Similarly, we can get the 'spin injection' due to this shift of the Fermi surface.

$$S = \pm\frac{\hbar}{2}\int_{-\frac{\pi}{2}}^{\frac{\pi}{2}} \frac{2}{4\pi^2}\,\delta k\,\cos\theta\, k\,\cos\theta\, d\theta$$
$$= \pm\frac{\hbar}{2}\,\frac{\delta k\, k}{4\pi} \tag{2.54}$$

After this, we can treat a little bit complex case, i.e. 2D Rashba spin-splitting surface. Eq.2.53 and Eq.2.54 only correspond to one subband.

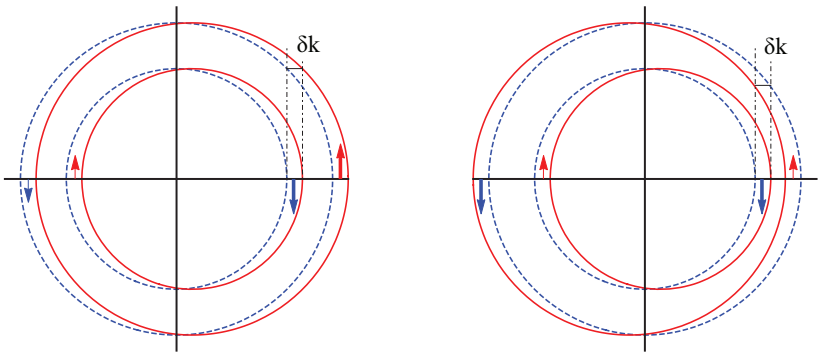

Figure 2.12: Two cases of non-equilibrium distributed Fermi surface of Rashba band. (a) is the case when applying an electric field; (b) is when spin injection happens.

Considering the two subbands, the total current would be:

$$J = j_1 \pm j_2 = \frac{ev_F\delta k}{4\pi}(k_1 \pm k_2) \tag{2.55}$$

subscripts 1 and 2 denote the inner and outer Fermi contour.

$$\text{For Fig. 2.12}(a)\ \ \frac{ev_F\delta k k_0}{2\pi}, \quad \text{for Fig. 2.12}(b)\ \ \frac{ev_F\delta k\,\eta\, k_0}{2\pi} \tag{2.56}$$

where k_0 is the average value of the two spin-splitting band wavevectors (Rashba splitting energy is $\pm\alpha_R k_0$), and η is a dimensionless factor to evaluate the splitting [78]. In the equilibrium 2DEG system with Fermi energy $\epsilon_F = (\hbar k_0)^2/2m^*$

$$\eta = \frac{\alpha_R m^*}{2\hbar^2 k_0} = \frac{\alpha_R k_F}{2\epsilon_F} \tag{2.57}$$
$$k_1 = (1-\eta)k_0, \quad k_2 = (1+\eta)k_0 \tag{2.58}$$

So if we use current to generate spin which is usually called as charge-to-spin conversion, i.e. case of figure 2.12(a), we would have a spin polarization of [79]

$$P = \frac{2(S_1+S_2)}{n} = \frac{2\eta}{v_F}\,\frac{J}{ne} = \frac{\alpha_R k_F}{v_F\epsilon_F}\,\frac{J}{ne}. \tag{2.59}$$

A direct conclusion we can get from Eqn.2.59 and Eqn.2.57 is: *a large charge-to-spin conversion ratio requires a large η, i.e. a large Rashba splitting α_R and a small Fermi energy ϵ_F*. As shown in Fig. 2.12, we can introduce two kinds of non-equilibrium to Rashba type states, by applying electrical field or through spin injection. Besides, we can instantly notice that comparing with single Fermi surface, i.e. TI case, the two Fermi surfaces of Rashba system always suppressing each other, no matter in spin inducing current circumstance or current stimulating spin polarization case. In the case of spin-to-charge conversion, with the same k_0, TI is 2η (maximum 2) times larger than Rashba type system.

For the case that spin polarization induced by a charge current, it is considered theoretically in more detailed by Edelstein [80] which is the Rashba-Edelstein effect (REE). The REE is verified experimentally at Bi/Ag interface [81] recently. Moreover, the reciprocal effect, inverse Rashba-Edelstein effect (IREE) which is a charge current induced by spin polarization, also exists. And the IREE is firstly experimentally realized also at Bi/Ag interface [82], and get better theoretical explained afterwards in 2013 [83]. Up to now, IREE has been observed on many materials, such as Rashba type metal alloy [84], topological insulators [85], oxide interfaces [86], etc.

It is worth mentioning that those equations above only apply to the spin-momentum locking surface without hexagonal warping. Things could get very complex when we include hexagonal warping effect. First, when hexagonal warping occurs, depending on the factor λ and energy level of the Fermi surface, the energy contour could strongly deviate from a perfect circle, therefore the simple calculation in Eqn. 2.52 would fail in such case. Second, as shown in Fig. 2.8(b), spin direction depends on the energy level of the Fermi surface and the direction of the Fermi surface (e.g. ΓK or else), so the spin injected due to the shift of the Fermi surface will strongly depends on the shift δk direction and the energy level.

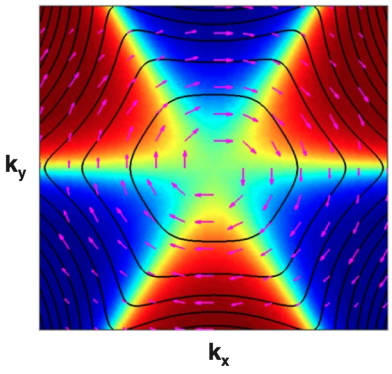

Figure 2.13: Conduction band spin textures of a hexagonal warped TSS. The arrow represents the in-plane spin polarization while the color indicates the out-of-plane component of the spin polarization, red for up and blue for down. The black line gives the constant energy contours. Figure is extracted from [87].

Take a very simple example to calculate the hexagonal warping effect, let's add an out-of-plane spin component to the Fermi surface of Fig. 2.11 which

takes a form of

$$S_z = ak\cos(3\theta + \varphi). \tag{2.60}$$

Here, factor ak together infers energy level of the Fermi surface, and φ denotes the Fermi surface shift direction, $\varphi = 0$ means ΓM direction.

It is clear that in-plane spin would follow the exact expression in Eqn. 2.54. For the out-of-plane spin:

$$\begin{aligned} S_z &= \pm\frac{\hbar}{2}\frac{2}{4\pi^2}\int_{-\frac{\pi}{2}}^{\frac{\pi}{2}} a\cdot\cos(3\theta+\varphi)\,\delta k\,\cos\theta\,k\,\cos\theta\,d\theta \\ &= \pm\frac{a\,\delta k\,k^2\,\hbar\cos(\varphi)}{15\pi^2}. \end{aligned} \tag{2.61}$$

The spin injected here is proportional to the shift, to the second order of k and greatly depend on the shift direction.

Furthermore, due to the symmetric distribution of the out-of-plane spin on the Fermi surface, as shown in Fig. 2.13, one cannot shift the Fermi surface by injecting out-of-plane spin thus no charge current generation in this scenario.

2.5 Light, photocurrent and spin

Light is an electromagnetic wave propagating in space, or a cluster of particles named photon traveling with the speed c. Depending on the observation methods, you can probe different aspects of a beam of light. Normally, we observe light as an electromagnetic wave. Similar as any kind of waves, it is able to carry energy and information. To describe a beam of light, for example, electric fields of a plane-wave propagating along z direction are

$$\tilde{\mathbf{E}}_x(z,t) = \hat{\mathbf{e}}_x E_{x0}(t)\exp[\mathrm{i}(-kz+\omega t+\varphi_x] \tag{2.62}$$

$$\tilde{\mathbf{E}}_y(z,t) = \hat{\mathbf{e}}_y E_{y0}(t)\exp[\mathrm{i}(-kz+\omega t+\varphi_y] \tag{2.63}$$

where $\tilde{\mathbf{E}} = \tilde{\mathbf{E}}_x(t) + \tilde{\mathbf{E}}_y(t)$. We can simply write the total field in a vector space where,

$$\tilde{\mathbf{E}} = \begin{pmatrix} E_{x0}\,e^{\mathrm{i}\varphi_x} \\ E_{y0}\,e^{\mathrm{i}\varphi_y} \end{pmatrix} = \begin{pmatrix} E_x \\ E_y \end{pmatrix} \tag{2.64}$$

Absorption, Reflection and Transmission

Basically, light interacts with media through transmission (transmittance T), reflection (reflectance R) and absorption (absorbance A). Especially, the absorption is of the interest of this thesis. A famous law that describes the absorption is called the Beer-Lambert Law.

$$A = \log_{10}\frac{I_0}{I_t} \tag{2.65}$$

where A is the absorbance, I_0 is the initial intensity and I_t is the transmitted intensity. We can write

$$I_t = I_0 e^{-\alpha z} \tag{2.66}$$

The penetration depth can be expressed as $\delta_p = 1/\alpha$ which defines the length through which the light intensity drops to $1/e$ of its surface value. α is the absorption coefficient, which related to extinction coefficient κ by[i]

$$\alpha = \frac{4\pi\kappa}{\lambda} \tag{2.67}$$

λ is the wavelength of the light. This law is widely used for bulk materials, like a chunk of a solid or a glass of solution. In the case of thin films, it can suggest some properties but not accurate. This is because of the interference of the light occurs within the film thickness.

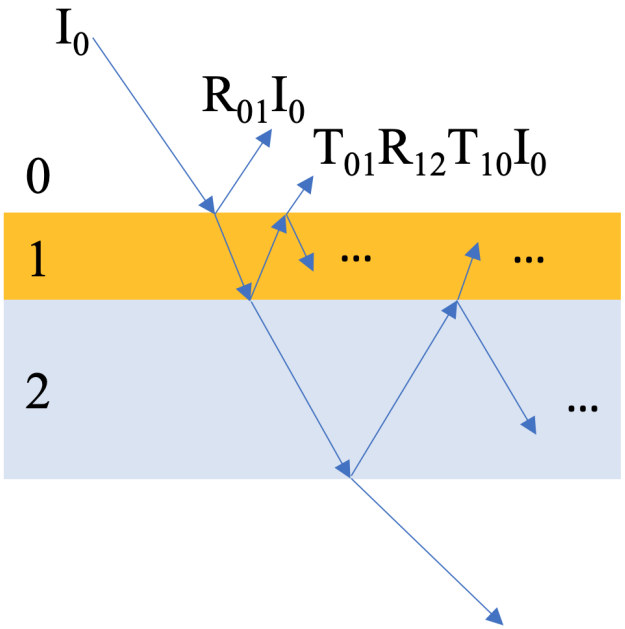

Figure 2.14: A beam of light I_0 incident from a medium 0 to a thin film 1 on a medium 2. Multiple reflections happen within film 1. As a result the total reflection is not simply equals to $R_{01}I_0$, it is $R_{01}I_0 + T_{01}R_{12}T_{10}I_0 + \cdots$. Similar case for the total transmission and total absorption.

To calculate the R, T and A we need to first calculate the reflection and transmission of the electrical fields, which are called reflection and transmission coefficients r, t. Using the Fresnel-Airy formulas [88]:

$$r = \frac{r_{12} + r_{23}e^{2i\beta}}{1 + r_{12}r_{23}e^{2i\beta}}, \tag{2.68}$$

$$t = \frac{t_{12}t_{23}e^{i\beta}}{1 + r_{12}r_{23}e^{2i\beta}} \tag{2.69}$$

where r_{ij} and t_{ij} are Fresnel coefficients for reflection and transmission coefficients from the i-th medium to the j-th medium, $\beta = n_2 k_0 \cos(\theta_2)h$, where θ_2 is the incident angle in the second medium, k_0 is the free-space wave vector, ω is

[i] https://en.wikipedia.org/wiki/Refractive_index

the angular frequency of the incident light and c is the speed of light in vacuum. As the Fresnel equation goes,

$$R = |r|^2, \tag{2.70}$$

$$T = \frac{n_f \cos\theta_f}{n_i \cos\theta_i}|t|^2. \tag{2.71}$$

θ_f and θ_i is the incident angle on the initial and finial material. In the case of normal incidence, according to Heavens, we will have [89, 90, 91]

$$\begin{aligned} R &= \frac{(g_1^2+h_1^2)\exp(2\alpha_1) + (g_2^2+h_2^2)\exp(-2\alpha_1) + A\cos 2\gamma_1 + B\sin 2\gamma_1}{\exp(2\alpha_1) + (g_1^2+h_1^2)(g_2^2+h_2^2)\exp(-2\alpha_1) + A\cos 2\gamma_1 + B\sin 2\gamma_1}, \\ T &= \frac{n_2}{n_0}\frac{((1+g_1)^2+h_1^2)((1+g_2)^2+h_2^2)}{\exp(2\alpha_1) + (g_1^2+h_1^2)(g_2^2+h_2^2)\exp(-2\alpha_1) + A\cos 2\gamma_1 + B\sin 2\gamma_1} \end{aligned} \tag{2.72}$$

where

$$\begin{gathered} A = 2(g_1g_2 + h_1h_2),\ B = 2(g_1h_2 - h_1g_2), \\ C = 2(g_1g_2 - h_1h_2),\ D = 2(g_1h_2 + h_1g_2), \\ g_1 = \frac{n_0^2 - n_1^2 - k_1^2}{(n_0+n_1)^2 + k_1^2},\ h1 = \frac{2n_0k_1}{(n_0+n_1)^2+k_1^2} \\ g_2 = \frac{n_1^2 - n_2^2 + k_1^2 - k_2^2}{(n_1+n_2)^2 + (k_1+k_2)^2},\ h_2 = \frac{2(n_1k_2 - n_2k_1)}{(n_1+n_2)^2+(k_1+k_2)^2} \\ \alpha_1 = 2\pi k_1 d/\lambda \quad \text{and} \quad \gamma_1 = 2\pi n_1 d/\lambda. \end{gathered} \tag{2.73}$$

Finally from the energy conservation we have the absorbance of the film:

$$A = 1 - R - T \tag{2.74}$$

The result of the thin film interference could be drastic, research shows that 70-80% of certain wavelength of the incident light is absorbed in a 10-15 nm thick Ge covered on Au [92].

The absorption of light mainly results in two kinds of consequences, photocurrent and thermal heating. Photocurrent is a generation of an electric current by light illumination. This phenomenon usually takes place in heterojunctions, like a p-n junction or a Schottky junction, where photoexcitation generates electron-hole pairs firstly, then under the field of the p-n junction or Schottky junction, electrons and holes are separated and swept into different directions. On the other hand, thermal heating is achieved by lattice or molecules resonating at the light frequency, which is usually at the infrared region. Inhomogeneous illumination will cause a thermal imbalance across the sample which could also lead to an electric current by the thermoelectric effect.

Spin orientation by circular polarization

Besides those conventional photocurrents or thermoelectric currents, a kind of electric current generated by the circularly polarized light, i.e. the helicity dependent photocurrent (HDP), catches the attention of researchers. As is known to all, circularly polarized light carries certain angular momentum, $\pm\hbar$ for left-handed circular polarization (LCP) or right-handed circular polarization

(RCP). Consequently, photoexcitation would be spin selective for a spin splitting band due to the unequal excitation possibility by LCP and RCP. Therefore, it is straightforward to think that the HDP is spin polarized, or at least to some percentages.

To illustrate the spin selective excitation, a simple model is presented which shows a circularly polarized light interacts with electrons at topological surface states. To write the Hamiltonian we need to substitute $\boldsymbol{p}$ by $\boldsymbol{p} - e\boldsymbol{A}$ in the Hamiltonian of Eqn. 2.41, and for simplicity let us do it without hexagonal warping effect.

$$H = v_k(k_x\sigma_y - k_y\sigma_x) - \frac{ev_k}{\hbar}(A_x\sigma_y - A_y\sigma_x) \tag{2.75}$$

The first term of this Hamiltonian is the topological states H_{TI} and the second term is the interaction Hamiltonian H_{int}. Considering a z-propagating plane wave that we used in in Eqn. 2.63 and rewriting it in the vector potential form $\boldsymbol{A} = A_0 e^{i(\boldsymbol{k}\cdot\boldsymbol{r}-\omega t+\varphi)}$. Here, q rather than k is used to distinguish the wave vector of light from that of the wave function.

$$\begin{aligned} A_x(z,t) &= A_{x0}\cos(qz - \omega t + \varphi_x), \\ A_y(z,t) &= A_{y0}\cos(qz - \omega t + \varphi_y) \end{aligned} \tag{2.76}$$

For RCP, $\varphi_x = \pi/2$, $\varphi_y = 0$, $A_{x0} = A_{y0}$ [93].

$$\begin{aligned} A_x(z,t) &= -A_0\sin(qz - \omega t), \\ A_y(z,t) &= A_0\cos(qz - \omega t) \end{aligned} \tag{2.77}$$

So the interaction Hamiltonian is

$$\begin{aligned} H_{int} &= -\frac{ev_k}{\hbar}(A_x\sigma_y - A_y\sigma_x) \\ &= -\frac{A_0 ev_k}{\hbar}(-\sin(qz-\omega t)\sigma_x - \cos(qz-\omega t)\sigma_y) \\ &= -\frac{A_0 ev_k}{\hbar}(-ie^{i\omega t - iqz}(\sigma_x + i\sigma_y) + ie^{-i\omega t - iqz}(\sigma_x - i\sigma_y)) \end{aligned} \tag{2.78}$$

Eqn.2.78 describes the emission (first term) and the absorption (second term) of a photon. We learn that the interaction with RCP is revealed as spin raising and lowering operators over the quantized spin along z axis, which is the light propagation direction. If the incident angle of the light is changed, the quantization axis varies accordingly. Spin selection rules requiring the RCP couples to spins that are aligned with the wave vector of the light [94]. If we change the RCP to LCP then the emission term would couple with the spin lowering operator and absorption term with the spin raising operator. Therefore, a material with helical spin structures can be excited asymmetrically by a circularly polarized light and produces a photocurrent if spin-momentum locking presents.

Photogalvanic effect

A practical example of this phenomenon is the circular photogalvanic effect (CPGE). Photogalvanic effect (PGE) has been observed in the early 1970s [95]. Besides the current due to uniformed illumination on the sample, additional contribution of current which strongly affected by the polarization of the light was

discovered, and this was interpreted as an optical rectification effect at that time [96]. Moreover these results show that the direct current depends linearly on the intensity of the light, and stable even in a long period experiment [97]. The characteristics of large-value photovoltages and the direction dependent ruled out Dember effects, entrainment of electrons by photons, micro-inhomogeneities of crystals and other known photovoltaic phenomena [98].An important point of such phenomenon is that it takes place in crystals which lacks of an inversion center. And we know that in such kind of crystals, Rashba effect is possible. This overlapping gives us a hint that it is possible to manipulate spin by optical polarization. To give a phenomenological interpretation, we derive this effect from the fundamental nonlinear optics.

The electric current in a homogeneous medium can be expanded in a power series with the electric field:

$$\begin{aligned} J_i = \alpha^0_{ij}\boldsymbol{E}_j + \beta^0_{ijk}\boldsymbol{E}_j\boldsymbol{E}_k + \sigma^0_{ijkl}\boldsymbol{E}_j\boldsymbol{E}_k\boldsymbol{E}_l \\ +\gamma^0_{ijkl}\boldsymbol{E}_j\tilde{\boldsymbol{E}}_k\tilde{\boldsymbol{E}}^*_l + \beta_{ijk}(\omega)\tilde{\boldsymbol{E}}_j\tilde{\boldsymbol{E}}^*_k + \cdots \end{aligned} \tag{2.79}$$

Here $\boldsymbol{E}$ is the statistic electric field, the first three terms describe the static conductivity taking the nonlinear corrections into account. Here, $\tilde{\boldsymbol{E}}^*(\omega) = \tilde{\boldsymbol{E}}(-\omega)$ and $\boldsymbol{E}$ is the intensity of the field at frequency ω. The fourth term describes photoconductivity and the last term is for photogalvanic effect [98]. These currents are also referred to as injection or shift currents which are second-order nonlinear optical effects [99]. It is obvious that the magnitude of the second-order effect is proportional to the radiation intensity $I = c|\boldsymbol{E}(\omega)|^2/2\pi$. To focus on the second-order effect, we take the last term out.

$$\boldsymbol{j}_i = \beta_{ijk}(\omega)\tilde{\boldsymbol{E}}_j(\omega)\tilde{\boldsymbol{E}}_k(-\omega) \tag{2.80}$$

This equation would not hold under a spatial inversion operation since current $\boldsymbol{j}_i$ would be the opposite, however $\tilde{\boldsymbol{E}}_j(\omega)\tilde{\boldsymbol{E}}_k(-\omega)$ is the same. Therefore, to let current in Eqn.2.80 exist, the medium should not possess inversion symmetry, i.e. PGE only exists in materials lack of inversion symmetry. Another way to let Eqn.2.80 hold is by modifying the equation with a light wave vector $\boldsymbol{q}$ which lead to the photon drag effect (PDE). We will deduce the PGE first and get back to PDE later.

The second-rank tensor in eqn.2.80 can be divided into a symmetric part and an antisymmetric part by the permutability of the pair indices j and k,

$$\begin{aligned} \beta_{ijk} &= \beta^+_{ikj} + \beta^-_{ijk}, \\ \beta^+_{ikj} &= \frac{1}{2}(\beta_{ijk} + \beta_{ikj}), \\ \beta^-_{ikj} &= \frac{1}{2}(\beta_{ijk} - \beta_{ikj}). \end{aligned} \tag{2.81}$$

So, Eqn. 2.80 is rewritten as

$$\boldsymbol{j}_i = \beta^+_{ijk}E_jE^*_k + \beta^-_{ijk}E_jE^*_k \tag{2.82}$$

From the definition of the symmetric and antisymmetric part of the β_{ijk} we know that we will have $\beta_{ijk}(E_jE^*_k + E_kE^*_j)$ in the symmetric part and $\beta_{ijk}(E_jE^*_k -$

$E_k E_j^*$) in the antisymmetric part. For the antisymmetric part, it can be further expressed as

$$(E \times E^*)_i = \epsilon_{ijk} E_k E_j^*, \tag{2.83}$$

where ϵ_{ijk} is the Levi-Civita symbol in three dimensions.

Besides, this kind of representation of the electric field is well-used in polarization representation called *Stokes Vectors* [100]. The Stokes vectors contain four elements which are defined as [101],

$$\mathcal{S}_0 = I_x + I_y = E_{x0}^2 + E_{y0}^2 = E_x E_x^* + E_y E_y^* \tag{2.84}$$

$$\mathcal{S}_1 = I_x - I_y = E_{x0}^2 - E_{y0}^2 = E_x E_x^* - E_y E_y^* \tag{2.85}$$

$$\begin{aligned} \mathcal{S}_2 &= I_{+45^\circ} - I_{-45^\circ} = E_{+45^\circ} E_{+45^\circ}^* - E_{-45^\circ} E_{-45^\circ}^* \\ &= \tfrac{1}{2}[(E_x + E_y)(E_x^* + E_y^*) - (E_x - E_y)(E_x^* - E_y^*)] \\ &= E_x E_y^* + E_x^* E_y \end{aligned} \tag{2.86}$$

$$\begin{aligned} \mathcal{S}_3 &= I_R - I_L = E_R E_R^* - E_L E_L^* \\ &= \tfrac{1}{2}[(E_x - \mathrm{i}E_y)(E_x^* + \mathrm{i}E_y^*) - (E_x + \mathrm{i}E_y)(E_x^* - \mathrm{i}E_y^*)] \\ &= \mathrm{i}(E_x E_y^* - E_x^* E_y) \end{aligned} \tag{2.87}$$

$\mathcal{S}_0$ means the total intensity of the light; $\mathcal{S}_1$ is the intensity difference between x direction and y direction; $\mathcal{S}_2$ denotes the difference between $\pm 45^\circ$ direction linear polarization; $\mathcal{S}_3$ shows the difference between RCP and LCP.

Obviously, the symmetric part is related with $\mathcal{S}_1$ and $\mathcal{S}_2$ which are the linear polarization, while the antisymmetric part is related with $\mathcal{S}_3$ which is the circular polarization. Finally, we can rewrite Eqn. 2.80 in the form of

$$\begin{aligned} j_\lambda = \chi_{\lambda\mu\nu}[E_\mu(\omega)E_\nu^*(\omega) + E_\mu^*(\omega)E_\nu(\omega)]/2 \\ + \mathbf{i}\gamma_{\lambda\kappa}(\mathbf{E} \times \mathbf{E}^*)_\kappa \end{aligned} \tag{2.88}$$

Here we have the third-rank tensor $\chi_{\lambda\mu\nu}$ represents the symmetric part of β_{ijk} and second-rank pseudo tensor $\gamma_{\lambda\kappa}$ which $\gamma_{\lambda\kappa} = \beta_{\lambda\mu\nu}\epsilon_{\kappa\mu\nu}$. Clearly, the first term is even in ω, but the second is odd in ω. This means when transform $\omega \to -\omega$, or equivalently, $\mathbf{E} \to \mathbf{E}^*$, i.e. reverses the helicity of the circularly polarized light, the sign of the second term changes, yet the first term remains unchanged. Thus, the first term stands for the effect caused by the linearly polarized light[ii](a.k.a linear photogalvanic effect, LPGE) or shift current (in ref.[99]), and the second term for the circular photogalvanic effect (CPGE) or injection current.

Note that for LPGE the last two indices of tensor $\chi_{\lambda\mu\nu}$ can be permuted, which means $\chi_{\lambda\mu\nu} = \chi_{\lambda\nu\mu}$, because swamping $E_\mu(\omega)$ and $E_\nu(\omega)$ would leave LPGE part invariant. In addition, the second term $\mathbf{i}\gamma_{\lambda\kappa}(\mathbf{E}\times\mathbf{E}^*)_\kappa$ can be written as $\mathbf{i}\gamma_{\lambda\kappa}(E_1E_2^* - E_1^*E_2)_\kappa$, or sometimes simply written as $\hat{e}_\kappa P_{circ} E_0^2$. P_{circ} is the degree of circular polarization, $\hat{e}_\kappa$ is the unite vector pointing the light propagation direction and E_0 is the amplitude of the electric field of the light [102].

An discussion of LPGE and CPGE based on this equation are proposed in ref.[103]: the LPGE part does not contain time reversal symmetry, yet CPGE

part is invariant to time reversal which means CPGE and LPGE has totally different physical origins. Also as proposed in ref.[104], there are two contributions for the LPGE, ballistic current due to excitations and displacement of wave packet's center of mass in quantum transitions. As for CPGE, only the ballistic contribution exists.

In the view of the injection currents and the shift currents, as stated in the reference [105], the shift currents arise from a spatial shift of electron charges during excitations, while injection currents are generated by quantum interference between different optical pathways.

As for the mechanism of CPGE, the author of ref.[106] gives a clear explanation that CPGE contains two steps: photoexcitation, and followed by carrier scattering.

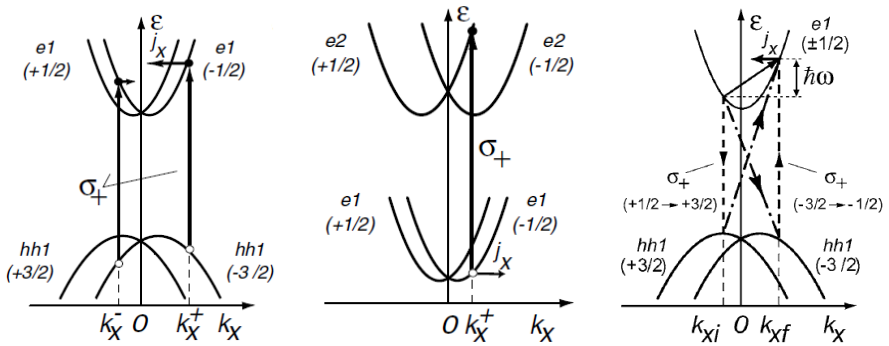

Figure 2.15: CPGE models proposed in ref.[107]. (a) inter-band transition. (b) inter-subband transition. (c) intra-subband transition. Figures are extracted from ref.[107].

As shown in Fig. 2.15, three types of CPGE are introduced in a review paper [107]: inter-band transitions Fig. 2.15(a), inter-subband transitions Fig. 2.15(b) and intra-subband transitions Fig. 2.15(c). In the case of the inter-band transition and inter-subband transition, the 'center of mass' of spin-up and spin-down electrons are not overlapping each other at $k_x = 0$ due to the spin splitting. Under circular illumination, conservation of the angular momentum causes the unbalanced excitation which results in a non-zero group velocity of the excited electrons [108]. Regarding the intra-subband transition, phonon takes part in the process. If a virtual process take place in different subbands, a spin current rather than a charge current would be generated [109].

It is suggested that the charge current generated by CPGE could be spin-polarized [107] which is appealing to device applications. So far, a lot of researches of CPGE have been done on materials like, topological insulators [13, 14, 110, 111, 18], spin-valley coupling system [15, 16], heave metal and quantum wells with strong SOC [11, 12, 112].

Photon drag effect

Another approach for Eqn. 2.80 to hold, i.e. the PDE scenario, is by modifying the equation to

$$\boldsymbol{j}_\lambda = \Xi_{\lambda\delta\mu\nu}(\omega) q_\delta \tilde{\boldsymbol{E}}_\mu(\omega) \tilde{\boldsymbol{E}}_\nu(-\omega). \tag{2.89}$$

Here $\Xi_{\lambda\delta\mu\nu}$ is the third-rank tensor and q_μ is the wave vector of the light. In this case, there is no symmetry constrains for the medium anymore.

Similar to PGE, PDE can also be divided into the circular photon drag effect (CPDE) and the linear photon drag effect (LPDE).

$$j_\lambda^{LPDE} = T_{\lambda\delta\mu\nu} q_\delta (E_\mu E_\nu^* + E_\mu^* E_\nu)/2 \tag{2.90}$$

$$j_\lambda^{CPDE} = D_{\lambda\delta\mu} q_\delta \mathbf{i} [\boldsymbol{E} \times \boldsymbol{E}^*]_\mu \tag{2.91}$$

Similar to the LPGE tensor χ_{ijk}, the last two indices of LPDE tensor $T_{\lambda\delta\mu\nu}$ can be permuted. However, for the CPDE pseudo tensor, the last two indices cannot be permuted, because they refer different meaning and generally they are not equal. In addition, totally opposite to PGE, the LPDE is even at time reversal and CPDE is odd at time reversal [113].

Photon drag effect is the electric current generated by momentum transfer from photons to electrons. This effect was experimentally observed in semiconductors at 1980 [114]. However most of the observations were LPDE. The reports of CPDE emerge only in recent years. CPDE was observed in quantum wells [115],bulk tellurium [116], topological insulators [117, 18] and in graphene [19, 118, 119]. The mechanism of CPDE is stated as a three-step process in ref.[115]: First, helicity and wave vector dependent photoexcitation. Then, the spin precess in an effective magnetic field. Finally, electric current caused by asymmetric spin relaxation.

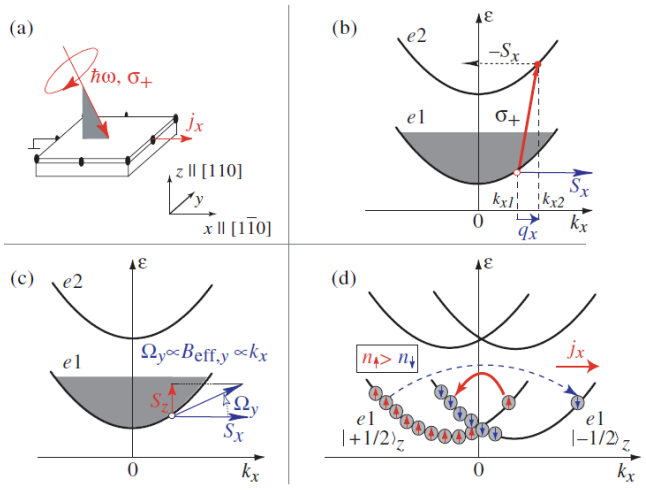

Figure 2.16: Sketch of PDE process in quantum wells from ref.[115]. (a) shows the experiment scheme of GaAs/AlGaAs QW. (b), (c) and (d) corresponding to step 1 to 3, respectively.

A microscopic model is shown in Fig. 2.16. PDE has a more restrict symmetry requirement than PGE, especially for CPDE. It might not be observable

simply, but once we have it, we can easily distinguish it from the incident angle dependence due to the requirement of both crystal symmetry and the wave vector of photon. According to [117], a calculation shows the frequency dependence of PGE and PDE in C_{3v} symmetry crystal. It can be seen that PGE and PDE current can be observed at a lower frequency range, and after a certain frequency both are attenuated while increasing photon frequency.

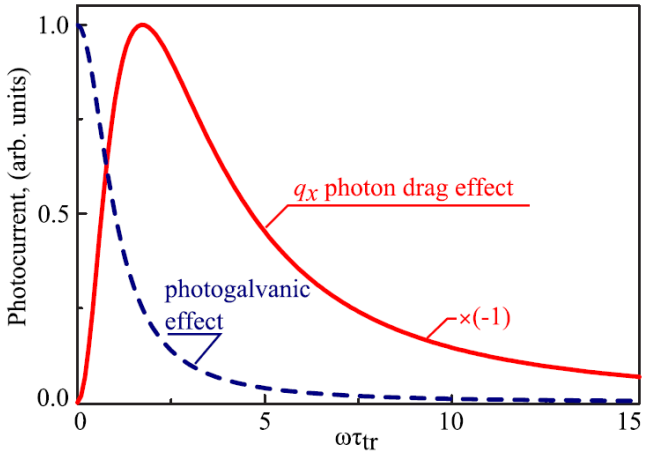

Figure 2.17: Frequency dependence for the photogalvanic and photon drag photocurrent. Figure is from ref.[117]. ω is the photon frequency and τ_{tr} is the transport relaxation time.

Spin-charge interconversion by inhomogeneous illumination

In addition to all the direct excitation of carriers, inhomogeneous illuminations could involve spin-charge interconversion as well, with the help of the gradient of heating or carrier densities. Early in 1984, Bakun *et al.* [120] used a circularly polarized light normally incident (z direction) on a bulk AlGaAs sample. A carrier density normal to the surface of the sample (Z direction) is created due to the illumination. Initially, spin is polarized along the incident direction, i.e. z direction. By applying a magnetic field in x direction some y direction spin is created. As a result, current is obtained in y direction by ISHE. Based on this idea, researchers found that with proper materials and experimental arrangement, the magnetic field can be remove to obtain the ISHE current [121, 122, 123, 124].

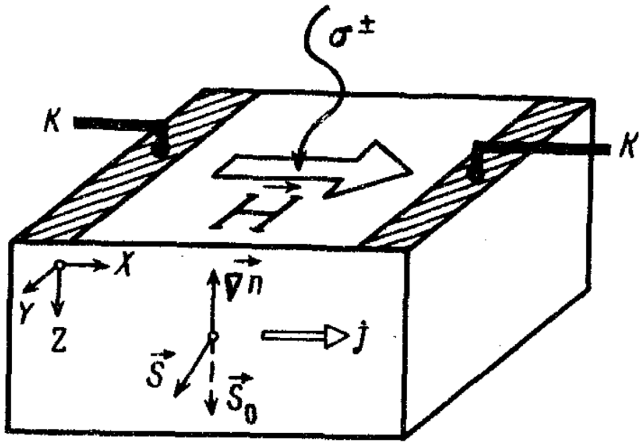

Figure 2.18: Arrangement for observing the photocurrent. Figure from [120].

Recently, a new phenomenon of spin separation by the thermal current is observed, which is called spin Nernst effect (SNE) [125, 126]. A spin current is generated by a thermal gradient $\boldsymbol{J}_s = \nabla T \times \boldsymbol{S}$. Under the inhomogeneous illumination by circularly polarized light, the laser heating would create a thermal gradient and the photoexcitation by circular polarization would generate spin polarized carriers, therefore could give rise to SNE.

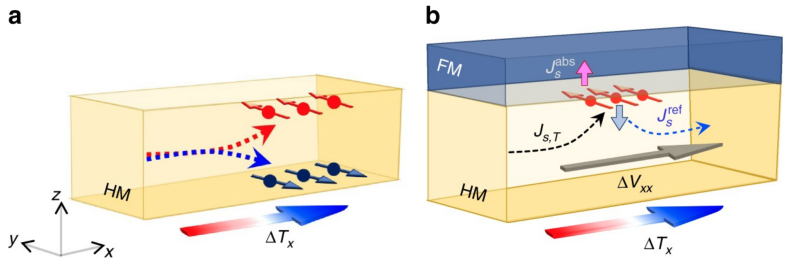

Figure 2.19: Schematics for SNE and spin Nernst magnetoresistance (SNMR). Figures are from [126]. (a) The temperature gradient in x-direction generates a spin current in z-direction with spin in y-direction. (b) A spin current induced in heavy metal by a temperature gradient in x-direction ($J_{s,T}$) partially reflected at the interface. Longitudinal (ΔV_{xx}) and transverse (ΔV_{xy}) are modified by the spin depended reflection at the interface. $\boldsymbol{J}_s^{abs}(\boldsymbol{J}_s^{ref})$ is the absorbed (reflected) spin current at the interface.

Chapter 3

Experimental methods

3.1 Optical setup

The apparatus used in this experiment basically can be divided into vacuum part and optical part. This system is built based on the setup of ref. [127] with some alternations, and the overall scheme is shown in Fig. 3.1.

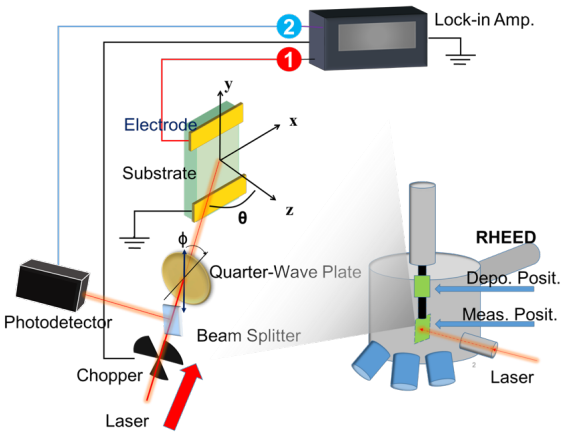

Figure 3.1: Schematic figure of experimental setup. LA: lock-in amplifier. PD: photodetector. BS: beam splitter. QWP: quarter wave plate. C: chopper. θ is the incident angle and ϕ is the angle between QWP's optical axis and linear polarization direction.

The apparatus contains mainly two chambers in its vacuum part, namely the load-lock chamber and the main chamber. Both film fabrications and measurements were done in the main chamber. The vacuum in the main chamber is supported by a rotary pump, a turbo, an ion pump and a titanium sublimation pump, with those the vacuum level is able to reach as low as $\sim 1 \times 10^{-10}$ Torr. The sample at the main chamber is capable of being cooled to as low as 27K with liquid He. Two magnets are located at the bottom of the main chamber and could supply $0 \sim 0.2$ T in-plane or out-of-plane magnetic field to the sample.

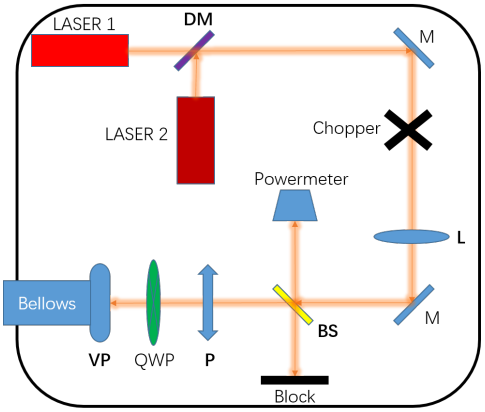

Figure 3.2: Scheme of the optical part of this experiment. DM: dichroic mirror. L: lens. BS: beam splitter. P: polarizer. VP: viewport. Bellows connect to the vacuum chamber.

In the optical part as shown in Fig. 3.2, two lasers are used, the wavelengths of the two are 635 nm and 1550 nm respectively. The light paths of the two lasers are carefully collimated by a dichroic mirror to align with each other, so we can use the visible laser to guide the setup roughly. A beam splitter is inserted into the light path to pick up the feedback of the laser intensity by a photodetector. After that the laser is linearly polarized by a Glan-Thompson prism which has an extinction ratio up to 5×10^{-5}. Then the linearly polarized light passes through a rotating quarter-wave plate (QWP) which would change the polarization of the light from linearly polarized to circularly polarized continuously. Later the light goes through a fused silica viewport perpendicularly and finally reaches to the surface of the sample in the main chamber.

The optical system needs to be carefully handled. First, the reflectance and transmittance of the p- and s-polarized light are different, and this could lead to artifact signal unless the light passes the optical compartments perpendicularly, so every transmitted optical element should be carefully aligned. In addition, the polarizer and the QWP must be put at the final stage of the light path, right before the light reaches the sample to keep the polarization. Second, due to the QWP used in this experiment is made from quartz, whose retardation is strongly dependent of the angle of incidence (AOI), it must be aligned carefully. Third, the viewport in the light path should be well protected to prevent from being contaminated during sample growth in the main chamber. And for optical use, strain-free viewport should be utilized, because strain across the viewport could cause retardation due to photoelastic effect. Last but not the least, the position of the light spot on the sample is difficult to adjust through the manipulator on the sample side (the manipulator will change horizontal and vertical position together, as well as the tilted angle). So, when adjusting that, in order to keep the light identical, the whole optical part, including the viewport, should be moved, rather than just adjusting any single part of the setup.

3.2 Lock-in technique

Lock-in technique is a powerful tool for experiments which attempt to collect signals from progressively smaller signals, weaker concentration and fainter excitation. Lock-in amplifiers can extract a small signal component at a specific frequency by using the phase-sensitive detection technique [128]. Noise signals

at other frequencies would not influence the output at all. Usually a signal we measured has several compositions:

$$V_{\text{sig}}(t) = V_0 + V_{\text{offset}} + V_{\text{white}}(t) + V_{\text{pink}}(t) \tag{3.1}$$

Here V_{white} means the white noise, also known as the Gaussian noise. This type of the noise fluctuates rapidly with time that the power spectrum is independent of the frequency up to $f \approx \tau^{-1}$, where τ is the correlation time of the white noise. The noise power goes to zero at a frequency higher than τ^{-1}. In addition, the expectation value over time of the white noise is zero [129]. A good way to get rid of the white noise is to take an average for a long time. And V_{pink} denotes the pink noise. The power spectrum shows a $1/f$ dependence, so it is also called as $1/f$ noise. Pink noise has been found in various systems such as, physical, biological even economic systems, some says it is ubiquitous [130].

If we can control the wanted signal V_0, like, switching the signal on and off at a certain frequency and take the difference. It is clear that the offset and the low-frequency signal almost makes no contribution to measured signal if the modulation frequency is high. After taking the average of the difference signal over time, only signal at modulation frequency is left (including noises and the wanted signal). For optical experiments, typical modulations include chopping beams with an optical chopper (100Hz–6kHz), or a combination of a photoelastic modulator (PEM) with a linear polarizer (100kHz), and simply using a PEM to modulate beams. The last type of modulation is particularly useful that eliminates all background signals which do not depend on the light helicity.

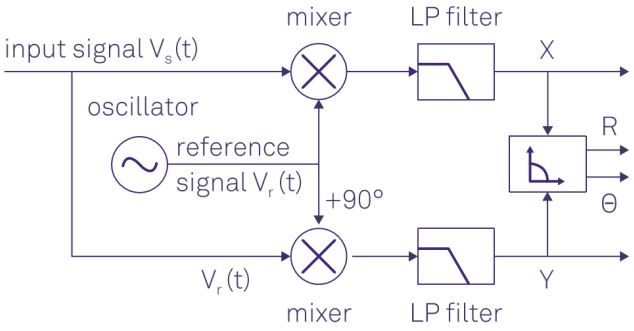

Figure 3.3: Schematic of the lock-in amplification: the input signal is multiplied by the reference signal. The mixer outputs are low pass filtered which eliminate the noise and the 2ω component, and finally converted into a polar coordinate[ii].

A modern lock-in amplifier can be seen as a combination of a phase sensitive detector (PSD) followed by a low pass filter as shown in Fig. 3.3. The chopping frequency provide a reference frequency ω_r to the PSD, and through a phase-locked-loop the lock-in amplifier will generate a reference signal $V_L \sin(\omega_L t + \theta_{\text{ref}})$ based on the reference frequency ω_r [128]. Fig. 3.4 shows this procedure.

[ii] Figure from https://www.zhinst.com/applications/principlesoflockindetection

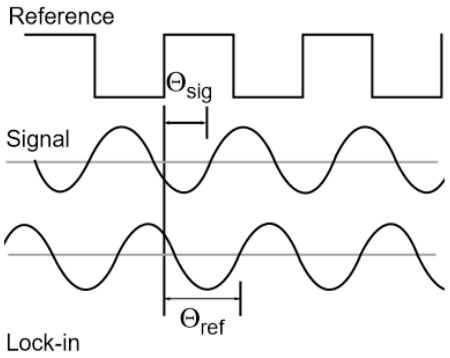

Figure 3.4: Reference, signal and lock-in signal generated from a PSD. Figure is from ref.[128].

The lock-in amplifier will amplify the signal and then multiplies it by a reference. The result of the mixer can be understood by trigonometric identities.

$$\sin(a)\sin(b) = \frac{1}{2}(\cos(a+b) - \cos(a-b)), \tag{3.2}$$

$$\cos(a)\sin(b) = \frac{1}{2}(\sin(a+b) - \sin(a-b)) \tag{3.3}$$

So, the results

$$\begin{aligned} V_{\mathrm{M1}} &= V_{\mathrm{sig}} V_{\mathrm{L}} \sin(\omega_{\mathrm{L}} t + \theta_{\mathrm{sig}}) \sin(\omega_{\mathrm{L}} t + \theta_{\mathrm{ref}}) \\ &= \tfrac{1}{2} V_{\mathrm{sig}} V_{\mathrm{L}} \cos([\omega_r - \omega_{\mathrm{L}}]t + \theta_{\mathrm{sig}} - \theta_{\mathrm{ref}}) \\ &\quad -\tfrac{1}{2} V_{\mathrm{sig}} V_{\mathrm{L}} \cos([\omega_r + \omega_{\mathrm{L}}]t + \theta_{\mathrm{sig}} + \theta_{\mathrm{ref}}) \end{aligned} \tag{3.4}$$

This output contains two AC signals, however if $\omega_r = \omega_{\mathrm{L}}$, i.e. lock-in frequency ω_L is the same as the reference frequency ω_r, the first term of Eqn. (3.4) becomes a DC term which proportional to the original signal that we want to measure. After the low pass filter, we can pick this signal out.

$$V_{\mathrm{out1}} = \frac{1}{2} V_{\mathrm{sig}} V_{\mathrm{L}} \cos(\theta_{\mathrm{sig}} - \theta_{\mathrm{ref}}) \tag{3.5}$$

If we have two PSDs with a reference angle θ_{ref} 90° shifted, we can exclude the phase dependence with two output commonly shown in a lock-in amplifier. The Lock-in amplifier solve this by using another mixer, with a reference input which is 90° out of phase [131]. The second reference input is $V_{\mathrm{ref}} \sin(\omega_r t + \theta_{\mathrm{ref}} - \pi/2)$, and the mixing signal is

$$\begin{aligned} V_{\mathrm{M2}} &= \frac{1}{2} V_{\mathrm{sig}} V_{\mathrm{L}} \cos(\theta_{\mathrm{sig}} - \theta_{\mathrm{ref}} - \pi/2) \\ &+ \frac{1}{2} V_{\mathrm{sig}} V_{\mathrm{L}} \sin(2\omega_r t + \theta_{\mathrm{sig}} - \theta_{\mathrm{ref}} - \pi/2) \end{aligned} \tag{3.6}$$

After filtering,

$$\begin{aligned} V_{\mathrm{out2}} &= \tfrac{1}{2} V_{\mathrm{sig}} V_{\mathrm{L}} \cos(\theta_{\mathrm{sig}} - \theta_{\mathrm{ref}} - \pi/2) \\ &= \tfrac{1}{2} V_{\mathrm{sig}} V_{\mathrm{L}} \sin(\theta_{\mathrm{sig}} - \theta_{\mathrm{ref}}) \end{aligned} \tag{3.7}$$

These are what we usually see on a lock-in amplifier as output X and Y.

$$X = V_{\text{sig}} \cos\theta\,, \quad Y = V_{\text{sig}} \sin\theta \tag{3.8}$$

$$\text{and} \quad R = \sqrt{X^2 + Y^2} = V_{\text{sig}} \tag{3.9}$$

Here $\theta = \theta_{\text{sig}} - \theta_{\text{ref}}$.

The CPGE current reported in former experiments [13, 14, 107] can be as low as around $1 \sim 10\,pA \cdot \text{mm}^2/\text{mW}$. In addition to promoting the laser power density, lock-in amplifier provides another sophisticated method to access to this weak signal.

3.3 Reflection high-energy electron diffraction

Reflection high-energy electron diffraction (RHEED), as well as low-energy election diffraction (LEED) are two methods widely used for surface science. Similar to x-ray diffraction (XRD), these two methods utilize diffraction patterns which are related with the reciprocal lattice structures. The main difference between XRD and RHEED/LEED is that XRD reveals the whole crystal structure, while, by selecting certain electron energy, RHEED and LEED are only sensitive to the surface structure.

The surface sensitivity of LEED is because that the electron interaction with the solid is strong at the low energy region. Rather than penetrating the whole crystal, the majority of electrons will lose kinetic energy during inelastic scattering processes, such as plasmon and phonon excitations as well as electron-electron interactions. As shown in Fig.3.5 which is known as the universal curve, the inelastic mean free path determines how far the electron goes into the sample. As for a typical surface region with a few atomic layers (5-10 $\mathring{A}$ thick), the corresponding energy is (20-200 eV). This attenuation ensures that the observation by LEED are dominated by the surface.

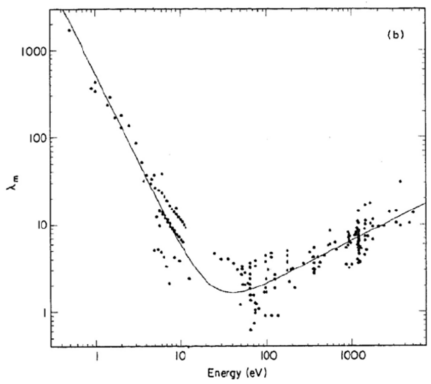

Figure 3.5: Inelastic scattering mean free path plotted vs the kinetic energy of electrons. Figure from [132].

In the case of RHEED, the small glancing angle of incidence allows electrons to escape from the bulk of the sample. And the atoms at the sample surface scatter the incident electrons and produce the diffraction pattern. There are two types of diffraction procedures contribute to the RHEED pattern. One is the kinematic diffraction, during which electrons goes through a single, elastic scattering at the sample surface. The high intensity spots or rings occur owing

to the kinematic scattering. The other procedure is called dynamical diffraction, where electrons undergo multiple but still elastic scattering in the crystal. In addition to these elastic scatterings, inelastic scatterings also contribute to the whole scattering patterns, they make the background but not the diffraction spots or rings. And for some of the inelastic electrons which fulfill Bragg diffraction conditions, Kikuchi pattern would be generated. Kikuchi lines are those faint lines connecting intense diffraction points. Kikuchi bands are dim ribbon structures. Scattering by small terraces and steps will broaden those Kikuchi features, therefore sharp Kikuchi patterns/lines infer a good morphology. Experimentally, sharp Kikuchi lines are usually obtained from crystals with perfect surfaces and perfect bulk lattices [133]. Besides providing the information about quality of the morphology, RHEED pattern could also provide some preliminary information about the surface status.

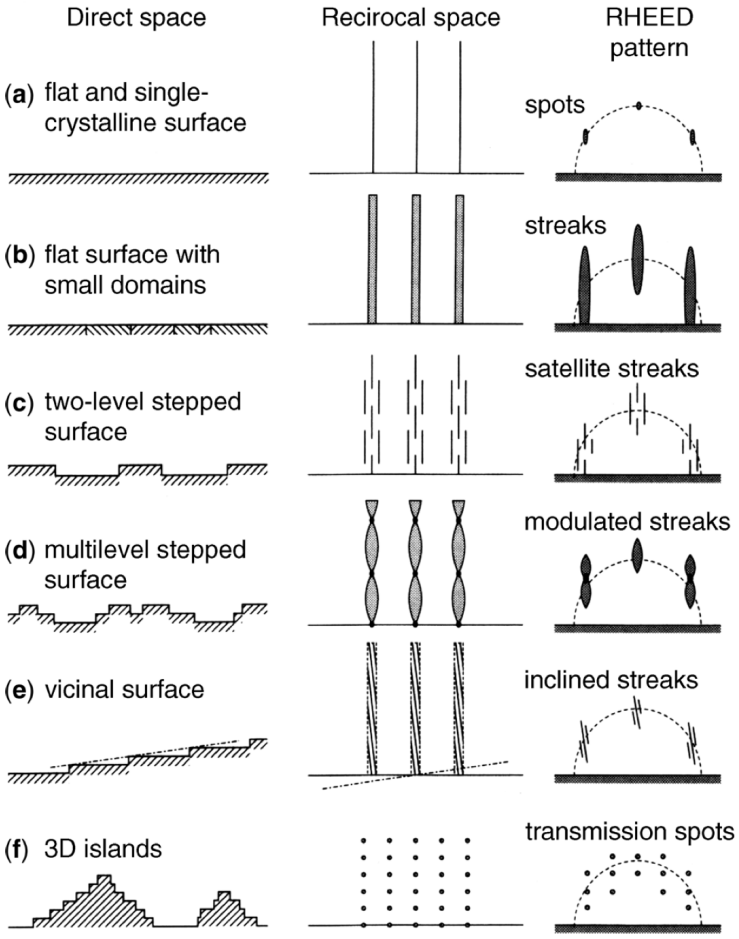

Figure 3.6: Real morphology, reciprocal space and RHEED pattern of various surfaces. Figure from [134].

An advantage of RHEED is that there can be a large open space in front of the sample where *in-situ* growth can be carried out [135]. The intensity change

of RHEED patterns reveal the growth style of the atomic layer on the surface. For the layer-by-layer growth, the oscillation of the RHEED intensity directly reflects how many layers have grown.

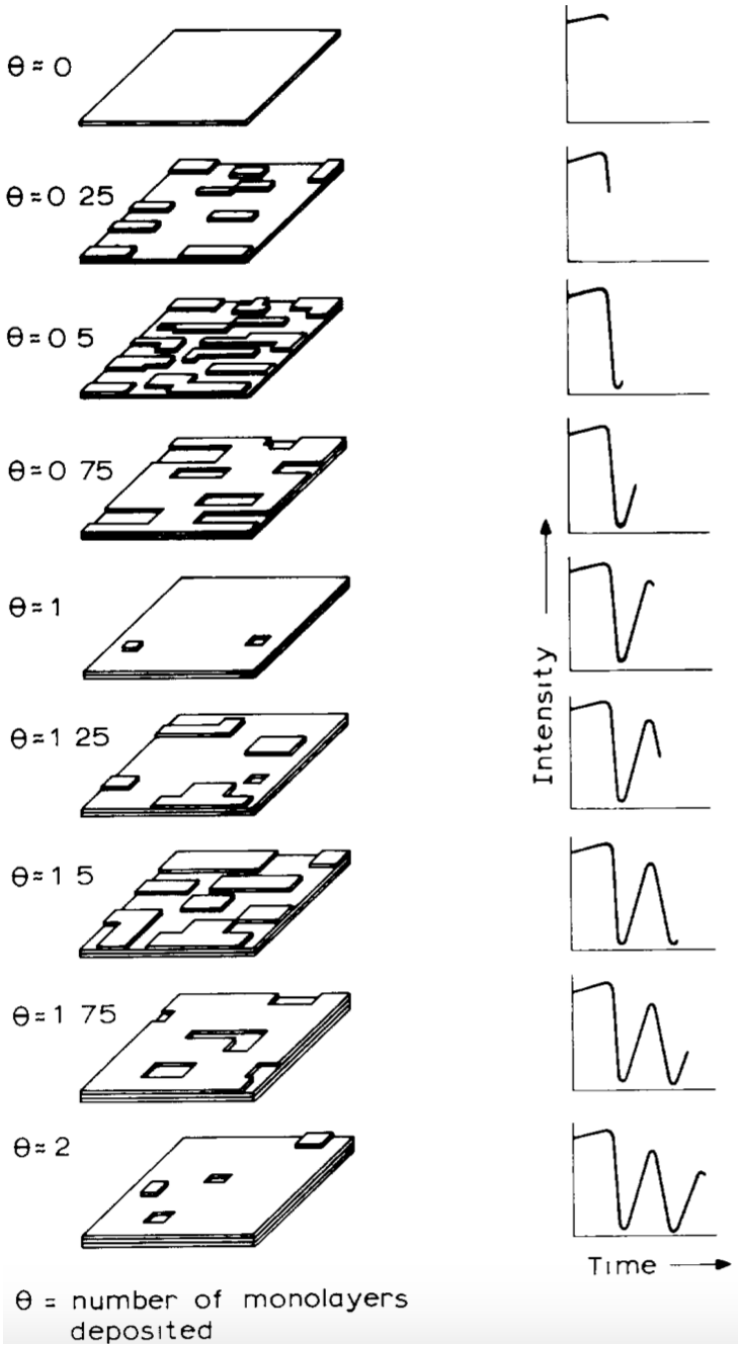

Figure 3.7: RHEED intensity oscillation during film deposition. Figure from [136].

Chapter 4

Materials

4.1 Bismuth

Bismuth is a chemical element with atomic number 83. The fresh bismuth metal is brittle with a silvery white color, but oxidation on the surface makes it pinkish. Bismuth is a natural diamagnetic element, thermal conductivity of it is also the lowest among other metals[i].

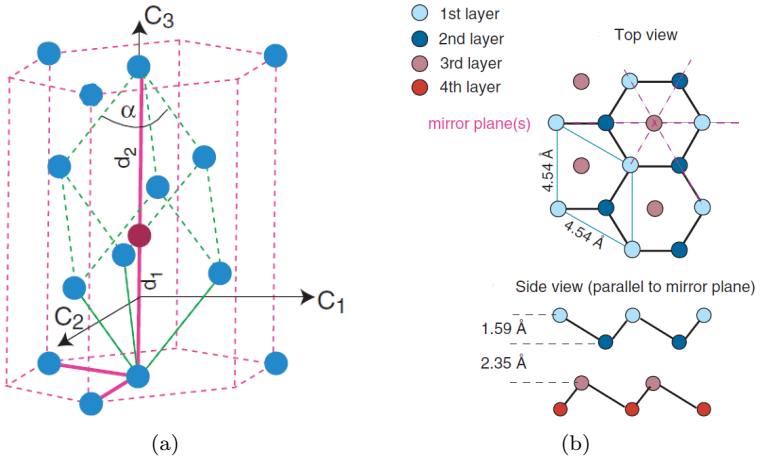

(a) (b)

Figure 4.1: (a) Bulk structure of the bismuth. Dashed green lines show the rhombohedral unite cell, and the dashed pink lines show the hexagonal unite cell. (b) Bismuth (111) plane structure. Figures are extract from ref.[137].

Same as other semimetal in group V, crystal bismuth shows the rhombohedral A7 structure. The crystal symmetry of bismuth is the space group $R\bar{3}m$-D^5_{3d}. As shown in Fig. 4.1(b), van der Waals force hold the atomic layers together, therefore bismuth could be cleaved easily along [111] direction [138]. [111] direction is also the preferred direction of epitaxial growth, as already demonstrated on the Si(111) surface [139].

[i]https://en.wikipedia.org/wiki/Bismuth

Due to the coexistence of metallic and covalent bonds, bismuth shows a very complex binding between atoms. In addition, as the nature of the heavy atoms, bismuth has a strong spin-orbit coupling which make Rashba spin-splitting possible in bismuth. For example, Bi(111) surface shows some interesting surface states and resonances [140]. The surface states which located near the Fermi level form electron pockets and hole pockets. Owing to these pockets, the surface states are more conductive than the bulk. Thus Hoffman *et al* suggest that surface states should dominate the physical properties of bismuth thin films [141]. In addition, surface states of Bi(111) shows a Rashba spin splitting observed in ARPES measurement [142]. It is said that the spin splitting on bismuth surface is expected to be 3 times bigger than that of Au (111) [143]. Moreover, the surface states of Au(111) are free-electron like and the spin splitting is classical Rashba type, but the surface states of Bi (111) are not free-electron like and the spin splitting are more complicate as shown in Fig. 4.2(a) [144]. Moreover, recent SRARPES (spin resolved ARPES) [145] implies that the band splitting derives from Rashba types, and ref.[145] shows that the in-plane spin polarization is suppressed yet out-of-plane spin greatly emerged. A recent theoretical paper shows that the surface states of Bi(111) are simply the results of hexagonal warping and Rashba effect [56].

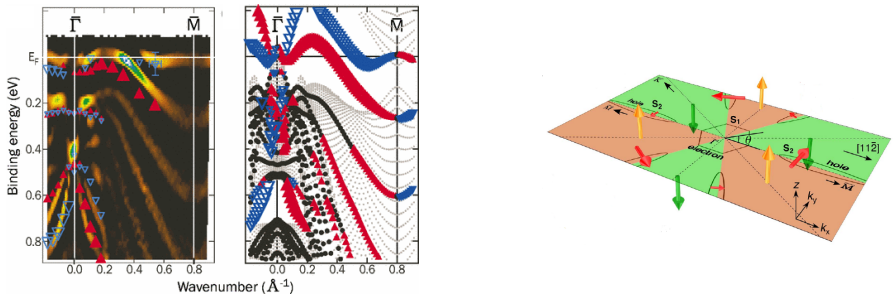

(a) (b)

Figure 4.2: (a) Bismuth spin splitting band extracted from ref.[144]. (b) The asymmetric spin structure on Bi/Si(111) from ref.[145].

As we previously calculated in Eqn.2.22, Berry's phase of a single subband of the Rashba states is nontrivial but ordinary Rashba states always possess two subbands encircle the TRIM point which makes the system trivial. However, with the great hexagonal warping effect, only one subband of Rashba states encircle the Γ point in bismuth which makes it a potential topological nontrivial material. Recent years, many attempts have been made on bismuth thin films because the quantum confinement converts Bi thin films from a semimetal to a semiconductor, which makes the idea of topological insulator possible. Theoretically, Bi(111) would be a topological insulator independent of film thickness [146, 147]. However, it is hard to verify since the band gap of bismuth is too small. Therefore experimentalists have to find another way to prove it in early days, such as to observe the strain induced topological phase transition [148], or to probe the band structure between two topological states [149]. Finally with enough resolution, we can directly observe the band structure [150, 151]. It is worth mentioning that in the high resolution ARPES measurement of ref.[151],

Ito *et al* prove that not just thin film but bismuth itself is topological nontrivial.

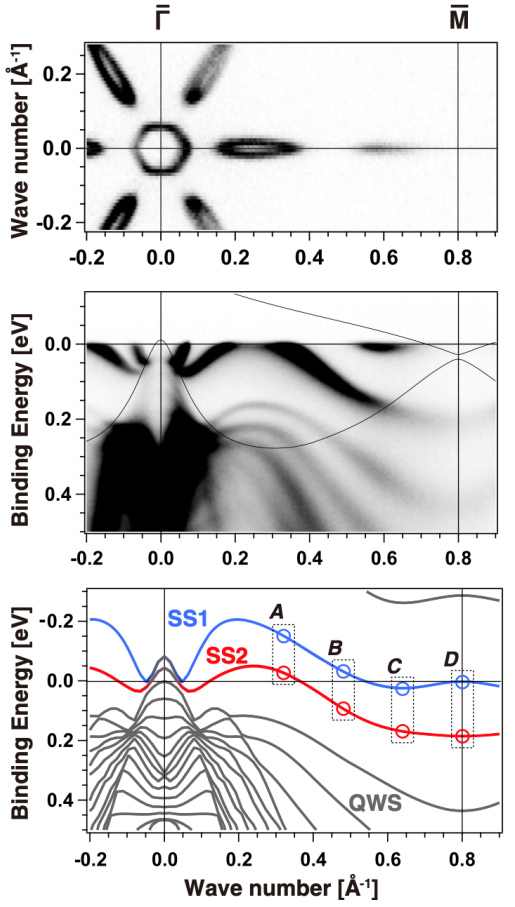

(a)

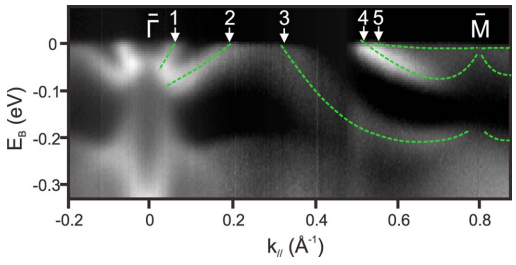

(b)

Figure 4.3: (a) 14 BL Bi(111) band calculation and experimental results extracted from ref.[151]. (b) Surface states of 30 nm $Bi/Bi_2Te_3(111)$ marked by green dashed line, from ref.[150]

4.2 Bismuth selenide

Bismuth selenide is known as a semiconductor and thermoelectric material in history, until 2010 when the topological surface states were observed by ARPES [152]. Bi_2Se_3 is a second generation of 3D TIs, with a large bulk band gap around 0.3 eV providing the possibility for room-temperature applications. The conduction band (CB) and the valence band (VB) near the Fermi level of bulk Bi_2Se_3 are mainly come from the p_z orbital, $p_{x,y}$ contributes 40% for VB and 20% for CB, as a result, surface states of Bi_2Se_3 are also predominated by p_z orbital, $p_{x,y}$ contributes around 40% and s orbital contributes less than 10% [153]. At ultrathin region (less than 6 QL), Rashba spin splitting bands rather than a topological Dirac cone appear at the bulk band gap of Bi_2Se_3 as shown in Fig. 4.2. The disappearance of the topological states is due to the overlapping between the front and back surface states of the Bi_2Se_3 [154].

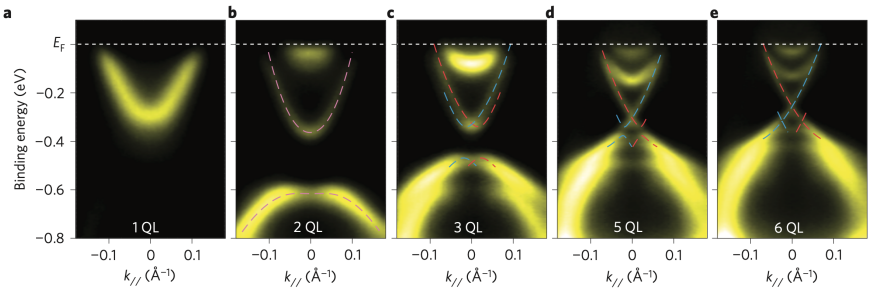

Figure 4.4: Bi_2Se_3 band evolution via changing thickness. Dirac cone appears after 6 QL. Figures are from ref.[154].

The topological surface states should be fully spin polarized, and shows spin-momentum locking as in the theory model Eqn. 2.39. However, a numerical calculation shows that the spin polarization of the TSS is just around 50% $\sim$ 60% close to the Γ point [155]. Author of ref.[155] suggests that due to the spin quantum number no longer conserve in a SOC system, the spin polarization would be reduced from 100% polarization. Experimentally, the spin polarization is said to be just around 20% [152]. The low magnitude of polarization would be problematic for spintronics application. However, another group reported with a higher resolution SRARPES and a TSS well separated Bi_2Se_3 sample said that the spin polarization actually is around 70% [156]. Their results also show the spin-momentum locking nature of the TSS. Another interesting feature of the Bi_2Se_3 that worth mentioning is, at the helical Dirac cone, not only spin but the orbit of the electron state is coupled with the momentum, as suggested in Ref.[157], verified by ARPES [158]. This coupling feature of Bi_2Se_3 may allow linearly polarized light selectively excite spin [159]. In addition, though the energy contour observed in various ARPES measurements show an almost perfect circle, hexagonal warping effect still impacts the spin structure of the helical Dirac cone [160]. A circular dichroism (CD) ARPES measurement shows that the z spin component exists at the helical Dirac cone of the Bi_2Se_3 [161]. Moreover, instead of a single helical Dirac cone, Bi_2Se_3 possesses a second Dirac surface states at around 1.8 eV above the first Dirac cone which is said to have the same properties as the first Dirac cone does [162]. Finally, despite the

topological Dirac surface state, a Rashba type 2DEG due to the quantum confinement also presents in Bi_2Se_3 as shown previously in Fig.2.7(b). Benia *et al* conclude these spin-splitting bands are the result of strongly spin-orbit coupled Bi $6p$ orbitals [163]. On the other hand, ref.[164] takes one step further suggesting that this kind of Rashba 2DEG is the result of the interplay between the quantum confinement and the topological order, and is general to all topological insulators. Though this Rashba 2DEG is not observed in [165, 166], a surface resonance state (SRS), which is believed to be intimately related with the TSS, is said to be the evolution of Rashba-like states through the SOI band inversion [166]. The SRS also shows spin-momentum locking and appears opposite spin direction as the TSS.

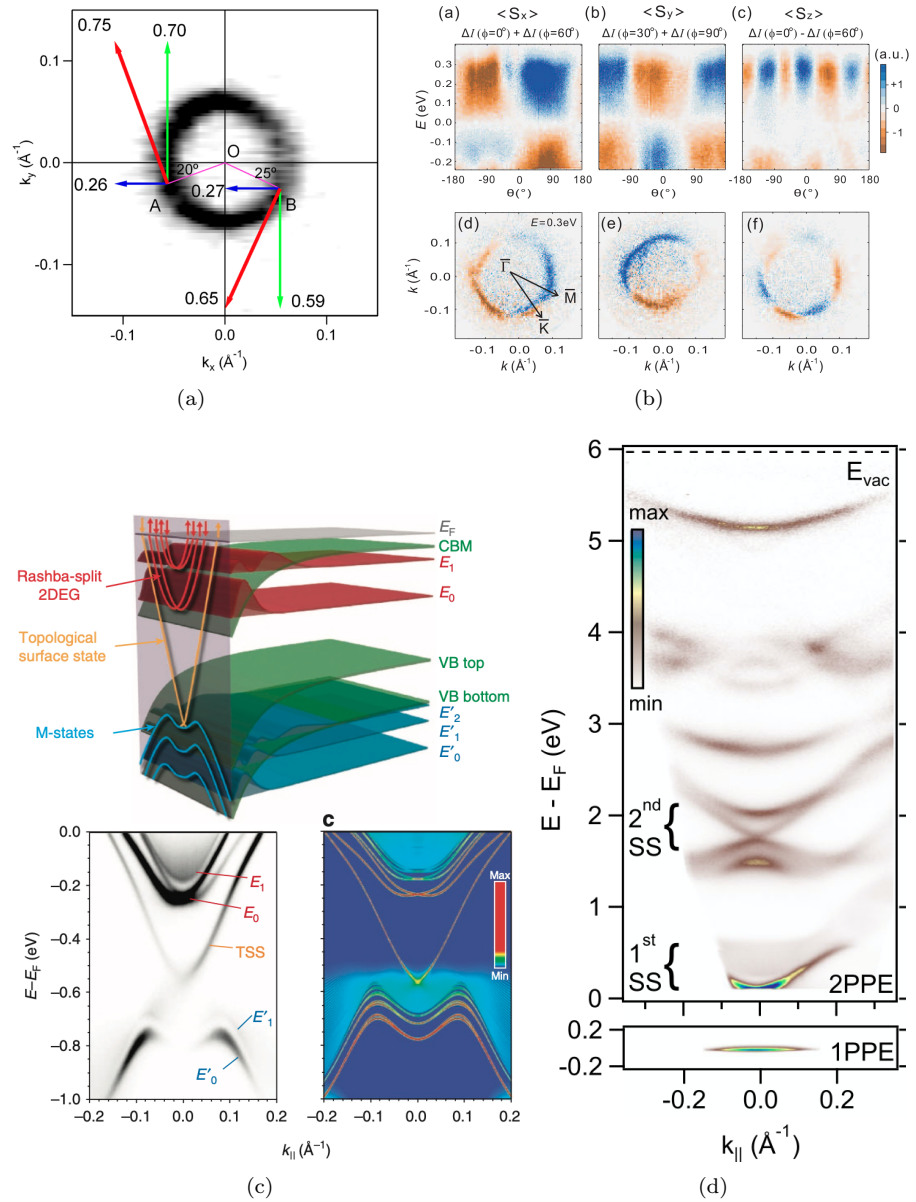

Figure 4.5: (a) TSS of Bi_2Se_3 extracted from ref.[156]. Red arrow is the total spin polarization, blue and green is for x and y component respectively. (b) Spin texture of TSS from ref.[161]. (c) Rashba 2DEG in Bi_2Se_3, extracted from ref.[164]. (d) Second Dirac surface states of Bi_2Se_3, extracted from [162]

4.3 Bismuth antimony telluride

Sb_2Te_3 and Bi_2Te_3 both belong to Z_2 class topological insulators, with the rhombohedral crystal structure and the lattice constant is 4.25 $\AA$ and 4.38 $\AA$ respectively. Sb_2Te_3 is naturally p-doped that the Dirac point is above the Fermi

level. To observe the Dirac cone experimentally, we need to either dope the mother material, or use a state-of-art technique, the time- and angle- resolved photoemission spectroscopy (TrARPES). The TrARPES results in ref.[167] reveal not only the uncoupled Dirac cone, but also the relaxation dynamics of the electrons in the Dirac cone. Despite the TSSs, Sb_2Te_3 also hosts other surface states. Wang *et al* observed a M-shape surface states near the Dirac TSSs [168]. The M-shape surface states appear when the film thickness is greater than 3 QL and the location is close to the quantum well states in thicker films. Another surface state is observed around 0.8 eV under the TSSs. This surface states show giant Rashba splitting with a Rashba factor $\alpha_R \sim 1.4$ eV $\mathring{A}$ [169]. This value is much larger than the Rashba states observed in Bi_2Se_3 0.36 eV $\mathring{A}$ [57]. The spin polarization in this Rashba states is as high as 45% whereas the polarization could reach to $80 \sim 90\%$ in the Dirac cone of Sb_2Te_3 according to [169].

Comparing with the 0.21 eV band gap of Sb_2Te_3, Bi_2Te_3 has a smaller band gap 0.15 eV. Bi_2Te_3 is naturally n-doped which means the Fermi level crosses the TSSs as well as the bulk CBs, which gives the opportunity to observe the TSSs directly by ARPES. The Dirac cone of the Bi_2Te_3 appears like a hexagram due to the hexagonal warping effect as shown in Fig.2.9. As previously discussed in Sec.2.3, the hexagonal warping enabled the out-of-plane spin polarization in the Dirac cone that can reach 25% polarization at ΓK direction. Meantime the in-plane polarization is around 60% at Fermi level [58]. Similar to Bi_2Se_3, Bi_2Te_3 also owns another TSSs at 1.3 eV above the Fermi level [170]. Besides, Bi_2Te_3 also possesses surface resonance states with spin-orbital coupling features [171].

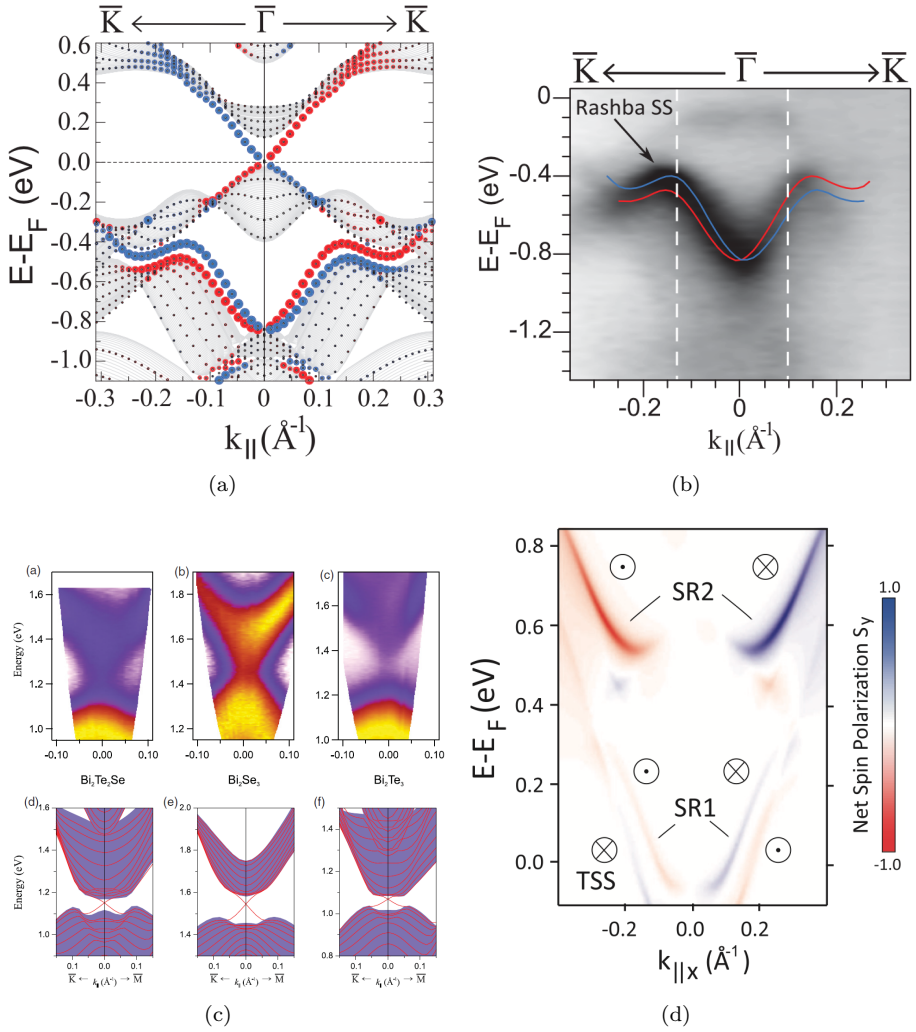

Figure 4.6: (a) Calculation and (b) ARPES data of Rashba states in Sb_2Te_3, extracted from [169]. (c) Second TSSs of Bi_2Te_3 obtained from [170]. (d) Surface resonant states (SR) above the TSS of Bi_2Te_3, extracted from [171].

A good thing for Sb_2Te_3 and Bi_2Te_3 is that the small lattice mismatch gives the possibility to "blend" two materials together. The advantage of mixing the two is that charging compensation of the naturally n-doped Bi_2Te_3 and p-doped Sb_2Te_3 could achieve a true bulk insulating TI [172].

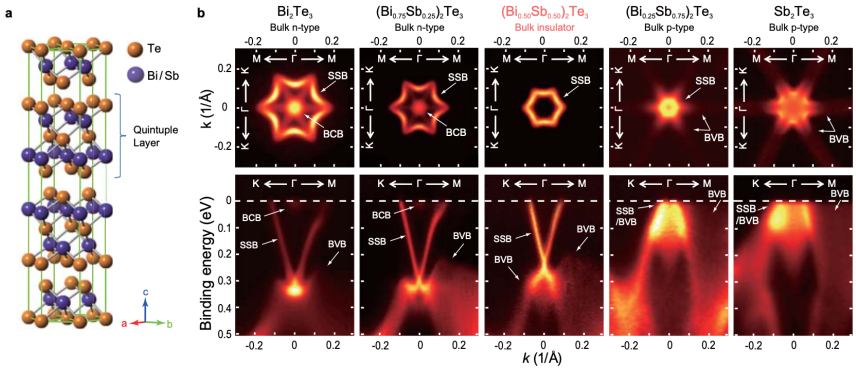

Figure 4.7: (a) Crystal structure and (b) band evolution when changing the Bi and Sb ratio. Figures are from [173].

Chapter 5

Results and discussion

5.1 Experimental expectation

All the samples are epitaxially grown on [111] oriented silicon substrates, therefore we set the x-axis along a mirror plane containing [11$\bar{2}$] direction of the silicon substrate, as shows in Fig. 5.1.

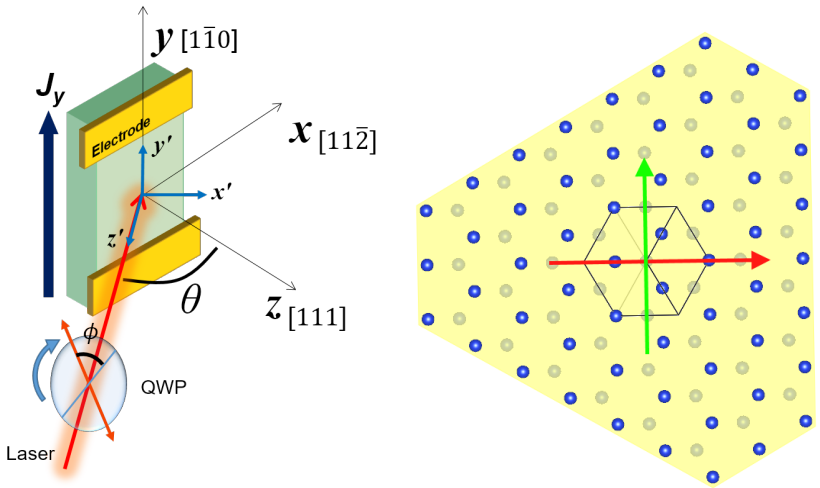

(a) (b)

Figure 5.1: (a) Sample mounting scheme. Experimental coordinates xyz and light polarization coordinates $x'y'z'$. Initially, light is s-polarized which is along y' axis. The angle of incidence (AOI) is θ and the quarter waveplate (QWP) rotation angle is ϕ.(b) Si(111) lattice. Red arrow indicates [11$\bar{2}$] direction and the green one refers [1$\bar{1}$0]

First, we will estimate the light absorption in the films, clearly if the absorption is low the photocurrent should be very weak. The absorption is mainly determined by the extinction coefficient of the material.

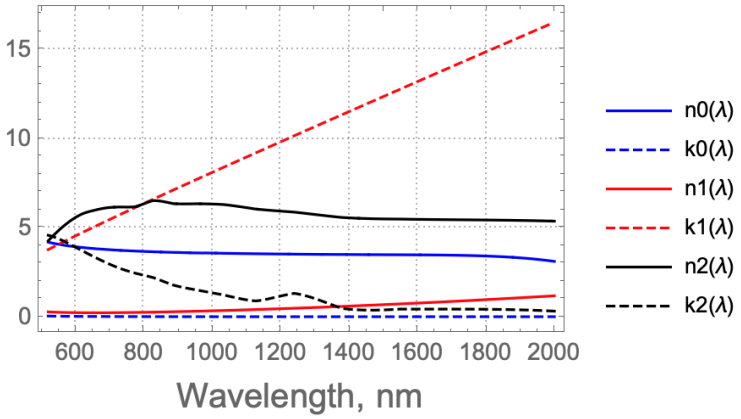

Figure 5.2: Refractive indices ($\tilde{n} = n + ik$) of silicon (n0, k0) from ref.[174], bismuth (n1, k1) from ref.[175] and Bi_2Se_3 (n2, k2) from ref.[176]. Solid lines are the real part and dashed lines are the imaginary part of the complex refractive indices.

	λ(nm)	n	κ	$\alpha(\text{nm}^{-1})$	δ_p(nm)
Bi	635	0.223	4.869	0.104	9.645
	1550	0.720	12.789	9.64×10^{-2}	10.378
Bi_2Se_3	635	5.881	3.550	7.03×10^{-2}	14.233
	1550	5.485	0.428	3.47×10^{-3}	287.893
Si	635	3.860	0.015	3.06×10^{-4}	3262.74
	1550	3.480	0	0	∞

Table 5.1: Real (n) and imaginary part (κ) of the complex refractive index, absorption coefficient (α), and calculated penetration depth δ_p from Eqn. 2.67. Silicon band gap is 1.12eV, so basically no light absorption occurs if photon energy is lower than 1.12eV.

If we use Eqn. 2.65 to calculate the absorbance, which relies on the extinction coefficient κ only, incorrect values will be obtained because the interferences are ignored. Using Eqn. 2.72 to calculate we will find out there is a big difference between the two results. The following calculations of R, T, A are assumed at normal incidence.

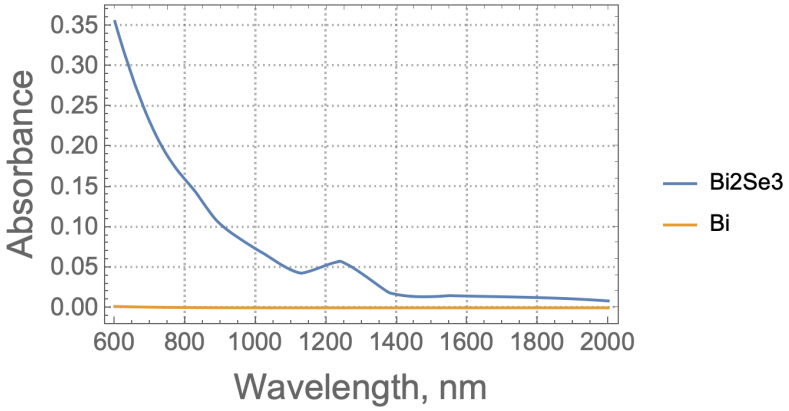

(a)

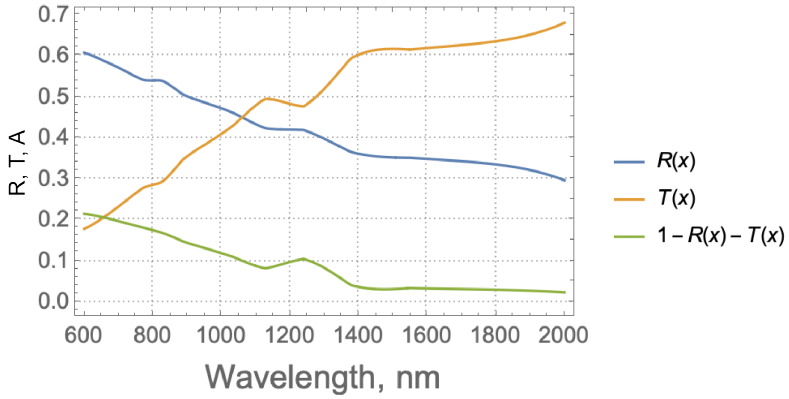

(b)

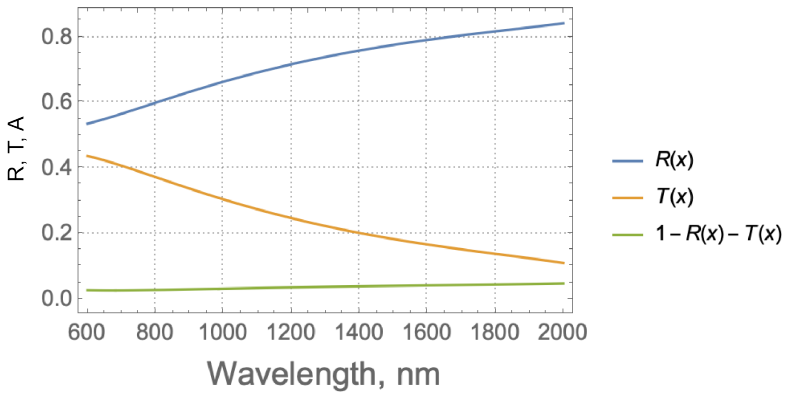

(c)

Figure 5.3: (a) Absorbance at normal incidence calculated using Eqn. 2.65. R, T and A calculated using Eqn. 2.72 for a 10 nm thick (b) Bi_2Se_3 and (c) Bi thin films on Si substrates.

From the comparison of the calculation results by two equations in Fig.5.3(a) and (b)(c), we can see that thin film interference raised the absorbance of the

material over all wavelengths. Besides, the large value of the extinction coefficient of Bi results in a high reflectance, but not a high absorbance. Whereas, low magnitude of the extinction coefficient of Bi_2Se_3 in the long wavelength region yields a low absorbance accordingly. The absorbance for Bi_2Se_3 at 1550 nm is $\sim 3\%$ while $\sim 21\%$ at 635 nm. The absorbance for Bi at 1550 nm is $\sim 4\%$ while $\sim 3\%$ at 635 nm. The absorbance would increase at oblique incidence.

Next we will calculate transfer matrices and tensors related with material properties. Luckily, all the samples we used here belong to $R\bar{3}m$-D^5_{3d} space group, so one calculation will solve all the materials. This symmetry group contains (1) a three-fold rotation along the (111) axis; (2) mirror reflection in plane a, b, c as in Fig.5.4; and (3) an inversion symmetry.

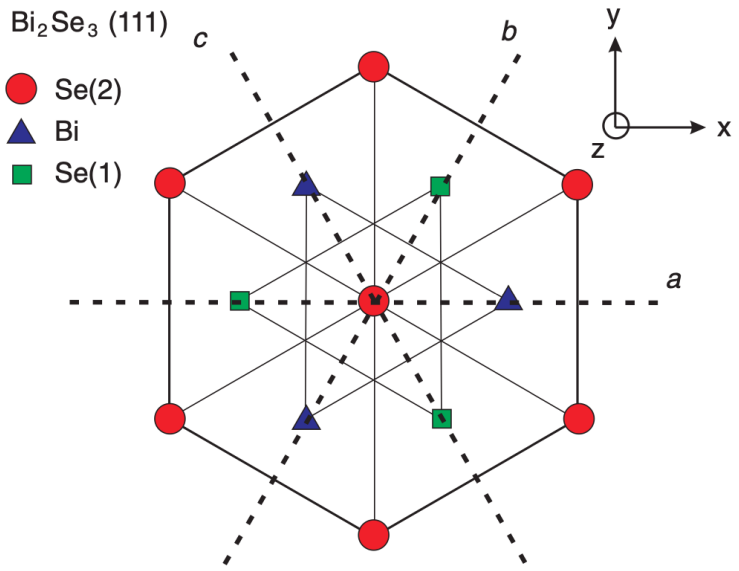

Figure 5.4: Take Bi_2Se_3 as an example to show the symmetry. Figure is from [177].

Three-fold-rotation symmetry gives the rotation matrix:

$$C_{3(z)} = \begin{pmatrix} \cos 120^\circ & \sin 120^\circ & 0 \\ -\sin 120^\circ & \cos 120^\circ & 0 \\ 0 & 0 & 1 \end{pmatrix} = \begin{pmatrix} -\sqrt{3}/2 & 1/2 & 0 \\ -1/2 & -\sqrt{3}/2 & 0 \\ 0 & 0 & 1 \end{pmatrix} \tag{5.1}$$

The mirror plane along x-axis:

$$\sigma_x = \begin{pmatrix} 1 & 0 & 0 \\ 0 & -1 & 0 \\ 0 & 0 & 1 \end{pmatrix} \tag{5.2}$$

Inversion symmetry:

$$I = \begin{pmatrix} -1 & 0 & 0 \\ 0 & -1 & 0 \\ 0 & 0 & -1 \end{pmatrix} \tag{5.3}$$

First, as we mentioned in Sec.2.5 that PGE requires the crystal to lack of an inversion center. However, D_{3d}^{5} group has inversion symmetry which means that PGE would not take place in the bulk of our samples, only at the surface where the inversion symmetry is broken.

Assuming the second-rank pseudo tensor for CPGE is

$$\gamma = \begin{pmatrix} \gamma_{xx} & \gamma_{xy} & \gamma_{xz} \\ \gamma_{yx} & \gamma_{yy} & \gamma_{yz} \\ \gamma_{zx} & \gamma_{zy} & \gamma_{zz} \end{pmatrix} \tag{5.4}$$

to calculate this pseudo tensor of C_{3v} symmetry, following

$$\gamma'_{ab} = T_{ai}T_{bj}|T|\gamma_{ij} \tag{5.5}$$

where γ_{ij} is the pseudo-tensor element in old coordinates, T_{ai} is element of the transforming matrix, $|T|$ is the determinant of the transforming matrix, and γ'_{ab} is the pseudo-tensor element after the transformation. For a system which possesses such symmetry, γ should equal to γ'. Following Eqn.5.5 we get:

$$\gamma' = \begin{pmatrix} 0 & \gamma_{xy} & 0 \\ -\gamma_{xy} & 0 & 0 \\ 0 & 0 & 0 \end{pmatrix} \tag{5.6}$$

Similarly, we can calculate the third-rank tensor χ_{abc} for LPGE. The transforming rules for tensor is:

$$\chi'_{abc} = T_{ai}T_{bj}T_{ck}\chi_{ijk} \tag{5.7}$$

Then we have the third-rank tensor of C_{3v}

$$\chi' = \begin{pmatrix} \begin{pmatrix} \chi_{xxx} \\ 0 \\ \chi_{xxz} \end{pmatrix} & \begin{pmatrix} 0 \\ -\chi_{xxx} \\ 0 \end{pmatrix} & \begin{pmatrix} \chi_{xzx} \\ 0 \\ 0 \end{pmatrix} \\ \begin{pmatrix} 0 \\ -\chi_{xxx} \\ 0 \end{pmatrix} & \begin{pmatrix} -\chi_{xxx} \\ 0 \\ \chi_{xxz} \end{pmatrix} & \begin{pmatrix} 0 \\ \chi_{xzx} \\ 0 \end{pmatrix} \\ \begin{pmatrix} \chi_{zxx} \\ 0 \\ 0 \end{pmatrix} & \begin{pmatrix} 0 \\ \chi_{zxx} \\ 0 \end{pmatrix} & \begin{pmatrix} 0 \\ 0 \\ \chi_{zzz} \end{pmatrix} \end{pmatrix} \tag{5.8}$$

Next we determine the light polarization by Stokes vectors. The light is initially linearly polarized in y direction which,

$$S_{in} = \begin{pmatrix} 1 \\ -1 \\ 0 \\ 0 \end{pmatrix} \tag{5.9}$$

The light passes through a rotating quarter waveplate (QWP) before it reaches the sample. The QWP can be expressed by

$$C_{\mathrm{QWP}} = \begin{pmatrix} 1 & 0 & 0 & 0 \\ 0 & 1 & 0 & 0 \\ 0 & 0 & \cos\pi/2 & \sin\pi/2 \\ 0 & 0 & -\sin\pi/2 & \cos\pi/2 \end{pmatrix} = \begin{pmatrix} 1 & 0 & 0 & 0 \\ 0 & 1 & 0 & 0 \\ 0 & 0 & 0 & 1 \\ 0 & 0 & -1 & 0 \end{pmatrix} \tag{5.10}$$

with the rotation matrix (rotating QWP, the fast axis of QWP makes an angle ϕ with initial polarization direction of the light):

$$R(\phi) = \begin{pmatrix} 1 & 0 & 0 & 0 \\ 0 & \cos 2\phi & \sin 2\phi & 0 \\ 0 & -\sin 2\phi & \cos 2\phi & 0 \\ 0 & 0 & 0 & 1 \end{pmatrix} \tag{5.11}$$

So before reaching the sample, the outcome light can be calculated by

$$\boldsymbol{S}_{out} = \boldsymbol{R}(\phi)\boldsymbol{C}_{\mathrm{QWP}}\boldsymbol{R}(-\phi)\boldsymbol{S}_{in} = \begin{pmatrix} 1 \\ -\cos^2(2\phi) \\ 1/2\sin(4\phi) \\ \sin(2\phi) \end{pmatrix} \tag{5.12}$$

In our setup, the photocurrent was measured along y-axis, in the case of normal incidence, following Eqn. (2.88). By considering the nonzero elements of γ and χ

$$\begin{aligned} j_y &= \chi'_{yxy}[E_x E_y^* + E_x^* E_y]/2 + \chi'_{yyx}[E_y E_x^* + E_y^* E_x]/2 + \mathrm{i}\gamma'_{yx}(\mathbf{E} \times \mathbf{E}^*)_x \\ &= -\chi_{xxx}[E_x E_y^* + E_x^* E_y] - \mathrm{i}\gamma_{xy}(E_y E_z^* - E_z^* E_y) \end{aligned} \tag{5.13}$$

Then we can use Stokes vectors (Eqn. (2.84-2.87)) to represent electric fields.

$$j_y = -\frac{1}{2}\chi_{xxx}\sin 4\phi \tag{5.14}$$

Because lacking the z-component of electric fields under normal incidence, CPGE is prohibited, only LPGE is allowed. And this coincides with former experimental reports on materials with C_{3v} symmetry [13, 14, 15].

In the case of oblique incidence, besides amplitude alteration of χ'_{yxy} term, E_z-component would be generated. Thus additional χ'_{yyz} would contribute to LPGE, which is $\cos 4\phi$ term. However, because of the restriction of γ', no additional terms are added in the CPGE part, just the amplitude is altered in respect of the incident angle, i.e. the projection on E_z gives a $\sin\theta$ factor. Considering the transmittance, we finally have the total current of PGE,

$$j_y = t_s t_p(a\,\gamma'_{yx}\sin 2\phi\,\sin\theta + b\,\chi'_{yxy}\sin 4\phi\,\cos\theta + c\,\chi'_{yyz}\cos 4\phi\,\sin\theta + d) \tag{5.15}$$

where a, b, c, d are factors and t_s, t_p is transmittance of s-wave (E_y component) and p-wave (E_x or E_z), respectively. Direct from Fresnel equations we have

$$t_s t_p = \frac{4n\cos^2\theta}{(\cos\theta + \sqrt{n^2 - \sin^2\theta})(n^2\cos\theta + \sqrt{n^2 - \sin^2\theta})} \tag{5.16}$$

n is the refractive index of the film. This equation works for materials whose refractive index is predominated by the real part. Usually imaginary part of the complex refractive index cannot be ignored for high conductive materials like metals. The Fresnel equation should be rewritten in its original form, since the refractive angle cannot be deduced from Snell's law when the refractive index is complex.

$$\begin{aligned} t_s &= \frac{2\cos\theta}{\cos\theta + \tilde{n}\cos\theta_t}, \\ t_p &= \frac{2\cos\theta}{\tilde{n}\cos\theta + \cos\theta_t}. \end{aligned} \tag{5.17}$$

Here $\tilde{n} = n + i\kappa$ is the complex refractive index of the metallic film, and θ_t is the refractive angle which can be get from [178]

$$\theta_t = \arcsin \frac{\sin\theta}{\sqrt{\frac{1}{2}(\sqrt{(n^2-\kappa^2-\sin^2\theta)^2+4n^2\kappa^2}+(n^2-\kappa^2+\sin^2\theta))}} \tag{5.18}$$

For simplicity we have the fitting function for current written as[i]

$$j_y = C\sin 2\phi + L_1 \sin 4\phi + L_2 \cos 4\phi + D \tag{5.19}$$

where factor C represents circular polarization related photocurrent (i.e. the helicity dependent photocurrent (HDP)), L_1 and L_2 are for linear polarization related photocurrent, and D is the polarization independent photocurrent.

In the view of the incident plane, as shown in Eqn. 5.13, when the incoming light makes a azimuthal rotation, the current may have a complex variation against azimuthal angle φ. In the CPGE case, the term $i\gamma_{xy}(E_y E_z^* - E_z^* E_y)$ always requires a E_y projection, so the CPGE current will shows a $\sin\varphi$ dependent behavior as reported from ref. [14]. As for the incident angle, when light incident angle changes $\theta \to -\theta$, i.e. incident-direction projection on x-axis $\hat{e}_x \to -\hat{e}_x$, CPGE current would reverse its direction ($E_y \to -E_y$) as in refs. [14, 179, 180]. However LPGE current of this system, χ'_{yxy} have $E_y E_x \to E_y E_x$, which means no sign changing; for χ'_{yyz}, $E_y E_z \to -E_y E_z$. These angles dependence shown in the following figures Fig. 5.5.

[i] In real experiment setup, the light coordinates rotated 45° around Z' axis in Fig.5.1 for observing the photocurrent difference between $s+p$ wave and circular polarization, this rotation would give raise to cos term in Eqn.5.19.

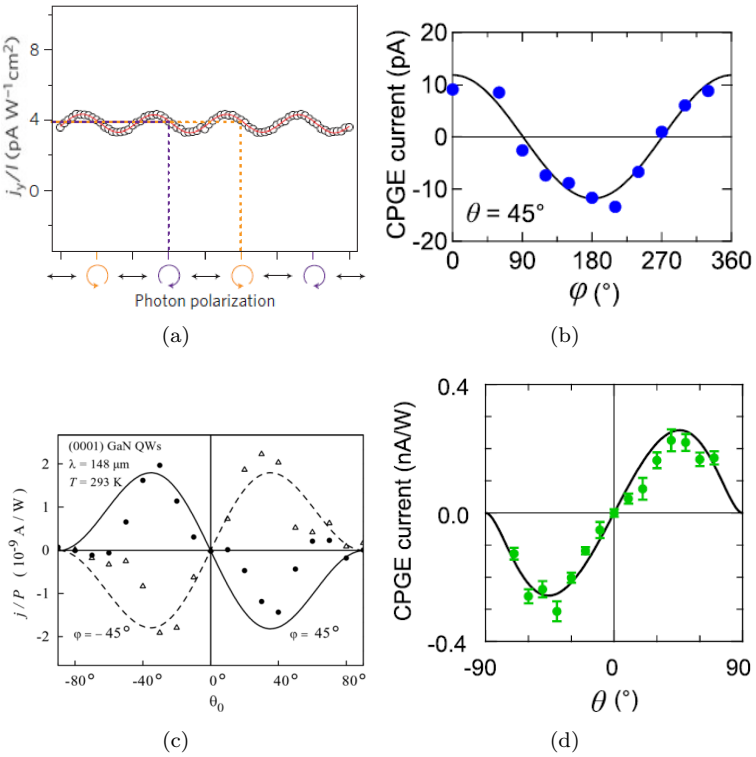

Figure 5.5: (a) Normal incidence on Bi_2Se_3, no $\sin(2\phi)$ part (CPGE), only $\sin(4\phi)$ term (LPGE) exists [13]. (b) Azimuthal rotation angle φ under 45° incidence, CPGE current have a $\sin\varphi$ pattern [14]. (c) CPGE current incident angle θ dependence of GaN quantum well with consideration of the transmittance[iii]. Current direction reverses if reversing the incident angle [179]. (d) Incident angle θ dependence of $(Bi_xSb_{1-x})_2Te_3$ [14].

If other effects also contribute to the total current, the result may also be fitted by Eqn. 5.19. Because simply considering the rotation of QWP, we can say that the current related to linear polarization have a 4ϕ periodicity and current related to circular polarization have a 2ϕ periodicity. However, additional analysis like incident angle dependence, position dependence could distinguish them.

Contribution from CPDE

Next we are going to take into account PDE. Because we are interested in the HDP, we mainly focus on CPDE which might have a different incident angle dependence compared with CPGE. Noted here that PDE have no symmetry restriction so both bulk and surface could be the source of PDE. CPDE current written as Eqn. 2.91

$$j_{CPDE} = D_{\lambda\delta\mu} q_\delta \mathbf{i}[\boldsymbol{E} \times \boldsymbol{E}^*]_\mu \tag{5.20}$$

[iii]Though GaN QW possess a different symmetry, the pseudo tensor of CPGE is identical with that of C_{3v} symmetry.

Following the transformation rule for the third-rank pseudo tensor we have the same pseudo tensor for C_{3v} symmetry surface and D_{3d} symmetry bulk.

$$D'_{abc} = T_{a\lambda}T_{b\delta}T_{c\mu}|T|D_{\lambda\delta\mu} \tag{5.21}$$

$$D' = \begin{pmatrix} \begin{pmatrix} 0 \\ D_{xxy} \\ 0 \end{pmatrix} & \begin{pmatrix} D_{xxy} \\ 0 \\ D_{xyz} \end{pmatrix} & \begin{pmatrix} 0 \\ D_{xzy} \\ 0 \end{pmatrix} \\ \begin{pmatrix} D_{xxy} \\ 0 \\ -D_{xyz} \end{pmatrix} & \begin{pmatrix} 0 \\ -D_{xxy} \\ 0 \end{pmatrix} & \begin{pmatrix} -D_{xzy} \\ 0 \\ 0 \end{pmatrix} \\ \begin{pmatrix} 0 \\ D_{zxy} \\ 0 \end{pmatrix} & \begin{pmatrix} -D_{zxy} \\ 0 \\ 0 \end{pmatrix} & \begin{pmatrix} 0 \\ 0 \\ 0 \end{pmatrix} \end{pmatrix} \tag{5.22}$$

Since xz plane is the incident plane, photon wave vector q and propagation direction e cannot be in y direction, the possible photocurrent combination in y direction is

$$j_y = D_{xxy}q_xP_{circ}E^2e_x - D_{xyz}q_xP_{circ}E^2e_z - D_{xzy}q_zP_{circ}E^2e_x \tag{5.23}$$

q_xe_x gives $\sin^2\theta$ incident angle dependence and q_ze_x gives $\sin 2\theta$ incident angle dependence.

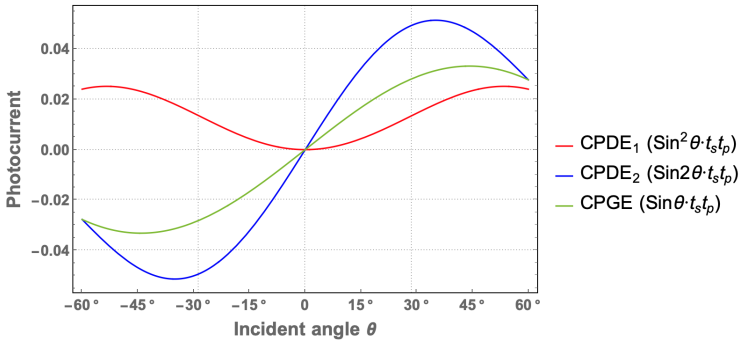

Figure 5.6: Overall incident angle dependence of CPGE and CPDE when taking refractive index $\tilde{n} = 5.88 + 3.55i$. $CPDE_1$ and $CPDE_2$ denote the two terms in Eqn.2.91. Note that peak position (periodicity) of CPGE and $CPDE_2$ is different. However, when fitting the experimental results these two terms may not be distinguishable if data points are not enough. But symmetric $CPDE_1$ can be separate from $CPDE_2$ and CPGE easily, once presented.

The primary expectation from the experiments is HDP, which consists of CPGE and CPDE in these films, and from the incident angle dependence we might be able to distinguish some parts of them. However, the straightforward method to separate CPDE and CPGE is by illuminating sample from front and back both sides [181]. It is worth mentioning that though PGE and PDE for a certain material are determined by these tensors, the frequency response could be different, e.g. CPGE dominant in low frequency but CPDE dominant in high frequency, since those tensors are a function of the optical frequency as in Eqn. 2.80.

5.2 Photocurrent in Si(111)

Silicon substrates were used in this experiment for MBE samples growth. A typical substrate size is 3 mm × 13 mm cut from a n-type Si(111) wafer whose resistivity is $1 \sim 5\Omega cm$. After being clamped by two tungsten plates at both ends as electrodes, roughly 3 mm × 8 mm area is exposed for deposition. Normally since silicon wafer is covered by a natural oxide layer of few nanometers ($\sim 10nm$) thick, a pretreatment is needed before sample growth. Si(111) substrate is set at ~ 650°C for degassing and removing the oxide layer around 8 hours in the UHV chamber. Then Si(111)-7 × 7 reconstructed surface is prepared by quenching after flush heating at ~ 1200°C to remove SiC and the oxide layer.

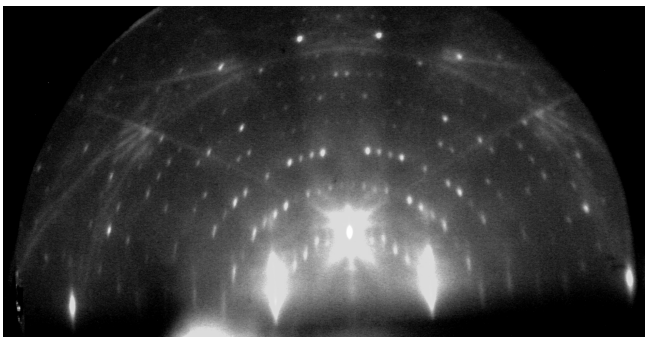

Figure 5.7: A RHEED pattern of Si(111)-7 × 7 reconstructed surface. Spotty pattern and Kikuchi pattern infer good morphology.

Photocurrent of Si(111) substrate was measured before and after the heating process. As shown in Fig. 5.8 (a), almost no photocurrent was observed on the pristine Si(111) substrate either by 1550 nm or by 635 nm illumination; the data points are scattered due to the lock-in amp. could not lock in a certain frequency since the signal is too small. After being prepared as Si(111)-7 × 7 surface reconstruction, an obvious amount of photocurrent was observed by both 635 nm and 1550 nm. This probably due to the emergence of the surface states of Si(111)-7 × 7, or the defects states generated during the heating process. Moreover, no clear HDP was observed either by changing the incident angle or illuminating the edge of the substrate.

Angle of incidence (AOI) dependence of HDP was measured on Si(111)-7 × 7 substrate by both 635 nm and 1550 nm. By fitting Eqn. 5.19 reveals a very small HDP, as shown in Fig. 5.9. Although it is not reliable to conclude that HDP is observed on Si(111)-7 × 7 substrate by fitting the scattering data points, we still plot the AOI dependence of the fitting results in Fig. 5.9. It is clear that no obvious AOI dependence was observed.

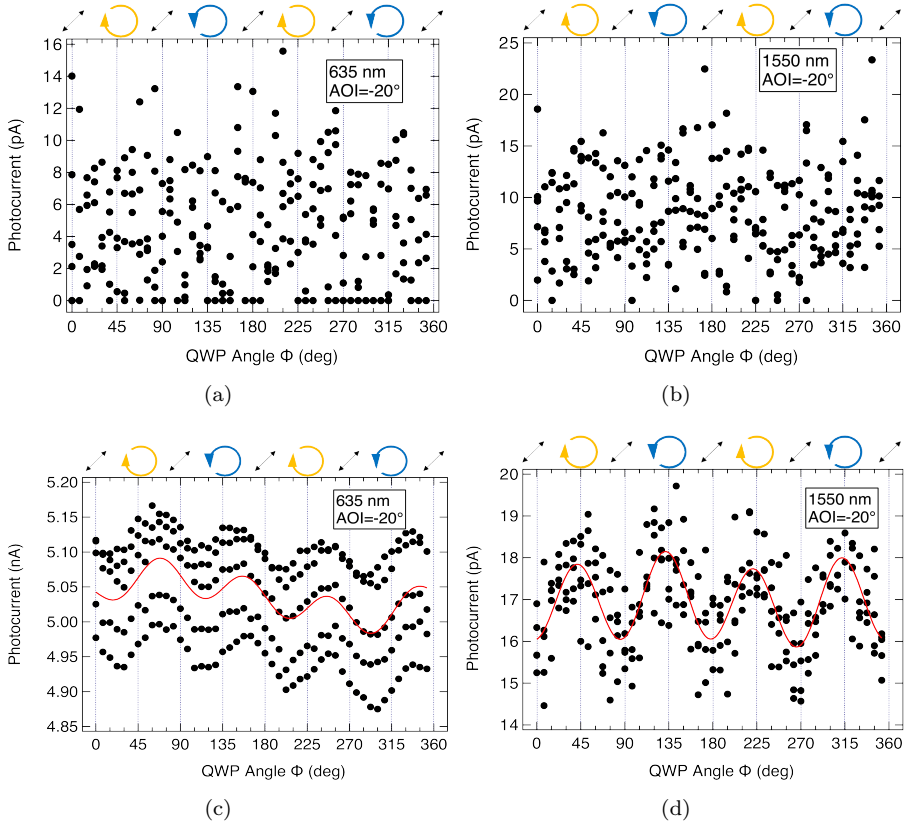

Figure 5.8: (a), (b) Photocurrent on the pristine Si(111) and (c), (d) on Si(111)-7×7 at $-20°$ degree incidence by both 635 nm and 1550 nm illumination. Almost no photocurrent was observed on the pristine Si(111), but a countable photocurrent was observed after thermal treatment though the data points are scattered.

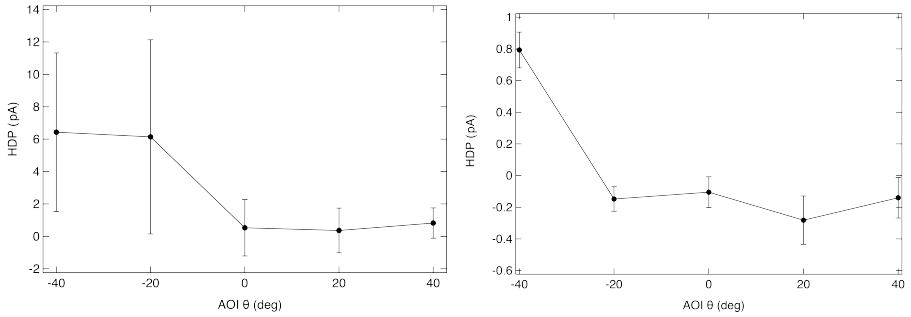

(a) (b)

Figure 5.9: AOI dependence of HDP from fitting (if any) was plotted by both (a) 635 nm and (b) 1550 nm illumination. HDP is very small and no clear AOI dependence was observed.

Position dependence at normal incidence was also measured from the left edge to the right edge of the sample. No position dependence was observed either as shown in the figure below.

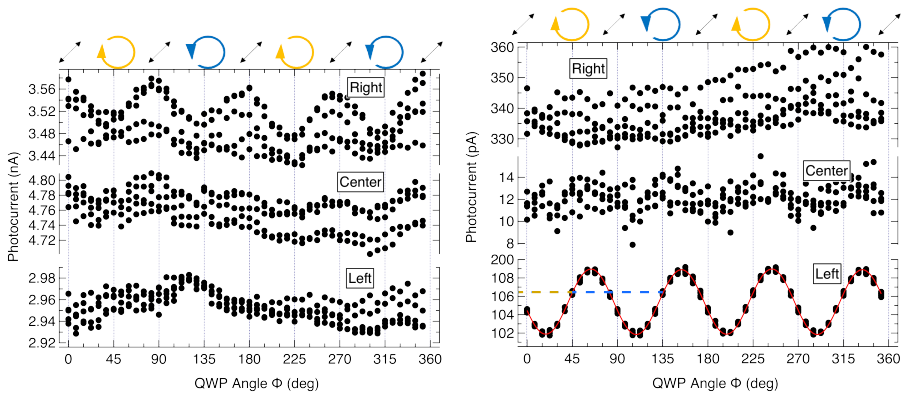

(a) (b)

Figure 5.10: Position dependent photocurrent at normal incidence was measured by (a) 635 nm and (b) 1550 nm. No systematic position dependence was observed. Some polarization dependent photocurrent was observed at the left edge of the sample but without HDP.

5.3 HDP in bismuth selenide thin films

5.3.1 Growth of bismuth selenide thin films

Growth of Bi_2Se_3 films by molecular beam epitaxy (MBE) on the Si(111) substrate was reported in ref.[182] by evaporating Bi in Se rich ambient, and a layer-by-layer growth mode was observed by RHEED. Usually the flux ratio of Bi and Se should be set to over 1:10 when using Knudsan cell. This is because the Se source is mainly composed of Se tetramers Se_4 whose decomposition is

not efficient [183]. One problem may occur when growing Bi_2Se_3 on the top of Si(111) substrate, as mentioned in ref.[182], is that the interface layer usually forms $SiSe_2$ amorphous structure. An alternative way is to grow β-$\sqrt{3} \times \sqrt{3}$-Bi/Si(111) before growing Bi_2Se_3 on it. But some suggests that the morphology of the Bi_2Se_3 films on the Bi-terminated $\sqrt{3} \times \sqrt{3}$ surface is not good, especially in the thinner region that the bulk is not insulating until 24 QL thick [184]. Though this could simply because of the Se vacancy or charge transfer from the substrate. Moreover, it is reported that vicinal Si(111) substrate will efficiently suppressing defects and the domain twining during growth [185].

The samples of the following experiments were prepared on the β-Bi-$\sqrt{3} \times \sqrt{3}$/Si(111) superstructure, following the method written in [186]. A sharp 1×1 RHEED pattern can be obtained after the growth of Bi_2Se_3 which infers a good quality of the film, as shown in Fig.5.11(a). When tracking the intensity of the (00) diffraction spot in the RHEED pattern, an oscillation was acquired with the periodicity around 4 min, as in Fig.5.11(b), suggesting the layer-by-layer growth fashion at a growth speed of 4 min/QL. The oscillation is not always observable, especially when the substrate temperature is high ~ 260°C. This is due to the growth mode change to step-flow mode which is said to be of better quality than layer-by-layer growth mode [187, 188].

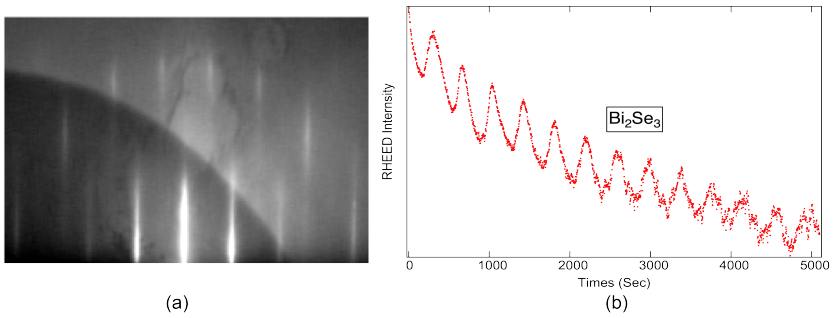

Figure 5.11: (a) 1×1 RHEED pattern of Bi_2Se_3. (b) RHEED intensity oscillation during growth.

5.3.2 AOI dependent HDP

When measuring the polarization-dependent photocurrent, there is a clear oscillation of the photocurrent intensity when changing the polarization of light by a quarter-wave plate (QWP). Initially, the light is linearly polarized when the optical axis of the QWP aligned with linear polarization (LP). The QWP rotating counterclockwise to create LP (0°)–RCP (45°)–LP (90°)–LCP(135°)–LP (180°) in a 180° cycle depending on the angle between the optical axis of the QWP and the initial polarization direction. It is clearly shown in Fig.5.12 that the photocurrent at RCP and LCP is slightly different, which is observed under both 635 nm and 1550 nm lasers illumination.

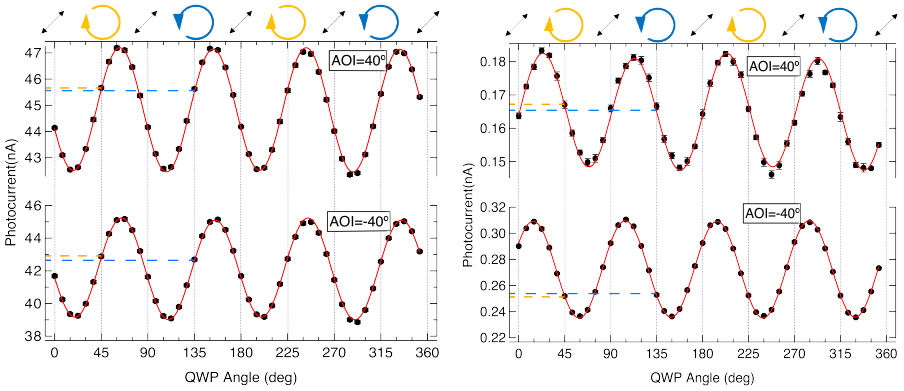

(a) (b)

Figure 5.12: Polarization-dependent photocurrent observed in a 4 QL Bi_2Se_3 film by both (a) 635 nm and (b) 1550 nm wavelength illuminations at the center of the sample. HDP also presented as shown by the indicators. However, HDP at 635 nm wavelength illumination does not reverse when the angle of incidence (AOI) changes from 40° to -40°, whereas HDP at 1550 nm wavelength illumination reverses.

Data is fitted by Eqn. 5.19. Parameter C is corresponding to HDP, L_1 and L_2 represent LP photocurrent which could be LPGE, LPDE or anomalous LPGE [189]. Parameter D represents polarization independent photocurrent which is originated from the photo Dember effect and/or thermal effect. It seems that both datum of 635 nm and 1550 nm wavelength illumination show circular dichroism. Before we jump to the conclusion of CPGE, we need to examine the incident angle dependence of the HDP. As we calculated earlier, AOI dependence can be fitted by:

$$J_{\mathrm{HDP}} = a_1 \sin 2\theta \cdot t_s t_p + a_2 \sin^2\theta \cdot t_s t_p + a_3 \sin\theta \cdot t_s t_p. \tag{5.24}$$

Here, a_1 and a_2 represent the CPDE and a_3 represents CPGE.

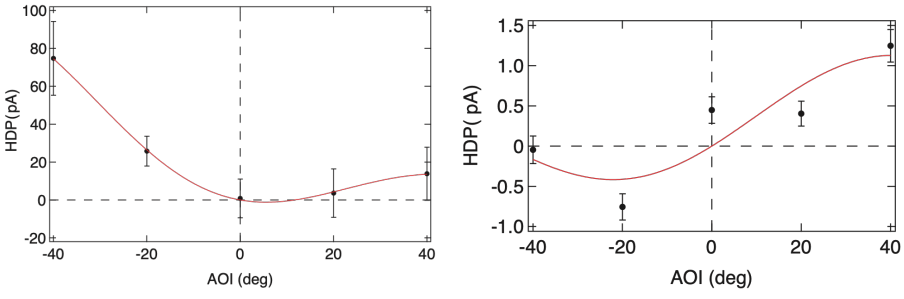

(a) (b)

Figure 5.13: AOI dependence of HDP in a 4 QL Bi_2Se_3 film under (a) 635 nm and (b) 1550 nm wavelength illuminations, fitted by Eqn. 5.24. AOI dependence of HDP at 635 nm wavelength illumination shows a more symmetric behavior than that at 1550 nm wavelength illumination.

It is clear from Fig. 5.13 that the AOI dependence of HDP is different between 635 nm wavelength illumination and 1550 nm wavelength illumination . Under 635 nm wavelength illumination, a symmetrical AOI dependence is dominant. However, the HDP at 1550 nm wavelength illumination shows more antisymmetrical. As we deduced in Fig.5.6, CPDE component will show a symmetrical behavior when changing the incident angle. It is clear that CPDE is observed here in Bi_2Se_3.

As mentioned earlier, usually CPDE and CPGE are not distinguishable. Though we have a fitting function as in Eqn. 5.24, fitting parameters a_1 and a_3 should be correlated with each other since our AOI range could only varies from $-40°$ to $40°$. However, with the special property of topological insulators, i.e. topological surface states appear only after a certain thickness. For Bi_2Se_3 the critical thickness is 6 QL[154]. So if the HDP shows a drastic change over different thickness, it could be concluded that the HDP is originated from TSSs by the mechanism of CPGE.

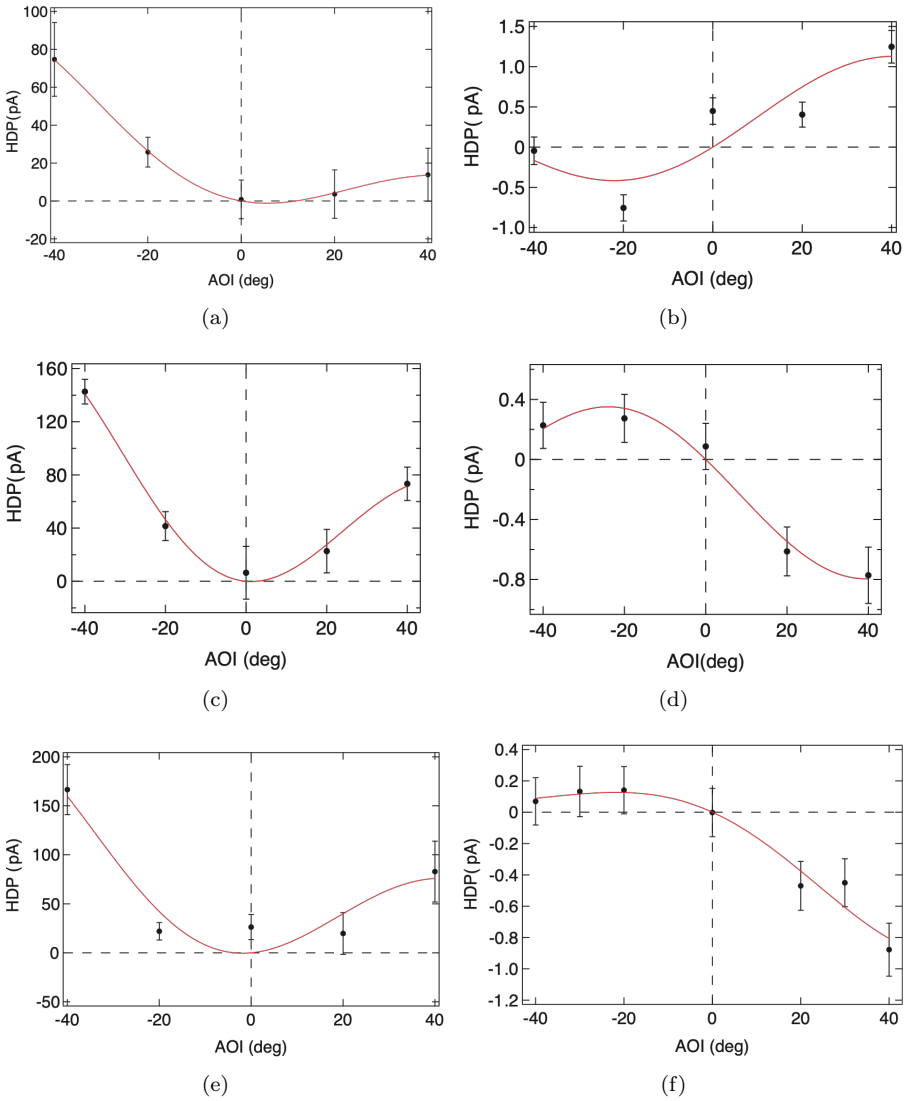

Figure 5.14: AOI dependence of HDP at 635 nm and 1550 nm wavelength illuminations in Bi_2Se_3 films of (a)(b) 4QL, (c)(d) 7QL and (e)(f) 10 QL thick. AOI dependence of HDP at 635 nm wavelength illumination (a)(c)(e) shows a more symmetric behavior than that at 1550 nm wavelength illumination (b)(d)(f).

To clarify the origin of the HDP, thickness dependent of HDP was measured on 4 QL, 7 QL (±1QL) and 10 QL (±1QL) Bi_2Se_3 films, that thicker films are deposited on thinner films successively. Due to the higher substrate temperature during deposition, no RHEED oscillation could be observed so there might be a ±1 QL error in thickness judging by deposition time. As a result, shown in Fig.5.14, it can be seen that the AOI dependence of the HDP measured at 635 nm wavelength illumination does not change so much when thickness increased, whereas that at 1550 nm wavelength illumination fundamentally changed after 4 QL thickness. Besides, the HDP at 1550 nm wavelength illumination decreased

a little when the film thickness is increased. This may not be related with the band structures changes of the film, but due to the illumination position shifts in y direction. Position dependent thermal current by laser heating is revealed by many papers [13, 18, 190], such thermal current will cause the average group velocity of electrons changes, therefore will increase or decrease the HDP consequently [18].

5.3.3 Discussion

Though ref.[13] excludes the CPDE in their experiments by stressing the spin degeneracy in bulk Bi_2Se_3. However, as it is observed in Ag/Pd nanocomposite [191], or even in material lack of SOC as graphene [113], CPDE seems to have very weak requirements on the presence of spin splitting bands. On the other hand, CPDE in materials of D_{3d} symmetry also has a antisymmetric component as in Fig.5.6. It appears that the HDP observed by 1550 nm also contains CPDE since the AOI dependence is not total antisymmetric.

As for the band origin of the HDP, a previous two-photon photoemission (2PPE) study [192] shows that the light couples to TSSs of Bi_2Se_3 revealing a clear circular dichroism pattern, and this process is not photon-energy sensitive. Later, Soifer *et al* concludes that HDP can be only excited by through resonant optical transitions which coupling to SOC states with broken inversion symmetry [193]. These findings support that the HDP existence in various wavelength ranges, and suggest the HDP could carry different properties since different SOC states could host the HDP.

For the excitation paths of our experiments, by comparing the band calculation results of Bi_2Se_3 from ref.[193], we conclude that 1550 nm wavelength excitation is more probably related with TSSs than 635 nm wavelength excitation. Moreover, the HDP could come from the spin-flip excitation within TSSs, as the path (1) in Fig.5.15; or orbital selected excitation path, as paths (2), (3) and (4) in Fig.5.15.

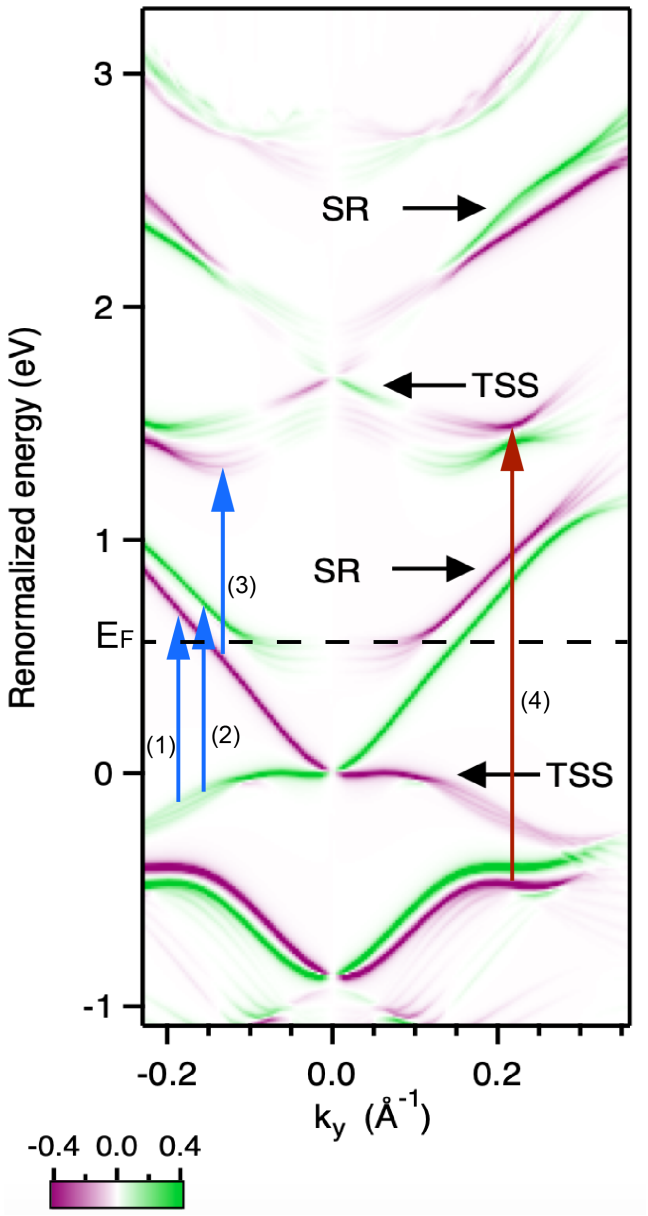

Figure 5.15: Possible excitation paths by 1550 nm (blue arrows) and 635 nm (red arrow) wavelength illuminations. Original bands calculation figure is from ref.[193], color function infers the in-plan spin polarization. SR stands for surface resonance states. We think that the excitation paths at 1550 nm wavelength are more related with TSSs, whereas that at 635 nm wavelength is not related with TSSs, probably. This can explain why AOI dependence of the HDP at 1550 nm wavelength illumination changes between 4 QL and 7 QL samples.

Besides, PDE current originates from the transfer of the photon momentum to photoexcited carriers. As discussed in the ref.[194], the photocurrent due

to the photo drag effect is proportional to the absorption coefficient α. The absorption coefficient at 635 nm wavelength is around 20 times larger than that at 1550 nm wavelength as shown in Tab. 5.1. It is normal that the CPDE contribution to the HDP is more profound at 635 nm wavelength illumination than at 1550 nm wavelength illumination.

More importantly, AOI dependence of HDP at 1550 nm wavelength illumination shows a significant change between 4 QL and 7 QL samples, as in Fig. 5.14. As we mentioned earlier, the fully developed TSSs of Bi_2Se_3 appear only above the critical thickness of 6 QL. Therefore, it is straightforward to believe that HDP at 1550 nm wavelength illumination is related with TSSs of Bi_2Se_3. As for the reason why HDP at 1550 nm wavelength illumination exists even below 6 QL, Fig. 4.4 from ref.[154] shows that though TSSs are not fully developed, the predecessor, i.e. Rashba states, also are spin-momentum locking states which are able to host a HDP by CPGE.

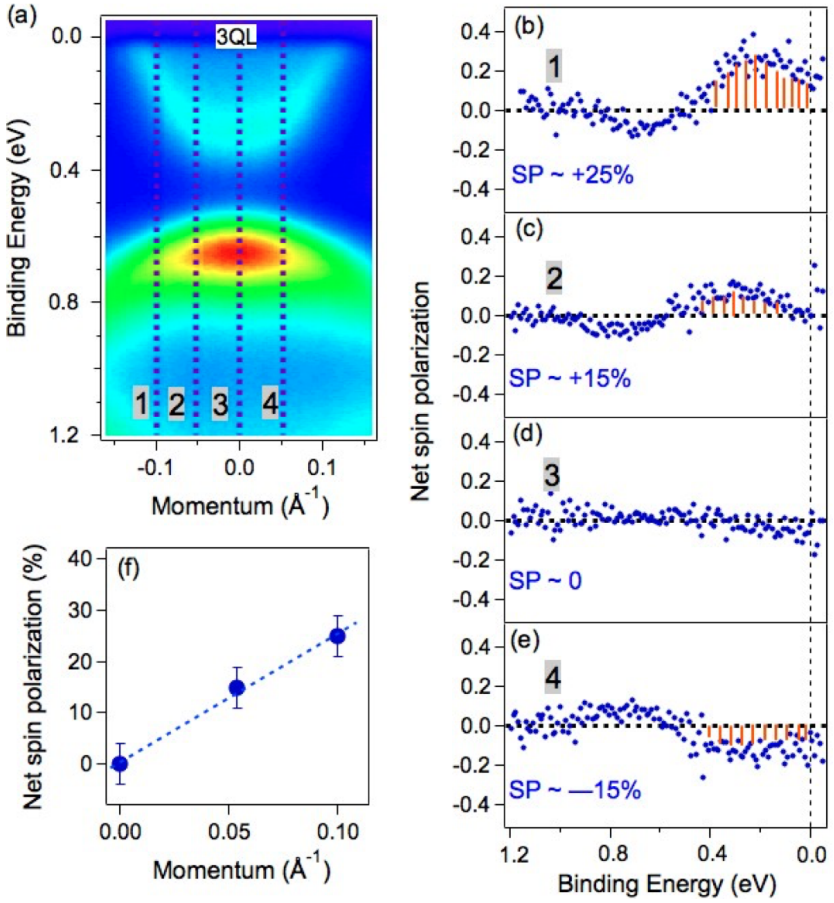

Figure 5.16: SRARPES shows that the predecessor is still spin polarized with in-plane spin polarization. Position far from the Γ point shows higher spin polarization. Figures are from ref.[195]

Second, as shown in Tab.5.1, the penetration depth of the Bi_2Se_3 at 1550

nm wavelength is around 288 nm, so it is inevitably for both top and bottom TSSs contribute to the HDP. However, only the top TSSs will dominate the HDP at 635 nm wavelength illumination when above ∼14 nm thick. The spin-momentum locking of the top and bottom TSSs is opposite (same spin coupled with the opposite momentum), which means HDP due to CPGE would flow in opposite directions for the top and bottom surfaces even under the same circularly polarized light illumination. If the two TSSs contribute equally, the HDP due to CPGE should be zero.

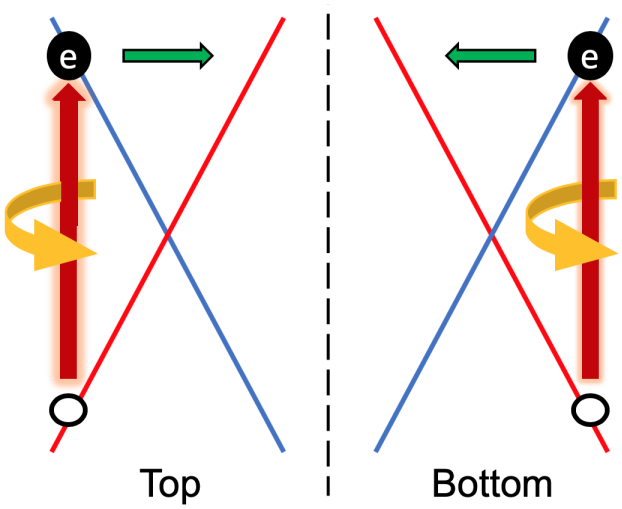

Figure 5.17: Illustration of illuminating top and bottom TSSs with the same circularly polarized light. Due to the opposite spin-momentum locking, same spin excitation will cause opposite flows of HDP.

As it is demonstrated in ref.[14], by comparing HDP between the front and back illuminations, one can conclude that one of the TSSs dominated the HDP. Moreover, as shown in ref.[110], by comparing the front and back illumination with different film thicknesses, one can clarify which TSSs is the main player of the HDP. Due to our apparatus limitation, we can only measure HDP under the front illumination. From Tab.5.1 we can learn that the penetration depth in Bi_2Se_3 at 1550 nm wavelength is roughly 288 nm thick, and that at 635 nm wavelength is just around 14 nm. Therefore, as we change the thickness of the film, the HDP of CPGE (antisymmetric part, presumably) at 1550 nm wavelength illumination should not change after the TSSs emergence after 6 QL, since the penetration depth is too long. Ideally, the total HDP due to CPGE should vanish if both top and bottom TSSs are equally illuminated. However, the influence from substrate, like carrier doping or roughness induced bad morphology, could lead to a inequivalent top and bottom TSSs and result in a nonzero output as we observed by 1550 nm wavelength illumination. As for the HDP of CPGE at 635 nm wavelength illumination, it should become smaller with increasing the film thickness and finally change the flow direction of HDP at around 14 nm, if the dominated TSSs is the bottom one. However, the experimental results differ, which means either the TSSs at top surfaces contribute greatly or there is no HDP of CPGE under 635 nm wavelength illumination.

Another interesting phenomenon is observed in the AOI dependence of 1550 nm during the thickness variation. We can see that the antisymmetric part HDP of the AOI dependence changes its sign from 4 QL to 7 QL sample. There are three possible explanations for this observation. First, this change of sign is due to the competence between CPGE and $CPDE_2$. As we mentioned in Fig. 5.6, the antisymmetric AOI dependence of HDP comes from CPGE or $CPDE_2$, so the thickness increasing would enhance the CPDE contribution since CPDE has bulk contribution but CPGE does not. If the CPGE and $CPDE_2$ are opposite in sign, when the thickness changes, the AOI dependence of HDP would change accordingly. However, we didn't observe a further increase of the antisymmetric AOI dependence of HDP in the 10 QL sample compared with the 7 QL as in Fig. 5.14, which means this explanation could be wrong. Second possibility is that the antisymmetric part in AOI dependence of HDP mainly originated from CPGE and the dominating TSSs change from the top surface to the bottom surface (or otherwise). As we discussed earlier, top and bottom TSSs show opposite spin-momentum locking feature, thus if the dominating TSSs changed, then the CPGE will reverse its direction accordingly. However, on the one hand the penetration depth at 1550 nm wavelength is always long enough to cover both TSSs; on the other during our growth procedure we did not observe a clear difference from the RHEED which means the quality of top and bottom surface does not change drastically to cause dominating TSSs change. So, this hypothesis is also not true. Third and the most plausible explanation is that this sign change is natural when the origin of CPGE is TSSs, which changes from Rashba surface states (TSSs predecessor) to the helical Dirac cone. As we introduced in Chp. 2 Sec. Spin and Charge interplay, spin-to-charge conversion in a Rashba like surface states is determined by the spin-momentum locking of the outer subband while the inner subband generates an opposite current that weakens the total current output. During the TSSs evolution, as shown in Fig. 4.4, the outer subband of the predecessor Rashba states gradually disappear and left the inner subband to form the TSSs. If we injecting a certain spin into this process, it is natural that the output current will reverse its direction when the TSSs come into being, as illustrated in Fig. 5.18. Therefore, this observation further supports that the antisymmetric part of the AOI dependence of the HDP comes from CPGE, and the CPGE is closely related with the TSSs of Bi_2Se_3 under 1550 nm wavelength illumination.

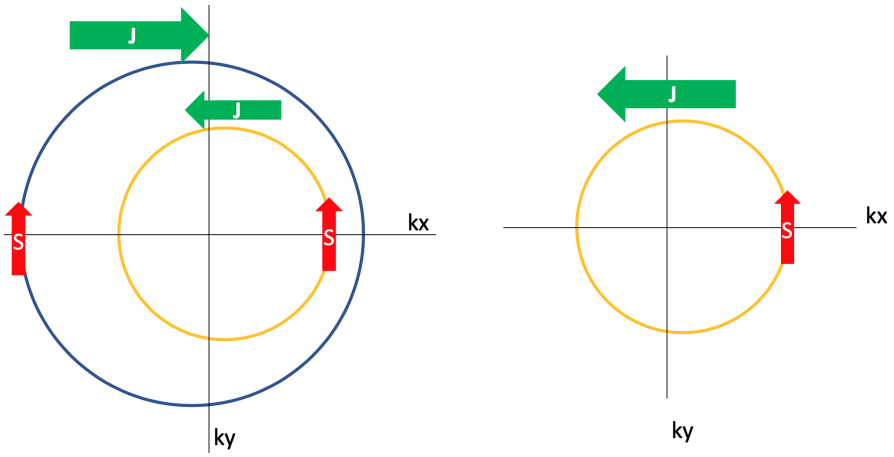

Figure 5.18: Spin-to-charge conversion in Rashba surface states and TSSs. With the same spin injected (red arrow), (a) Rashba surface states yield two opposite flowing currents in two subbands, and the total current direction is determined by the outer subband. (b) TSSs yield a current that flows the same direction as the inner Rashba band but opposite to the total current of Rashba surface states. This current direction change will happen during the evolution of TSSs.

5.3.4 HDP at normal incidence

While measuring the HDP of Bi_2Se_3, an unexpected phenomenon was observed during the measurement, i.e. horizontal-position dependent HDP. As shown in Fig. 5.19, HDP varies across the sample when shifting the illumination center from the left edge of the sample to the right edge of the sample. In addition, this position dependent component does not reverse when changing the incident angle of the light.

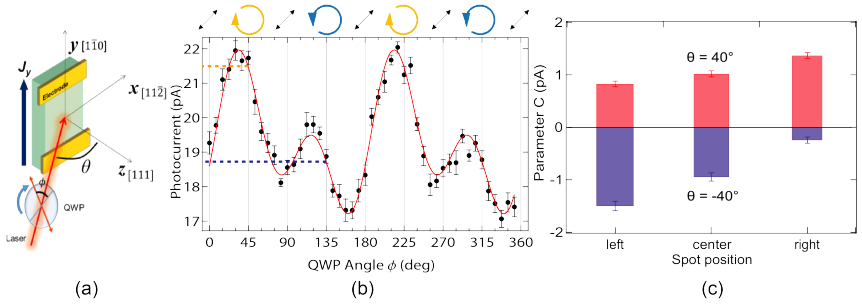

Figure 5.19: (a) Schematic geometry of measurement. (b) Polarization dependent photocurrent at left edge under 40° incidence. (c) HDP at different positions and incident angles.

As we discussed in Eqn. 2.78 at Sec. 1.5, circularly polarized light raising or lowering spin states of electrons along the quantized axis which is the incident direction. HDP of CPGE reverses the direction when the incident angle of

light changes to opposite with respect to surface normal, because the in-plane angular momentum component of photon reversed. Simultaneously, the out-of-plane component remains unchanged when using opposite incident angles. Naturally we can relate this effect with the out-of-plane component of electron spin. To confirm this hypothesis, we measured the HDP under normal incidence where CPGE is prohibited as shown in Eqn. 5.13.

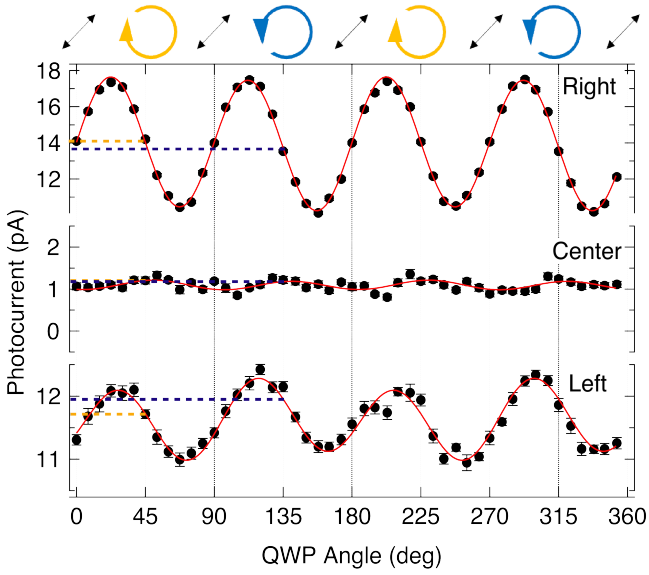

(a)

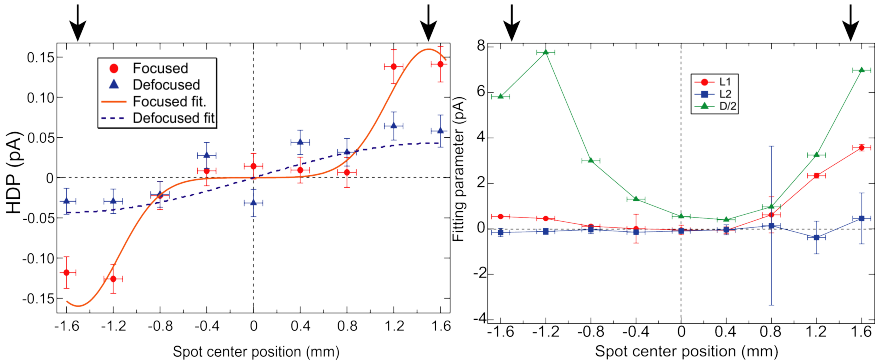

(b)

Figure 5.20: (a) Polarization dependent photocurrent at the left edge, center and right edge of a 13 QL thick Bi_2Se_3 thin film under normal incidence by a 1550 nm wavelength laser. HDP is absent at the center of the film but appears at two edges of the film and opposite in sign to each other. (b) Position dependence of fitting parameters by Eqn. 5.19. Black arrows denote the position of sample edges. Parameter C which indicates by HDP shows a clear antisymmetric dependence, with respect to the sample center, in which the HDP signal reaches its extrema at edges but almost zero at center position, in both focused (diameter 1 mm) and unfocused (diameter 2 mm) cases. Other parameters which corresponds to LP photocurrent and polarization independent photocurrent show symmetric behaviors.

As one can see in Fig. 5.20, HDP does not present when illuminating at the center of the sample but appears at the edges with opposite sign to each other. Position dependence of this HDP clearly shows an antisymmetric distribution with respect to the sample center, and the maximum of the HDP strongly

depends on the spot profile; a focused spot generates a larger HDP at the edge. Other photocurrent components as in Fig. 5.20(b) have some position dependence, but these components are symmetric with the respect to the sample center. To further understand the phenomenon, laser power dependence of HDP was measured, together with a control experiment on Si(111)-7 × 7 substrate by a 635 nm wavelength laser. A linear power dependence is obtained which means this HDP is a second-order optical response that originated from single photon absorption. The control experiment on Si(111)-7 × 7 substrate shows no HDP at all.

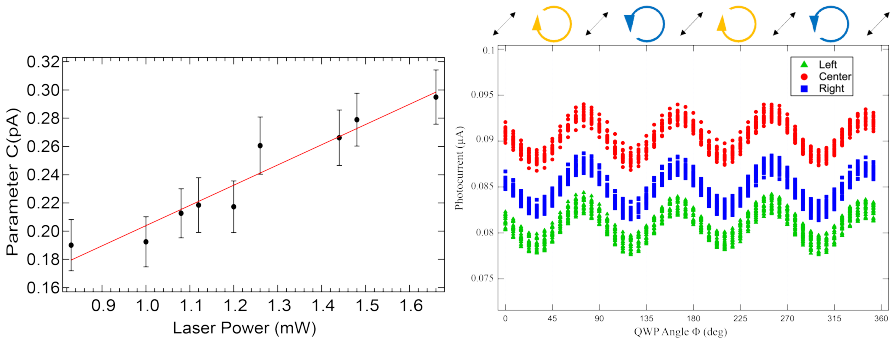

(a) (b)

Figure 5.21: (a) Laser power dependence of the HDP at the edge of the sample. (b) Control experiment on Si(111)-7 × 7 substrate by a 635 nm wavelength laser. Light at 1550 nm wavelength is transparent for silicon because the photon energy (∼ 0.8 eV) is smaller than the band gap of silicon, so no photocurrent should be observed.

One may consider that the CPGE at the edge might be possible since the symmetry of the edge is not exactly the same as the bulk sample. Indeed, similar as the surface symmetry which differs from the bulk symmetry by breaking the inversion symmetry, the edge has its own symmetry by breaking the 3-fold rotational symmetry that only the mirror reflection along the x axis remains. In this case, we can calculate the pseudo tensor for CPGE by Eqn. 5.5. We have the pseudo tensor

$$\gamma_{\text{edge}} = \begin{pmatrix} 0 & \gamma_{xy} & 0 \\ \gamma_{yx} & 0 & \gamma_{yz} \\ 0 & \gamma_{zy} & 0 \end{pmatrix}. \tag{5.25}$$

Following the Eqn. 2.88 we will have the HDP in y direction

$$j_y = \gamma_{yx} P_{circ} E_0^2 e_x + \gamma_{yz} P_{circ} E_0^2 e_z \tag{5.26}$$

At normal incidence, the first term will disappear ($e_x = 0$) but the second term survives ($e_z \neq 0$). However, changing illumination position would not affect the propagation direction e_z of the light, so the HDP should be the same for both left and right edges if it was CPGE. Clearly, the experimental results differ meaning that observed HDP is not due to CPGE.

Another scenario might enable the edge HDP is that the CPGE at the side surface of a thin film. If it presents, this side surface CPGE indeed would reverse the direction when illuminating the opposite edge. But the magnitude of this CPGE should be very small if we consider the side area of a thin film. As shown in Fig. 5.19, HDP at the center of the film should be originated from CPGE totally, so the additional HDP at the edge is ±0.2 pA. If we assume the value of CPGE is proportional to the illumination area, then the size of side surface should be $\frac{0.2}{1} \times 1.2\text{mm} = 0.24$ mm high. However, for a 13 QL thick thin film, the height of the film is only 13 nm. That is 10^5 times different, thus the side surface CPGE cannot be the explanation for the observed edge HDP.

The possible origin of the this HDP is the photoinduced ISHE. When shining circularly polarized light at the sample, spin polarized carriers would be photoexcited. Due to the concentration distribution of these carriers, a diffusion current would be generated.

$$J_d = D \cdot \nabla N, \tag{5.27}$$

where D is the diffusion constant and N is the concentration of the photoexcited carriers. Under a certain circular polarization of the light, the spin of electrons and holes would gain $+\hbar$ or $-\hbar$ with respect to the helicity of the light. As a result, electrons and holes with the same spin diffuse outwards radially from the spot center. In this case, J_d represents a pure spin current. Usually, the diffusion coefficient of electrons is larger than that of holes so electrons would diffuse faster than holes and causes the ambipolar diffusion, which has already been observed on Bi_2Se_3 [196]. The ambipolar diffusion is the diffusion speed difference of electrons and holes creates an electrical filed which slows down the faster carriers and speeds up the slower carriers. As a result, two types of carriers reach the same diffusion speed and a net spin current is created.

As we mentioned earlier, normal incidence of circularly polarized light will excite the out-of-plane spin component, i.e. S_z. In a strong SOC material ISHE is expected to happen when we have a in-plane spin current with spin polarized in S_z.

$$J_{ISHE} = \theta_k J_d \times S_z. \tag{5.28}$$

Here, θ_k is the spin Hall angle of Bi_2Se_3, which marks the efficiency of the conversion between the spin current J_d and the charge current J_{ISHE}. In our specific case here, θ_k does not contain other spin-to-charge conversion phenomena, like IREE, since IREE cannot produce observable current in this case because the spin component here is the out-of-plane spin S_z. When the laser spot shines at the center of the sample, a radial diffusion of spin current will occur and the ISHE gives a swirling charge current. Due to the close loop of this ISHE current, it cannot be observed by the two electrodes across the sample. However, if the diffusing spin current is not centrosymmetric, e.g. shining laser at the interface of two adjacent materials, the consequently ISHE current would be detectable by electrodes across the sample. Simplest case would be illuminating the edge of the sample.

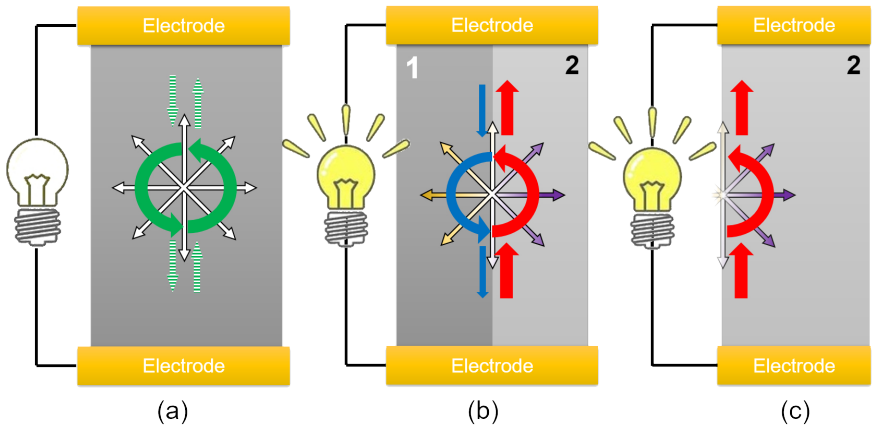

Figure 5.22: (a) When the circularly polarized light irradiates the center of the sample surface, the circulating charge current (green solid arrows) appears, which is converted from the radial diffusing spin current (white solid arrows) by the ISHE. However, no outcome can be detected by the electrodes at both ends of the sample. The dashed green arrows are the inflow and outflow of the closed circulating electric current, canceling each other, resulting in no net flow along the sample. (b) When the circularly polarized light irradiates an interface between different materials, 1 and 2, the inflow and outflow currents are not equivalent, resulting in a net current flowing along the longitudinal direction. (c) As one of the simplest situations of (b), when the material 1 is vacuum, the net current is expected to be the maximum.

Here a schematic figure shows hypothetical experiments that the ISHE charge current could be observed. When the diffusing spin current does not balance anymore, the resultant ISHE current can be detected by those electrodes. To verify the hypothesis, here we analyze the results of the diffusion spin current which is created by optical illumination. First, dividing the sample in to a 14×34 mesh, then spin is injected at a fixed position with a profile of

$$I_{S_z} = \begin{cases} 1, & \text{selected mesh} \\ 0, & \text{others} \end{cases} \tag{5.29}$$

Following the equation (10)-(13) from ref.[197]

$$\boldsymbol{j} = \boldsymbol{j}_o + \boldsymbol{j}_{av} + \boldsymbol{j}_{ss} + \boldsymbol{j}_{sj}, \tag{5.30}$$

$$\boldsymbol{j}_o = -\frac{\sigma}{2e}(\nabla\mu_c + \nabla(\boldsymbol{\mu}_s\hat{\sigma})), \tag{5.31}$$

$$\boldsymbol{j}_{av} = \sigma\frac{\alpha\hbar}{6mDe}(\nabla \times \boldsymbol{\mu}_s + \hat{\sigma} \times \nabla\mu_c), \tag{5.32}$$

$$\boldsymbol{j}_{sj} = \sigma\frac{\alpha}{3e}(\hat{\sigma}\nabla)\boldsymbol{\mu}_s, \tag{5.33}$$

$$\boldsymbol{j}_{ss} = -\sigma\frac{\alpha}{3e}\hat{\sigma}(\nabla\boldsymbol{\mu}_s). \tag{5.34}$$

Here, $\boldsymbol{j}_o$ is the ordinary current without SOC, $\boldsymbol{j}_{av}$ is the current due to the anomalous velocity operator, $\boldsymbol{j}_{ss}$ is the current originated from skew scattering, and $\boldsymbol{j}_{sj}$ is the current owing to the side-jump scattering. $\sigma = e^2N_0D$ is the

conductivity, μ_c and $\boldsymbol{\mu}_s$ are the charge and spin distribution, α is the SOC constant, $\hat{\sigma}$ is the electron spin in Pauli matrices, and D is the diffusion constant. Then we can calculate the electric potential distribution at equilibrium.

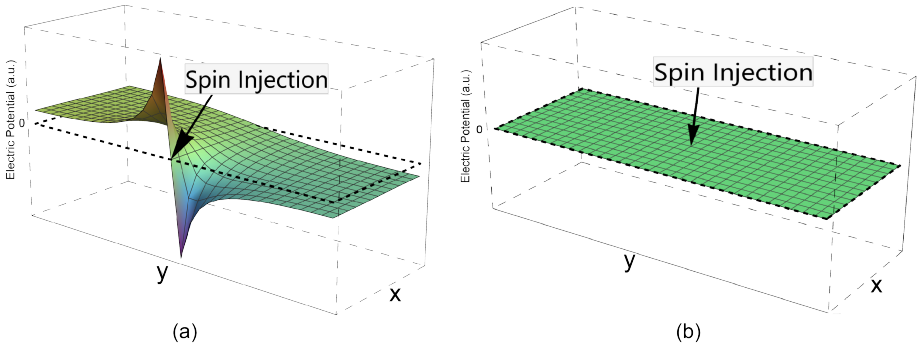

Figure 5.23: Electric potential distribution at equilibrium when injecting spin at the (a) left edge and (b) center of the sample, indicated by the arrow respectively. When S_z spin is injected at the left edge, a dipole-like potential is created around the injection position and a finite potential difference is generated across the whole sample. However, no potential difference created when spin is injected at the center of the sample.

The dipole potential here exactly reveals the charge accumulation by the swirling current generated by ISHE, by which the circulating current path acts like a charge conveyor transferring electrons/holes from one location to another on the same edge and forming an electric dipole. This process goes to the equilibrium when the ISHE current is balanced by the electric field of the dipole. For a Gaussian beam, this conveyor can be seen going along the extrema of the derivative, as shown in Fig. 5.24.

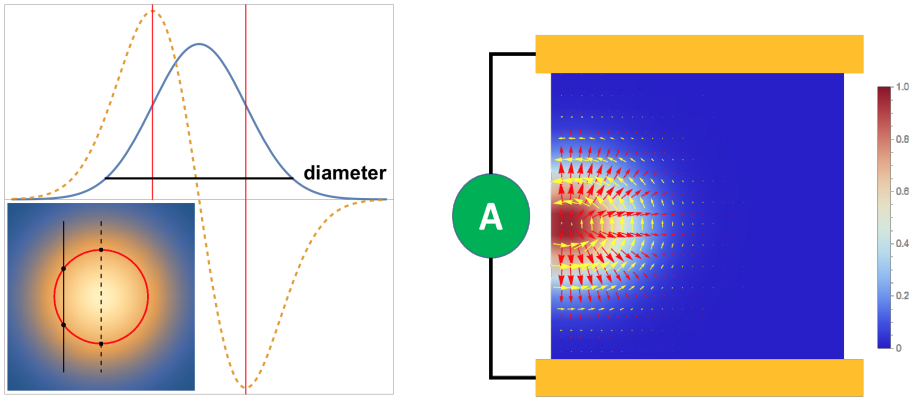

Figure 5.24: (a) A Gaussian function (blue line) and its derivative (dashed yellow line). Black line shows the diameter (4σ) of this Gaussian and two red lines indicate the extrema of it. The inset shows the 2D plot of this Gaussian with the red ring shows the extrema of its derivative. If the edge of the sample (solid and dashed black) cut the spot at different positions, the dipole distance would be different (dipole center indicated by black spots). (b) Color plot shows the intensity of a Gaussian laser beam, red arrow shows the diffusing spin current, yellow arrow indicates the movement of electrons. The size of the arrow suggests the magnitude of the corresponding current.

After the preliminary understanding of this phenomenon by finite element method (FEM) simulation we can start to write down the functions to describe this phenomenon. The irradiance of a z-propagating (surface normal) Gaussian wave can be written as

$$I(r, z_0) = I_0 \exp(\frac{-r^2}{2\sigma^2}), \tag{5.35}$$

where r is the distance between the spot center and a certain position in xy plane and 2σ indicates the radius of the spot. For a laser beam that the spot center located at (x_0, y_0) with AOI= θ degree in xz-plane, the expression is

$$\begin{aligned} I &= I_0 G(x, y, \theta), \\ G(x, y, \theta) &= \frac{\cos\theta}{2\sigma^2\pi} \exp(-\frac{(x-x_0)^2\cos^2\theta + (y-y_0)^2}{2\sigma^2}). \end{aligned} \tag{5.36}$$

And the consequent diffusion current is

$$\boldsymbol{J}_d = D \cdot \nabla N. \tag{5.37}$$

Here the N is the concentration of the photoexcited carriers and D is the ambipolar diffusion constant of the Bi_2Se_3 in one direction. The photoexcited carriers $N(x, y)$ should follow the same distribution as the irradiance of the light which is $G(x, y, \theta)$. $N = A\, G(x, y, \theta)$ where A is a coefficient related with excitation probability.

$$\begin{aligned} J_{dx} &= -AD\frac{(x-x_0)\cos^3\theta}{2\sigma^4\pi} \exp(-\frac{(x-x_0)^2\cos^2\theta + (y-y_0)^2}{2\sigma^2}) \\ J_{dy} &= -AD\frac{(y-y_0)\cos\theta}{2\sigma^4\pi} \exp(-\frac{(x-x_0)^2\cos^2\theta + (y-y_0)^2}{2\sigma^2}) \end{aligned} \tag{5.38}$$

Then the resultant ISHE current is written as

$$J_{\mathrm{ISHE}} = \theta_k \boldsymbol{J}_d \times \boldsymbol{S}_z, \tag{5.39}$$

where θ_k is the spin Hall angle and $\boldsymbol{S}_z$ is the z-component spin of the photoexcited carriers. The $\boldsymbol{J}_d$ and J_{ISHE} are plotted in Fig. 5.24(b) shown by red arrows and yellow arrows respectively.

Finally, we can write the Poisson equations when the whole system goes to equilibrium. The potential $\varphi(x, y)$ follows

$$\nabla \cdot (\sigma_{1 \text{ or } 2} \nabla \varphi(x, y)) = 0, \tag{5.40}$$

$$\sigma_2 \boldsymbol{n} \cdot \nabla \varphi(x, y)|_{x=-w} = -J_x^{\mathrm{ISHE}}(-w, y), \tag{5.41}$$

$$\varphi(x, 0) = 0. \tag{5.42}$$

Here, $\boldsymbol{n}$ is the unite vector perpendicular to the sample edge, $\sigma_{1,2}$ is the conductivity of electrodes and the sample respectively, and w is the half width of the sample. Solving these equations would give a similar result as the FEM shown in Fig. 5.24(a). Furthermore, we can estimate the potential difference between the two electrodes with these equations. The tungsten electrodes have the conductivity of 1.89×10^7 S/m [iv], and the conductivity of Bi_2Se_3 is 4000 S/m [198]. 1 mW 1550 nm laser would inject 1×10^{-3} J/0.8 eV $= 7.8 \times 10^{15}$ photons per second, and only $7.8 \times 10^{15} \times \alpha \times 13$ nm $= 3.751 \times 10^{14}$ photons per second would be absorbed by a 13 QL Bi_2Se_3 (α is the absorption coefficient of Bi_2Se_3 at 1550 nm wavelength). Here we assume every signal photon would create a 100% spin polarized electron-hole pairs (this will be the upper limit). The ambipolar diffusion coefficient is 500 cm^2/s [196], so the one directional diffusion coefficient should be $\sqrt{0.005} = 0.07$ m/s. The spin Hall angle of Bi_2Se_3 is $0.0093e$ [199], e is the elementary charge when the assumed $\boldsymbol{S}_z$ is -1. With a 3 mm wide 8 mm long sample and a 0.8 mm diameter wide laser spot shining at the left edge of the sample, the voltage difference between two electrodes is -1.31×10^{-11} V when grounding the lower electrode. It can be seen that this numerical simulation is consistent with the experimental results and suggests that with spin injection, ISHE can create a finite potential difference across the sample. The exact value of the simulation results might be different from the real experiment since the influence of the substrate is totally not considered here, besides . Though the magnitude is very small, this is still a measurable value of voltage for lock-in amplifier. During the calculation it is noticed that a smaller laser spot, a smaller width of the sample, a lower conductivity of the sample or a larger spin Hall angle would give rises to a larger voltage difference between two electrodes.

[iv] https://en.wikipedia.org/wiki/Tungsten

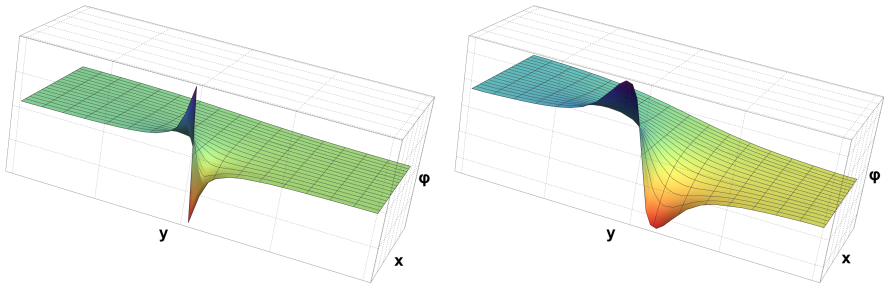

(a) (b)

Figure 5.25: Numerical solution of the Poisson equations for (a) $\sigma = 0.1$ (b) $\sigma = 0.4$. The potential difference between two ends for (a) is roughly 4 times larger than (b), though it looks opposite because the scale of the figure is normalized by the dipole peak; the dipole peak of the larger spot (b) is much lower than the sharp one (a).

It is difficult to get the analytical solution for the Poisson equations above, so here we use an approximation to get the function for the potential measured by those electrodes. As we mentioned earlier, ISHE cause a dipole like potential, so we try to use the dipole potential to express the result.

$$\varphi(r) = \frac{kp\cos\beta}{r^2}. \tag{5.43}$$

Here k is the Coulomb's constant, r is the distance from the dipole center, $\boldsymbol{p} = q\boldsymbol{d}$ is the dipole moment where d is the vector pointing from the negative charge center to positive charge center, and β is the angle between $\boldsymbol{r}$ and $\boldsymbol{p}$. Then the dipole at the edge is

$$\boldsymbol{p} = J^{\mathrm{ISHE}}_{x=\pm w} y dy. \tag{5.44}$$

The voltage difference between the electrodes will be

$$V = 2k\int_0^l \frac{J^{\mathrm{ISHE}}_{x=w} y dy\cos\beta}{r^2} + 2k\int_0^l \frac{J^{\mathrm{ISHE}}_{x=-w} y dy\cos\beta}{r^2} \tag{5.45}$$

Here, l is the half length of the sample in y direction. The reason why we need to integrate the dipole at both edges is in case that the laser spot is big enough to cover both edges. When the spot is small, only half of the above equation is enough. The solution of the integration is

$$V = kAD\frac{\exp -\frac{2w^2+2x_0^2+l^2}{2\sigma^2}(\exp\frac{(w-x_0)^2}{2\sigma^2} - \exp\frac{(w+x_0)^2}{2\sigma^2})(2l - \sigma\exp\frac{l^2}{2\sigma^2}\sqrt{2\pi}\mathrm{Erf}\frac{l}{\sqrt{2}\sigma})}{4\sigma^2\pi l^2} \tag{5.46}$$

Divided by the sample resistance, we can have the current that we measured. Actually, Fig. 5.20(b) is fitted by this function.

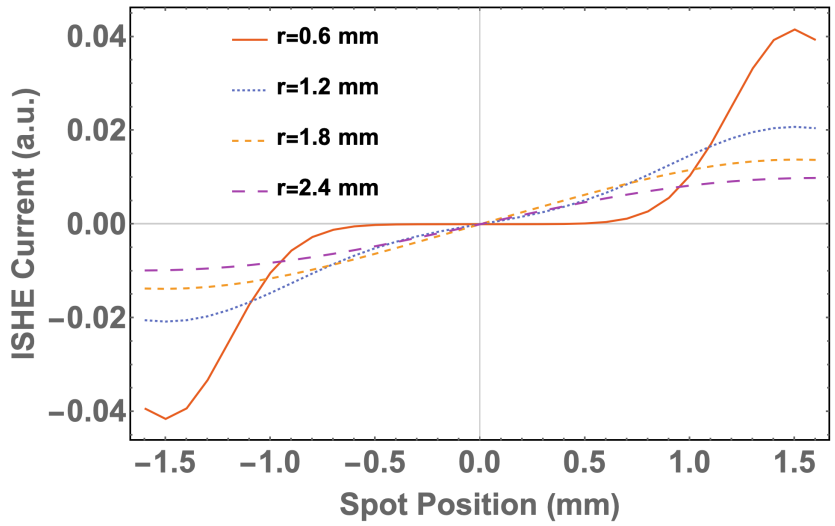

Figure 5.26: ISHE current as a function of laser spot position across the sample, calculated from Eqn. 5.46, with different spot size of laser beam. r is the radius of the Gaussian beam spot (r= 2σ).

The key factor for the ISHE to occur in such geometry is the out-of-plane spin. As we mentioned earlier, we suspect the hexagonal warped TSSs or Rashba states would be the source of the out-of-plane spin. To verify the hypothesis, a Bi_2Se_3 film thickness dependence of the HDP at normal incidence is measured. As we known from the previous calculation, higher power and smaller spot is good for a larger HDP. Thus, in the following measurement, 1.36 mW with 0.6 mm diameter spot is applied.

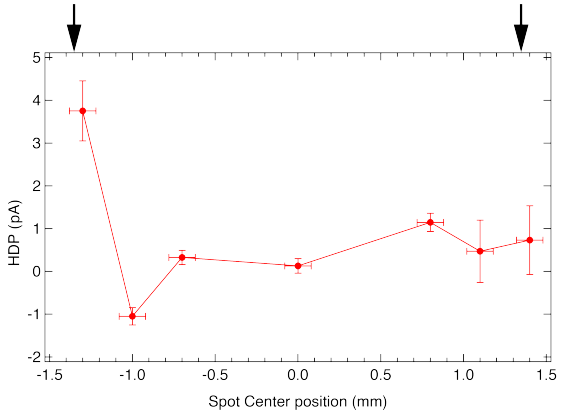

(a)

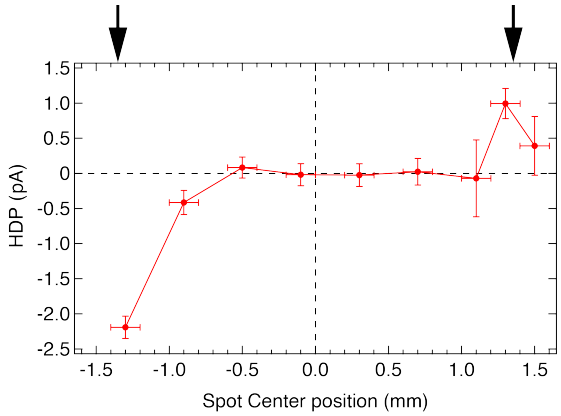

(b)

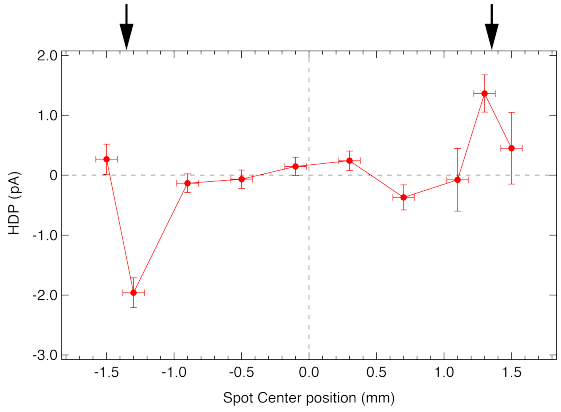

(c)

Figure 5.27: Bi_2Se_3 film thickness dependence of HDP at normal incidence by a 1550 nm wavelength laser. (a) 4 QL (b) 7 QL and (c) 10 QL. Clear ISHE like position dependence is observed on 7 QL and 10 QL samples, while 4 QL sample does not show a clear ISHE like position dependence.

We measured thickness dependence on the same samples as used in previous section, in which thicker samples were made by successively deposition on thinner one. As shown in Fig. 5.27, a clear position dependence is observed in thicker samples but not in the 4 QL one. Besides, we also checked the HDP at normal incidence by 635 nm laser in the 8 QL sample, no position dependence is observed.

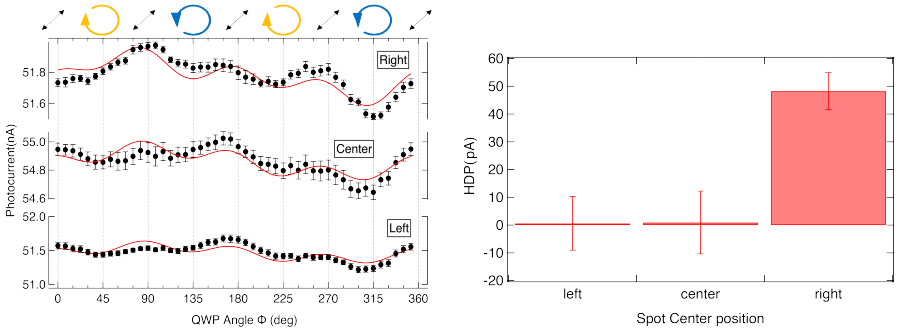

(a) (b)

Figure 5.28: Position dependent HDP measured by a 635 nm wavelength laser at normal incidence. (a) Photocurrent at normal incidence. To fit the data, additional term, $a \sin \phi$, needed to add in Eqn. 5.19. This 360° periodicity term comes from the intensity change due to the full rotation of the QWP. (b) From the fitting, HDP term shows no change of the sign when illuminating the opposite edge. The large value of HDP at the right edge probably due to a defect at that position.

5.3.5 Discussion

Previously, position dependent HDP was also observed by others in similar materials. Seifert *et al* observed this position dependent HDP on Bi_2Te_2Se (shown in their supplemental material). However they conclude the mechanism for this HDP with CPGE from the side surfaces [200]. As we estimated in the previous section by the data we have in Fig. 5.19, the side surface CPGE will not contribute that much HDP. So, this side surface CPGE explanation may not be correct. In another paper, Schumann *et al* report a spin Nernst photocurrent observed in $(Bi_{0.57}Sb_{0.43})_2Te_3$, with oblique incidence HDP shows opposite sign at opposite edges. Schumann *et al* suggest that the thermal current induced by laser illumination create a spin accumulation at the edge of the sample by spin Nernst effect and such spin accumulation modulate the CPGE [201]. It could be possible if the measurement is under oblique incidence since the in-plane spin is the key to explain their results. However, we can observe this position dependence even at normal incidence which no in-plane spin could be excited. In our opinion, those observation probably are not the CPGE but the ISHE due to asymmetric illumination as our results shown.

Other mechanisms are also proposed for the HDP that is generated at normal incidence. Hosur proposed a model that such HDP due to interband transition is controlled by the Berry curvature of the surface bands [202]. To observe this HDP, two essential requirements are listed, out-of-plane spin components

in TSSs and breaking of the rotational symmetry. Though our experiments fulfilled those two requirements, our results differ. Since both left and right edges break the rotational symmetry, the HDP controlled by Berry curvature should be the same. However, the HDP at opposite edges flow in opposite directions as shown by our results.

Ji *et al* discovered a so-called spatially dispersive circular photogalvanic effect (s-CPGE) in a Weyl semimetal [203]. The mechanism for this s-CPGE is proposed to be the $\boldsymbol{k}$ space distribution of excited electrons is modulated by the optical field gradient, and the dominant term of the s-CPGE requires the material to lack of the inversion symmetry. Their experiments show that the Weyl semimetal ($MoTe_2$) they used to undergo a phase transition (1T' phase to T_d phase by cooling) that breaks the original inversion symmetry, and s-CPGE is observed after this phase transition. It seems that this s-CPGE should be a bulk effect since the surface of the 1T' phase also lack the inversion symmetry but no s-CPGE observed on such phase.

Despite these claimed different mechanisms, one thing in common is that all of them agree that TSSs should be the origin of the HDP they observed at normal incidence. Indeed, as shown in Fig. 5.15, the possible excitation paths of 1550 nm wavelength are all related with TSSs, and the initial or finial states are at the high energy position of the Dirac cone. As we introduced in the background chapter, out-of-plane spin component due to hexagonal warping is more profound when it is far from the Dirac point. In our experiments, we show that this HDP does not present at the predecessor of the TSSs (4 QL sample). This is consistent with previous SRARPES measurement on 3 QL Bi_2Se_3 where negligible out-of-plane spin polarization is observed [195].

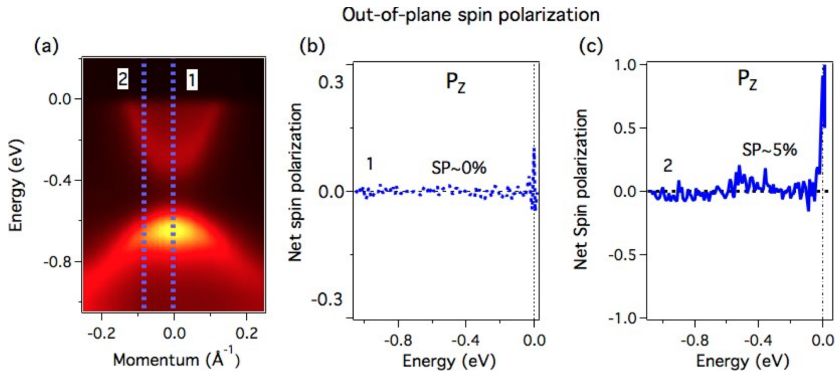

Figure 5.29: SRARPES of a 3 QL Bi_2Se_3, from ref.[195]. Out-of-plane polarization is negligible. This is totally different from a well-developed TSSs where out-of-plane spin polarization is clearly observed [161].

The thickness dependence further back the hypothesis that 1550 nm wavelength excitation path is related with TSSs as previous discussed in Fig. 5.15. When illuminating the predecessor of TSSs, no position dependent HDP is observed whereas a clear position dependent HDP is observed at 7 and 10 QL sample.

Except for the ISHE mechanism we mentioned in the previous section, spin-momentum locking of the out-of-plane spin could also result in HDP at nor-

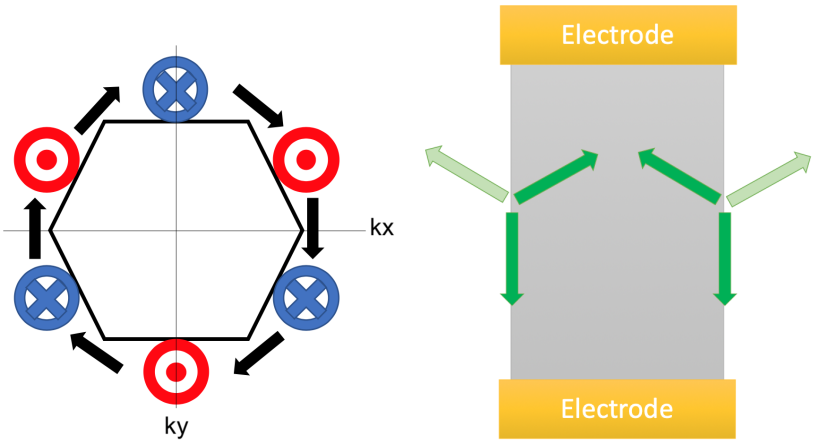

(a) (b)

Figure 5.30: (a) Illustration of the hexagonal warping at the Fermi surface, arrows indicate the local spin orientation. Out-of-plane spin distributed symmetrically in k-space, which means that no net current will be generated by the spin-momentum locking if only populating certain out-of-plane spin. (b) The edge will breaks the threefold rotational symmetry but the left and the right edge will have the same outcome. Green arrows are the currents due to the spin-momentum locking by injected out-of-plane spin, shallow green color indicates the suppressed currents due to the presentation of an edge.

mal incidence. However, this HDP cannot be solely originated from the spin-momentum locking at the hexagonal warping part of the TSSs. Indeed, the out-of-plane spin in TSSs is also locked to a certain momentum and the threefold symmetry of the out-of-plane spin, as shown in Fig. 5.30(a), will make sure no net current be generated under normal incidence of the circularly polarized light. If using the edge to break the threefold symmetry, a current could be obtained, but the same result should be obtained at the opposite edge due to the symmetry, as shown in Fig. 5.30(b). It is clear that our observation shows opposite direction of the current at the opposite edge. The possible way for this spin-momentum locking feature to take part in this position dependent HDP is by acting the same role as the diffusion current that we mentioned in the ISHE mechanism, and the following ISHE will convert this spin-polarized current into the swirling current. Besides, the result by the diffusion current and the the spin-momentum locking current will not cancel each other, since both of them are carriers with the same spin moving outwards from the spot center. One may argue that the spin-momentum locking would forbid the carriers move along directions other than the spin-momentum locked one, so the ISHE cannot act on them. Actually, the ISHE itself is the result of the spin scattering event, as long as it is not the backscattering, other direction scattering is allowed, which means ISHE could act on it.

Moreover, unlike the HDP of CPGE, this HDP due to ISHE does not weaken by the opposite orientated top and bottom TSSs. The only thing different between the top and bottom TSSs is the spin-momentum locking orientation.

As we discussed earlier, this HDP is not the direct result of the spin-momentum locking so there will be no cancellation between the results of the top and bottom TSSs. We can look into the detailed steps of this HDP, first circularly polarized light with normal incidence excites out-of-plane spin, but these spin texture distributed symmetrically in the band structure which means no photocurrent would be generated up to this step. Then, for the diffusion current case, due to the gradient of the laser intensity, spin current rather than charge current is generated, and the direction of the spin current is determined by the gradient of the intensity which is the same for both top and bottom surfaces. For the case of the spin polarized current generated by the spin-momentum locking feature, the direction of the spin polarized current will be different for the top and bottom TSSs, and there could be some compensation but not total cancellation since the TSSs of the top and bottom surfaces are not identical due to the substrate influence and morphology difference during growth. Finally, the edge breaks the swirling charge current and a electric dipole potential is generated at the edge. Therefore, excitation at both top and bottom TSSs will have the same outcome.

5.4 HDP in bismuth thin films

Bi/Si(111)-1 $\times$ 1 film was epitaxially grown on a Si(111) 7 $\times$ 7 reconstructed surface at room temperature. The RHEED pattern is shown in Fig. 5.31.

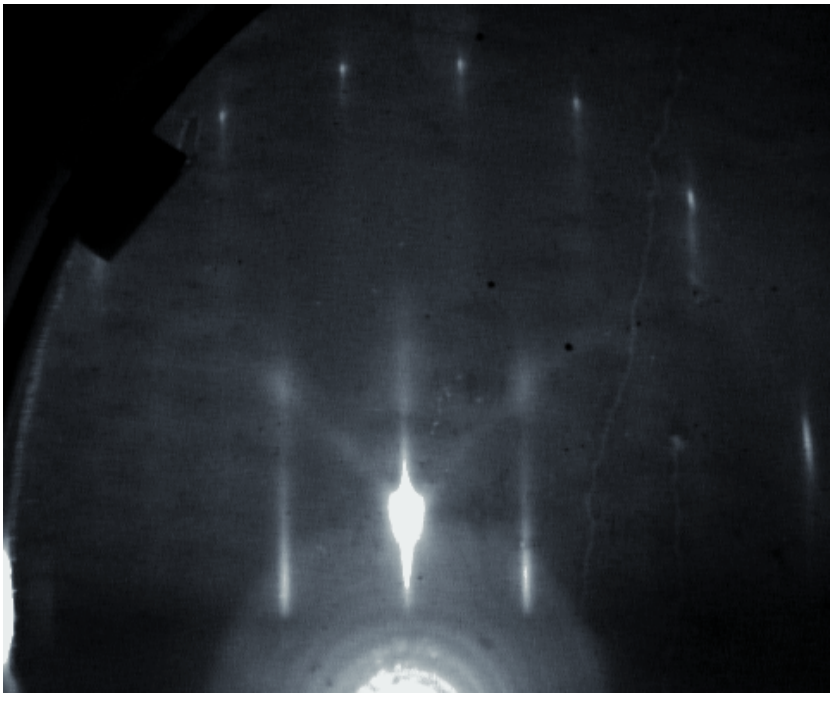

Figure 5.31: RHEED of a 15 BL Bi(111) film grown on Si(111) substrate. Sharp diffraction streaks and Kikuchi lines imply a good quality of this film.

Large photocurrent with a very weak HDP was observed on this Bi(111) film

by 635 nm wavelength illumination. However, photocurrent excited by a 1550 nm wavelength laser is so weak that the total photocurrent is below 3 pA. It is difficult to conclude whether HDP present or not, though fitting suggests HDP presents.

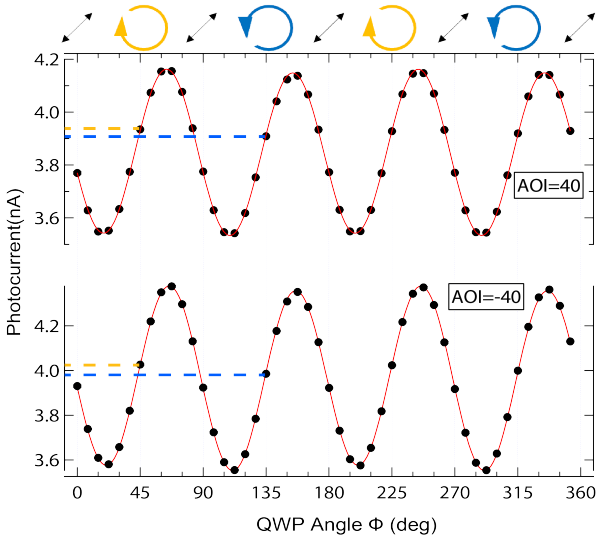

(a)

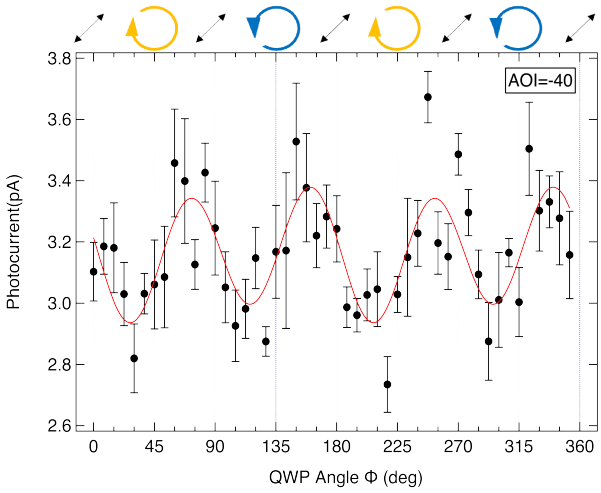

(b)

Figure 5.32: Photocurrent measured by (a) 635 nm wavelength laser and (b) 1550 nm wavelength laser, black dots are the averaged measured datum and red lines are fitting by Eqn. 5.19, error bar shows the statistic standard deviation of the collected datum. Relatively larger photocurrent was observed at 635 nm wavelength illumination than by 1550 nm wavelength. Although absorbance of bismuth calculated in Fig. 5.1 suggests that absorbance at 1550 nm wavelength is slightly larger than that at 635 nm wavelength, the measured photocurrent suggests oppositely. This might be because the refractive index of bismuth we used in calculation is not acquired from a thin film in [175]. Moreover, HDP measured by the 635 nm wavelength laser is of the same sign at both 40° and −40° incidence, i.e. photocurrent excited by RCP is larger than LCP. This suggests that the CPDE is dominating the HDP mechanism.

To further verify the conclusion that the HDP on Bi(111) at 635 nm wavelength illumination is due to CPDE, incident angle dependence of the HDP is measured. As shown in Fig. 5.33, nearly parabolic behavior infers the CPDE mechanism domination. The slight deviation from parabolic is due to term $\sin 2\theta \cdot t_s t_p$ as mentioned in Fig. 5.6.

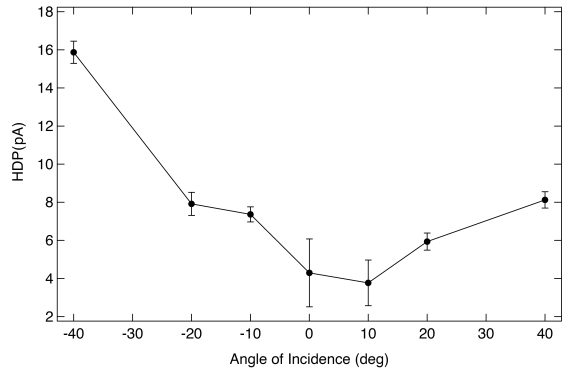

Figure 5.33: Incident angle dependence of HDP. Clearly, the behavior is dominated by CPDE term $\sin^2\theta \cdot t_s t_p$.

Since the HDP suggests that CPDE is the main player, it is safe to say that HDP measured by the 635 nm wavelength laser does not reveal any information about the Rashba spin splitting bands. This probably because of the Rashba factor of spin-splitting surface bands is relatively small, c.f. $\alpha_R = 0.55\text{eV} \cdot \text{Å}$ [204]. Furthermore, two subbands of Rashba states would cancel out the results due to the opposite spin orientation.

HDP at normal incidence is also inspected under 635 nm wavelength illumination. Similar to the fitting of HDP in 8 QL Bi_2Se_3 by the 635 nm wavelength laser, an additional term $a \sin\phi$ is also added into the fitting function of Eqn. 5.19 to fit the datum in Fig. 5.34. The fitting results show a plausible position dependence though the data is not well-fitted, further investigation is needed.

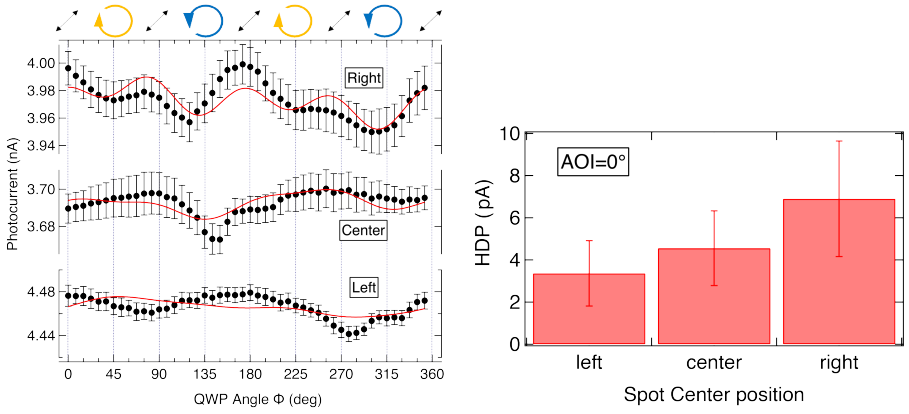

(a) (b)

Figure 5.34: (a) Photocurrent at normal incidence by a 635 nm wavelength laser at the left edge, center and right edge of the sample, fitted by Eqn. 5.19 with an additional term $a \sin \phi$. (b) Fitting parameter C, i.e. HDP component, shows a large none zero value at the center of the sample. HDP at the left and the right edge is larger and smaller than the HDP at the center respectively.

Previously, Zucchetti *et al* found that 3D polycrystalline bismuth on Ge substrate hosts an obvious spin-charge interconversion signal, with the morphology getting better the spin-charge interconversion getting smaller [205]. The thin single-crystalline Bi film shows no spin-charge interconversion which is consistent with our experimental results. Besides, their AOI dependent HDP shows not a total antisymmetric behavior which suggest that CPDE is also observed in their experiments, though Zucchetti *et al* did not consider it.

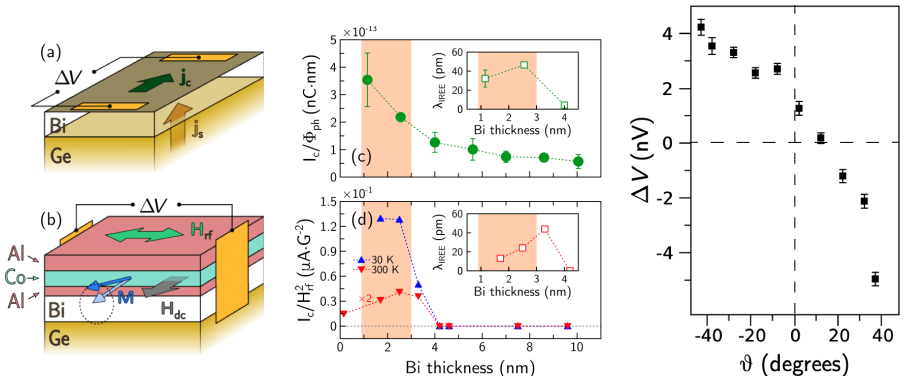

(a) (b)

Figure 5.35: Experimental scheme and results of ref.[205], both optical method and electrical spin injection suggest spin-to-charge conversion decreasing when morphology is getting better. (b) Incident angle dependence of HDP measured by optical method. It is not totally antisymmetric which means CPDE is also included in the HDP measured by Zucchetti *et al*.

5.5 HDP in bismuth antimony telluride thin films

As introduced in Sec. 3.3, by varying the compounds ratio of Sb and Bi in $(Bi, Sb)_2Te_3$, Fermi level can be tunned continuously from the bulk conduction band to the bulk valence band. Three kinds of samples were made to investigate the influence of the Fermi level position on the HDP, namely Sb_2Te_3, $(Bi_{0.45}Sb_{0.55})_2Te_3$ and Bi_2Te_3. Sb_2Te_3 is made on Sb/Si(111)-$\sqrt{3}\times\sqrt{3}$ and the other two are made on Bi/Si(111)-$\sqrt{3}\times\sqrt{3}$ surface structures. By changing the flux ratio of Bi and Sb, $(Bi_xSb_{1-x})_2Te_3$ can be made by MBE. RHEED of those materials are almost the same in the lattice constant and crystalline structures as shown in Fig. 5.36.

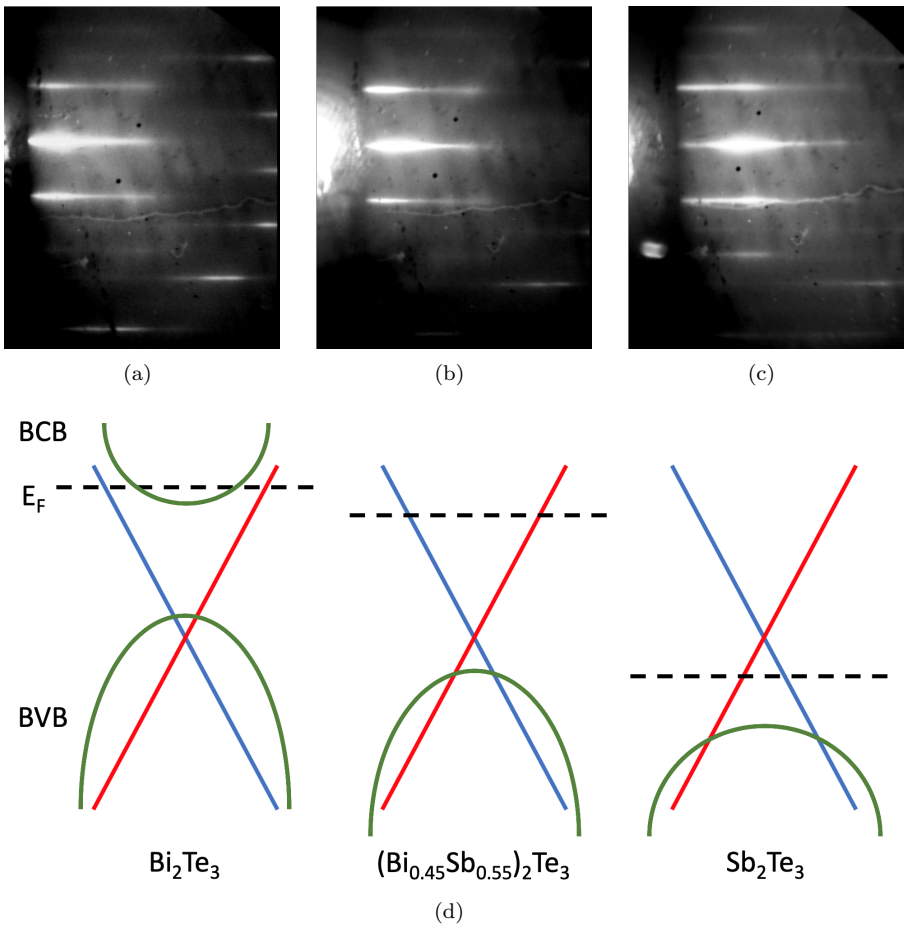

Figure 5.36: RHEED patterns of (a) Sb_2Te_3, (b) $(Bi_{0.45}Sb_{0.55})_2Te_3$ and (c) Bi_2Te_3. Sharp diffraction streaks infer good morphology of those films. (d) Illustration of Fermi level position of these three samples. The Fermi level cut the bulk bands of Sb_2Te_3 in ΓM direction but only the TSSs at ΓK direction as shown in this illustration.

As shown in Fig. 5.37, polarization dependent photocurrent was observed in a 12 QL Sb_2Te_3 film by a 1550 nm wavelength laser. From the incident angle

dependence of the HDP, an antisymmetric dependence with respect to AOI= 0° was observed.

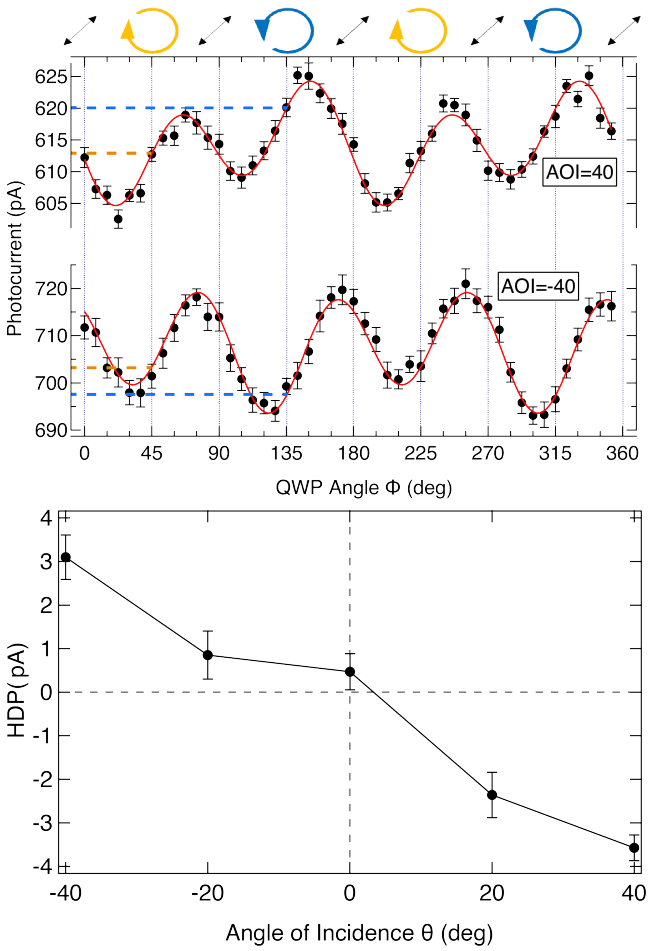

Figure 5.37: Incident angle dependence of HDP in a 12 QL Sb_2Te_3 film by 1550 nm laser. (a) A clear HDP is observed, and the HDP changes sign when reversing the incident angle. (b) An antisymmetric behavior as a function of AOI infers the CPGE mechanism whose AOI dependence is $\sin\theta \cdot t_s t_p$ as shown in Fig. 5.5.

Laser spot position dependence of HDP was also measured in Sb_2Te_3 film. There is a position dependence of HDP, but the HDP at the two edges show the same sign rather than the opposite sign as the ISHE observed in Bi_2Se_3.

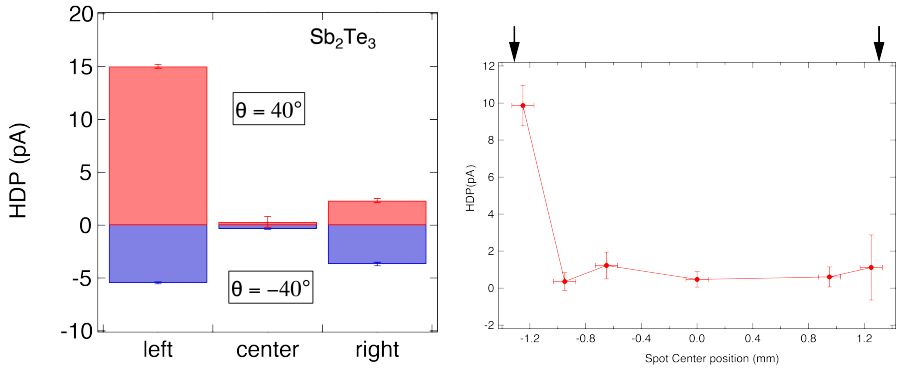

(a) (b)

Figure 5.38: Laser spot position dependence of HDP in Sb_2Te_3. (a) Measured HDP at oblique incidence, the left and right edges show larger HDP than the center of the sample. However, the HDP at the left edge is always larger than that at the right edge even when the incident angle is reversed. This is different from the observation on Bi_2Se_3. (b) Laser spot position dependence of HDP measured at normal incidence. Black arrows indicate positions of the sample's edges. HDP at edges shows large value but with the same sign, which is different from ISHE mechanism observed in Bi_2Se_3.

Then, $(Bi_{0.45}Sb_{0.55})_2Te_3$ was also examined and HDP appeared under both 635 nm and 1550 nm wavelength illumination as shown in Fig. 5.39. However, HDP excited by 635 nm wavelength illumination shows no sign inversion after reversing the incident angle with respect to the surface normal direction. Whereas under 1550 nm wavelength laser excitation, HDP reverses its sign when the incident angle is reversed, though the magnitude is small.

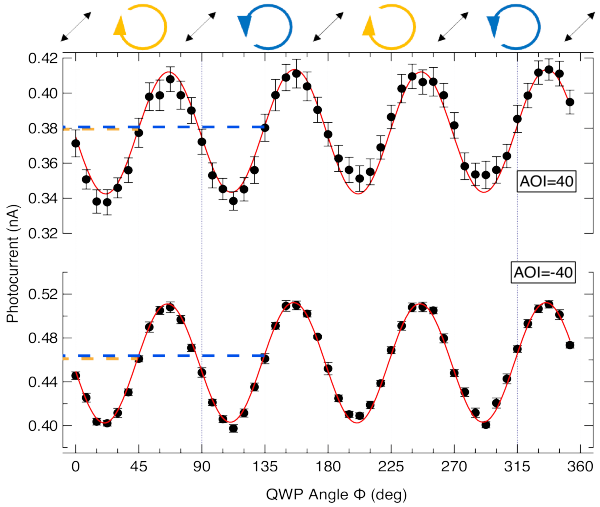

(a)

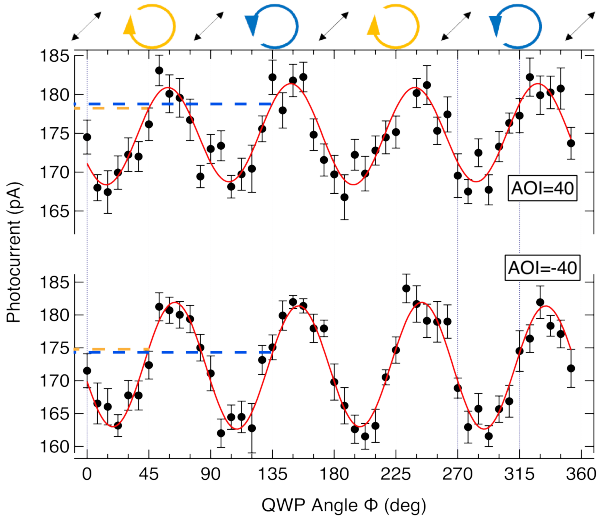

(b)

Figure 5.39: Polarization dependent photocurrent of $(Bi_{0.45}Sb_{0.55})_2Te_3$. Both (a) 635 nm and (b) 1550 nm wavelength illuminations show HDP during measurements. (a) However, HDP does not change sign, i.e. photocurrent excited by RCP is always larger than LCP no matter the incident angle of the light. (b) HDP is reversed when changing the incident angle by the 1550 nm wavelength laser.

When checking the laser spot position dependence of the sample, a clear position dependence was observed, with the sign reversing at the opposite edges.

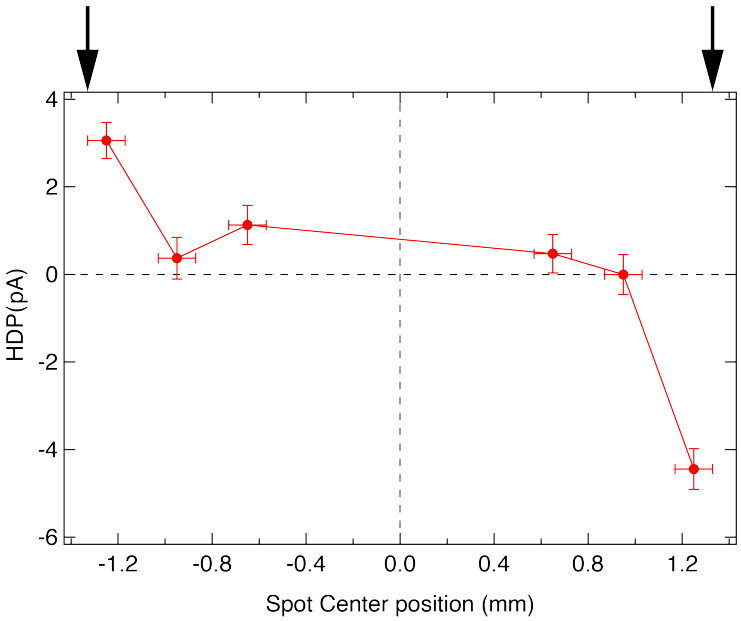

Figure 5.40: Position dependence of HDP in a 12 QL $(Bi_{0.45}Sb_{0.55})_2Te_3$ film. Black arrows denote the edges positions. A clear position dependence with the sign reversing at the opposite edges is observed. This is similar to the observation in Bi_2Se_3 samples, suggesting the ISHE also presents at this sample.

Finally, Bi_2Te_3 was measured. Photocurrent measured by the 1550 nm wavelength laser is around 50 pA, however, polarization dependent part is very small, only around 4 pA as shown in Fig. 5.41(b). Moreover, a vague HDP was observed in Bi_2Te_3 as shown in Fig. 5.41(b). When illuminating by the 635 nm wavelength laser, a clear polarization dependent photocurrent with HDP are observed as shown in Fig. 5.41(a). However, the incident angle dependence suggests the HDP is from CPDE, because the HDP does not reverse its sign when the AOI reversed.

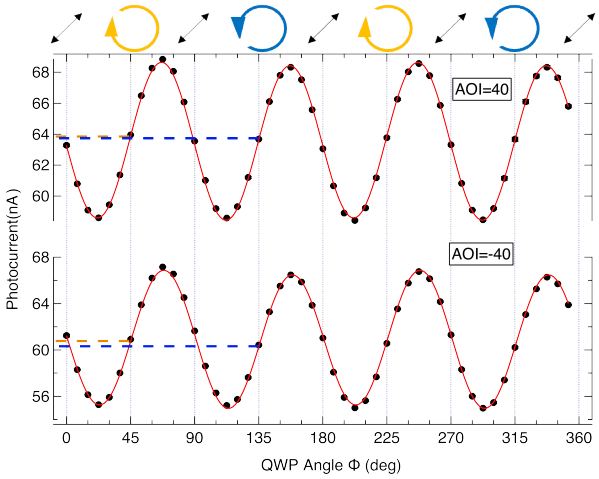

(a)

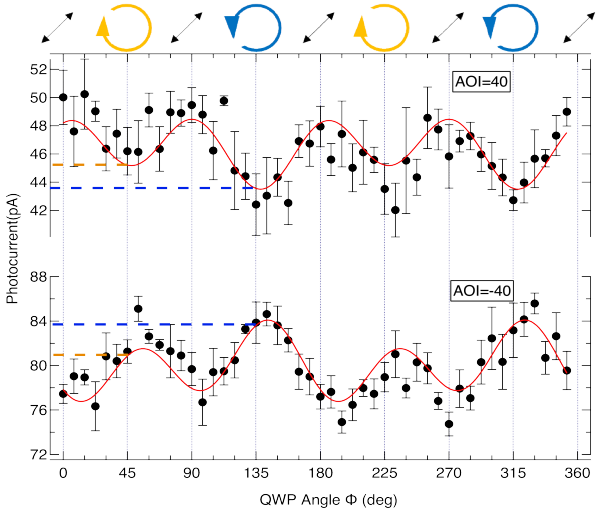

(b)

Figure 5.41: Photocurrent measured by (a) 635 nm and (b) 1550 nm wavelength lasers. HDP at 635 nm wavelength illumination does not reverse when AOI changed from 40° to -40°.

Position dependence is also measured by the 1550 nm wavelength laser. As a result, no ISHE like position dependence was observed.

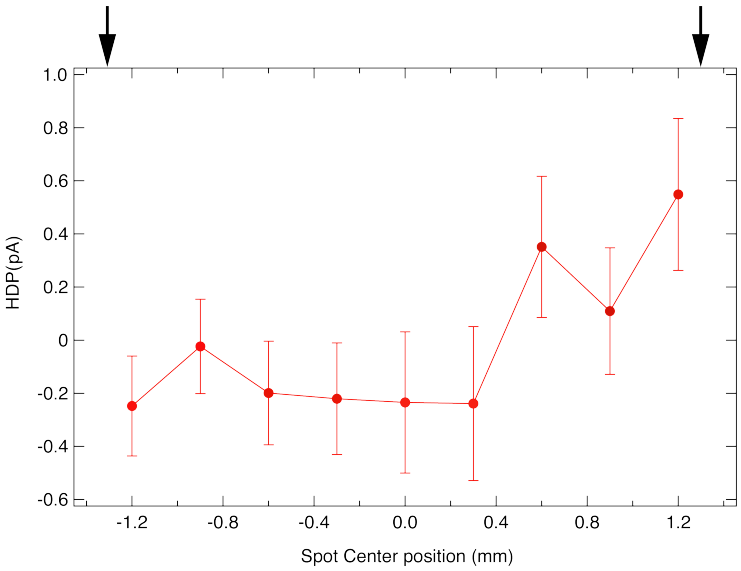

Figure 5.42: Position dependence of HDP under normal incidence by the 1550 nm wavelength laser. No ISHE like behavior was observed.

5.5.1 Discussion

Previously, Okada *et al* have already investigated the CPGE in $(Bi_xSb_{1-x})_2Te_3$, and found that the HDP of CPGE is modulated by changing compounds ratio [14]. By changing the compounds ratio, Fermi level is adjusted that it crosses TSSs only. It is only within the bulk insulating region that the HDP is greatly enhanced. Therefore, Okada *et al* conclude that scattering events occur between the TSSs and the bulk states during the photoexcitation which would influence the HDP generation, under the preassumption that the photocurrent is mainly come from the photoexcitation of the states around the Fermi level. And tunning a bulk insulated sample is essential for suppressing the scattering between the bulk and TSSs.

In our experiments, we observed a similar HDP dependence of the compounds ratio under oblique incidence, especially by 1550 nm wavelength excitation. Similar to Bi_2Se_3 case, HDP excited by the 635 nm wavelength laser is more likely to be CPDE. Whereas HDP excited by the 1550 nm wavelength laser is more CPGE like, especially as shown in Fig. 5.37 a clear antisymmetric CPGE behavior is observed. Due to the large photon energy of the 635 nm wavelength laser, the excitation path is not in the vicinity of Fermi surface thus merely not affected by the change of Fermi level.

Besides, we observed a different feature that didn't present in the previous Okada's report. As one can see the data acquired by the 1550 nm wavelength laser in Fig. 5.37 and Fig. 5.41, the HDP is opposite between Sb_2Te_3 and Bi_2Te_3, which means the HDP reversed when the Fermi level changes from BVB to BCB. This actually reveals the photoexcitation paths between the TSSs and bulk states. As shown in the Fig. 5.43, the HDP will depends on the Fermi level position when the photoexcitation is between TSSs and bulk states, even if the excitation is not exactly at the Fermi level. When the Fermi level is

in the BVB or lower Dirac cone, as the case of Sb_2Te_3, only the excitation path BVB→TSSs is available and the HDP is determined by this path. When the Fermi level position is within the Dirac cone around the Dirac point, as the case of $(Bi_{0.45}Sb_{0.55})_2Te_3$, both BVB→TSSs and TSSs→BCB are enabled, but the total photocurrent is zero due to the symmetry. Finally, when the Fermi level is in BCB or upper Dirac cone, as the case of Bi_2Te_3, only the excitation path TSSs→BCB is available so the HDP is determined by this path and opposite to the case when Fermi level is in BVB or lower Dirac cone. This kind of photocurrent has been predicted by theory previously [94]. It is said that the photocurrent due to the excitation between bulk states and TSSs would dominate the HDP, and this part of the HDP is not necessarily protected against the backscattering thus spin polarization could be low.

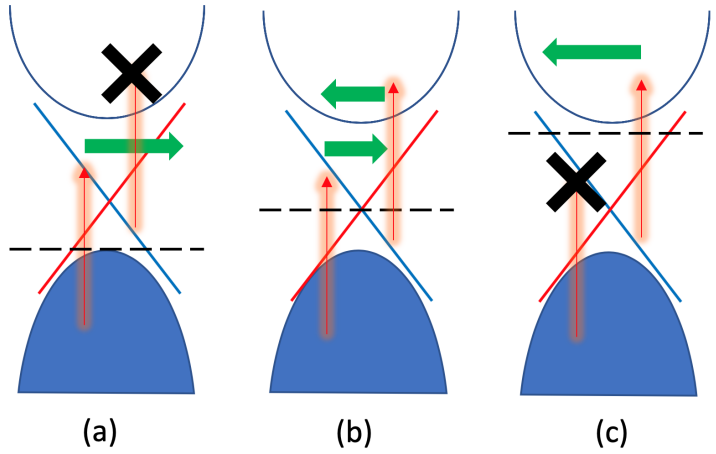

Figure 5.43: Model of the Fermi level dependent HDP. Red arrow is the excitation path by a certain circularly polarized light, green arrow is the photocurrent, dashed black line is the Fermi level. Black cross marks the forbidden excitation path. (a) When Fermi level is in BVB or lower Dirac cone, the excitation path is BVB→TSSs. (b) When Fermi level is around the Dirac point, both BVB→TSSs and TSSs→BCB are possible. The total HDP is zero due to the symmetry in k space. (c) When Fermi level is in BCB or upper Dirac cone, the excitation path is TSSs→BCB.

More importantly, we found the HDP at normal incidence is also affected by the changing of the compound's ratio. As we described in previous section, the laser spot position dependence of the HDP at normal incidence is due to ISHE. In addition, we suspect the out-of-plane spin is originated from the hexagonal warping part of the TSSs. In our experiments, only the bulk insulating $(Bi_{0.45}Sb_{0.55})_2Te_3$ shows a clear position dependent HDP at normal incidence. Two possible reasons for explaining this Fermi level dependence. First, a certain energy level on the TSSs is mainly responsible for the position dependent HDP, so this excitation can be turned on and off depending on the Fermi level position. Second, similar to Okada's explanation, bulk insulating sample strongly suppressed the spin scattering which makes the ISHE results larger than the bulk non-insulating samples. The second hypothesis could be

verified by cooling the bulk non-insulating samples, which could also suppress the spin scattering.

An interesting observation about the HDP at normal incidence in $(Bi_{0.45}Sb_{0.55})_2Te_3$ is that the position dependence of the HDP is opposite to the one observed in Bi_2Se_3, as in Fig. 5.40 and Fig. 5.20. As we mentioned in the discussion part of Bi_2Se_3, the mechanism of this HDP is the ISHE. So, the results from these two materials should be the same since the hexagonal warping TSSs, the helicity of the light and the spin Hall angle are similar. The possible explanation for the opposite result is that the origins for those two materials are different. As shown in Fig. 2.7, Bi_2Se_3 also possesses a Rashba state with hexagonal warping in addition to the TSSs, which could lead to a opposite excited spin compared with the excitation in TSSs. As a result, the ISHE induced HDP in Bi_2Se_3 should be the combination results of Rashba states and TSSs, whereas the ISHE induced HDP in $(Bi_{0.45}Sb_{0.55})_2Te_3$ is only from TSSs. If the Rashba states in Bi_2Se_3 dominates the ISHE induced HDP, the total result of the Bi_2Se_3 could be opposite to the result in $(Bi_{0.45}Sb_{0.55})_2Te_3$.

Chapter 6

Conclusions and outlook

During this research, we successfully observed the HDP on various materials with strong SOC by our *in-situ* measurement system. We have used several experimental techniques to solve the questions we raised at the beginning of this thesis.

Variable	Purpose
AOI	Distinguish between CPGE and CPDE
Thickness	Check the relation between TSSs and HDP, Top and bottom TSSs contribution
Wavelength	Check the relation between TSSs and HDP Check the wavelength respond of CPGE or CPDE
Fermi level position	Check the relation between TSSs and HDP
Spot position	Check the ISHE by out-of-plane spin

With these experimental methods we are able to verify that both CPGE and CPDE mechanisms are presented in the HDP generation, and CPDE seems to dominate in the 635 nm wavelength illumination while CPGE is profound in 1550 nm wavelength illumination. Besides, HDP at 1550 nm wavelength illumination is probably more related to TSSs of TIs than that at 635 nm wavelength illumination. Finally, ISHE due to photoexcited out-of-plane spin is observed in TIs with hexagonal warping. As a result, this work settled the ground hypothesis and ambiguous points in this field with solid experimental evidences, and further provide a new angle for optical spin orientation in strong spin-orbit coupling materials.

There are some key findings we want to emphasize here.

- It is observed that different mechanisms contribute to HDP.

It is clearly shown in Sec. 5.1 and Sec. 5.3.2 that different mechanisms, namely CPDE and CPGE, could contribute to the observation of HDP. It needs to be distinguish by methods, such as sample symmetry analysis and AOI dependence measurement like we did in Fig. 5.13 and Fig. 5.14, before rush to the conclusion that HDP is due CPGE.

- HDP of CPGE will change its direction when TSSs evolves from Rashba states to the helical Dirac cone surface states when the film thickness increase.

When measuring the AOI dependence versus the Bi_2Se_3 thickness as shown in Fig. 5.14, we observed the tendency of the AOI dependence changes as the sample thickness changes from 4 QL thick to 7 QL thick. More importantly, the asymmetric part of AOI dependence which is believed to be the result of CPGE changed its sign when the sample changes from 4 QL to 7 QL thick. It is natural that such HDP reverses its direction if we look into the evolution of the TSSs with the film thickness. When the TSSs evolve from the Rashba states to the helical Dirac cone surface states, the outer subband of the Rashba states is gone. With the same spin injected into this system by a circularly polarized light, the dominating band of the spin-to-charge conversion changes from the outer Rashba subband to the inner Rashba subband, as shown in Fig. 5.18. Therefore this reversing of HDP is inevitable when the HDP originates from TSSs.

- ISHE due to the asymmetrical illumination.

Out-of-plane spin can be injected into a TI by a circularly polarized light at normal incidence as we shown in Sec. 5.3.4. Spin current is generated due to the gradient in the density of excited carriers. This diffusing spin current is converted into a charge current by ISHE. When illuminating the edge of the sample, the charge current by ISHE forms an electrical dipole at the edge and causes a measurable potential difference along the sample, resulting in a HDP flowing in one direction as shown in Fig. 5.23. By shining the opposite edge of the sample, an electrical dipole with opposite polarity is generated, and the HDP flows in opposite direction. The result shown in this experiment reveals a simple way to control the output of the ISHE and could lead to novel spintronic devices.

- Fermi level dependence of the HDP.

HDP in TIs will be influenced by the Fermi level position above or below the Dirac point. In addition, it tends to influence the HDP due to in-plane spin and out-of-plane spin differently. This is probably due to the out-of-plane spin only exists position that far from the Dirac point of TSSs while the in-plane spin generally exists in a wide energy range of the helical Dirac cone.

With experimental results we have from the Si(111), Bi_2Se_3, Bi(111) and $(Bi_xSb_{1-x})_2Te_3$, we can now try to answer the questions we raised at the beginning of this thesis.

1. *Does HDP commonly exist in strong SOC materials?*

Our measurements shows that except for the Si(111), all of our samples (with strong SOC) exhibit HDP under certain wavelength illumination. However, the mechanisms and magnitudes of the HDP strongly depends on the particular experimental geometry, i.e. AOI and wavelength of illuminating light, illumination position on the sample, e.t.c.

2. *A lot of researches have been done in TIs with different wavelengths of laser. As a result, they all observed HDP and claimed the TSSs could be the origin. Is that correct that HDP can be observed in TIs almost at any wavelength and originated from TSSs?*

We have observed HDP by lasers at 635 nm and 1550 nm wavelengths in our measurements. It is probably true that that HDP can be observed in TIs in a large range of wavelengths due to their naturally complex spin texture in bulk and surface bands. However, it is not true that all wavelengths can excite electrons in TSSs. As our AOI dependence and position dependence measurements shown that HDP by 635 nm and 1550 nm wavelength illumination exhibit different behaviors. CPDE is the main mechanism driving the HDP under 635 nm wavelength illumination, while CPGE and CPDE are both observed at 1550 nm wavelength illumination. With further investigation of the thickness dependence, we can conclude that HDP at 1550 nm wavelength illumination probably related with the TSSs, based on the evidences that AOI and position dependence of HDP change when using 4 QL and 7 QL thick samples, and the CPGE part of the HDP reversed its direction from 4 QL to 7 QL sample. These findings suggest that we need to be careful when concluding the mechanism and origin of the HDP.

3. *The previous reports based on Rashba SOC materials and TIs reveals that incident angle dependence of HDP is originated from the in-plane spin nature of those surface states. Is it certain that the out-of-plane spin cannot be injected into those materials?*

HDP at normal incidence of light is usually forbidden by symmetry for CPGE or CPDE mechanism in samples with C_{3v} symmetry. However, we observed an HDP at the edge of a TI edges by 1550 nm wavelength laser at normal incidence. With analysis and simulations, we conclude that ISHE with the out-of-plane spin component in TSSs could be the answer of this edge HDP at normal incidence. This means that the out-of-plane spin can be injected into TIs. With the conclusion that we previous have, HDP at 1550 nm wavelength illumination probably related with TSSs, we conclude that hexagonal warping part of the TSSs could be the origin of the out-of-plane spin. Furthermore, $(Bi_xSb_{1-x})_2Te_3$ samples enable us to change the Fermi level position and investigate the influence of the Fermi level position. We found that the bulk insulating sample is the best for this ISHE to be observed, and this further suggests that TSSs might be important for HDP in $(Bi_xSb_{1-x})_2Te_3$ under 1550 nm illumination.

Besides those findings, we have noticed a few points that need further improvement or study.

- Extinction coefficient of light in bismuth is very large due to its metallic nature, which makes the light absorption in bismuth very difficult especially at the long wavelength region. Perhaps the way to observe CPGE in bismuth is to make it more semiconducting to lowering the extinction coefficient by making ultra-thin film or disordered bismuth film.
- Acquiring HDP through fitting is acceptable when the original data is stable and with good signal-to-noise ratio. It is difficult to use this method when measuring a varying process like cooling. Photoelastic modulator (PEM) should be used to measure, rather than fitting, to get the HDP during a fast-varying process.
- For our current measurement system, it is better to add electrodes in the x-axis to measure the photocurrent in x-direction. In this way, we can

investigate the spin injection from the substrate to samples with applying a magnetic field in x-direction under normal incidence.

- More samples should be made to get a clearer picture of the Fermi surface influence on HDP. Currently, we only have three samples to describe the influence of Fermi level position and there is no sample which Fermi level cross the lower half of the Dirac cone.

- Mn- or Cr- doped topological insulator shows a complex spin texture in their bands. It is predicted that large circular dichroism can be observed on TIs when gap is opened [206]. Besides, previous ARPES measurements show that spin texture in TSSs changes to out-of-plane component dominating[207]. This might be a large enhancement of the HDP by ISHE.

Acknowledgement

I would like to thank my supervisor **Prof. Shuji Hasegawa** who led me into the interesting surface physics. His unique perspectives and profound knowledges in surface science have been helping me a lot in my research.

I want to thank my vice supervisor **Prof. Atsushi Fujimori** during the first two years of ALPS course. His kindness and erudition in optics supports my research a lot.

I would like to thank my vice supervisor **Prof. Akira Furusawa** in the last year of ALPS course. His guidance in optics and lasers helps me with many questions.

I appreciate the help from **Mr. Rei Hobara** who helped me a lot during my modifying the setup and gave me a lot of advices on experimental methods. He helps me with a lot difficult and crucial questions in research.

I'm very grateful to **Dr. Ryota Akiyama** who directly advised and supported my experiments. Thank you for all the supports and for introducing me to the collaboration with other groups.

Besides staffs who supported my research directly, I also want to thank **Dr. Yukihiro Endo** for helping me with my trivial affairs in the first few months after I arrived in Japan. Besides your humor makes me have a very pleasant time in Hasegawa lab and I really enjoy hanging out with you. **Ms. Kyoko Tanaka**, thank you for your hard work to make our research goes smoothly. I would like to thank **Mr. Zhendong Chi** for discussing physics with me all the time. I would like to thank **Mr. Hongrui Huang** for hanging out and discussing physical and mathematical problems with me. **Miss. Haruko Toyama** your hard working inspired me a lot. **Mr. Shengpeng Liu** good luck with your experiments. **Mr. Takuya Takashiro** shares the same machine with me, he is serious when doing experiments but easygoing in daily life. Good luck on the way to PhD degree. **Mr. Yuxiao Guo** travels with me a lot, and I really enjoy the accompany. For all the master's course students in Hasegawa lab: **Mr. Kowata Hiwatari**, **Mr. Jehong Jung**, **Ibuki Taniuchi** and **Mr. Syunsuke Sato**, enjoy your life in these years but don't waste time, two years of master's course is really quick. Wish you all have a good research result.

I also want to acknowledge the ex-members of Hasegawa lab: **Dr. Tomonori Nakamura**, **Dr. Akari Takayama**, **Dr. Jianlin Wang**, **Dr. Naoya Fukui**, **Mr. Hirotaka Ishihara**, **Dr. Satoru Ichinokura**, **Mr. Yasunori Takeuchi**, **Mr. Keita Miyauchi**, **Mr. Ryosuke Nakanishi**, and **Mr. Kazumi Watanabe**. Thank you all for helping me and making studying in this lab a pleasure, it is really nice to meet you here. Wish you all the best with your current position.

I'd like to thank **Prof. Jingbo Qi** for guiding me into the interesting condensed matter physics and optics. Thanks for introducing me to Prof. Li at Univ. of Utah. Thanks **Prof. Sarah Li** for taking me into her group as a visiting scholar, and thanks **Mr. Yue Yao** for taking care of me during the days I was in Salt Lake City. Also, I want to thank ALPS for the financial support for this visiting.

I want to thank **Dr. Josh Zhao**, **Dr. Yoshitaka Matsui**, **Ms. Kate Ishikawa**, **Ms.Naomi Iwasato**, **Mr. Yoshikazu Sakamoto**, **Mr. Kenya Ogata** and **Jin Watanuki** for taking care of me during the internship. I have learned a lot in this internship.

I want to thank for the financial support during these years from the **Advanced Leading Graduate Course for Photon Science (ALPS)** of the MEXT "Program for Leading Graduate Schools". I learned a lot of knowledges in chemistry and industry during the course which widen my vision in research.

At last, I want to thank to my parents, **Ms. Huiping Fan** and **Mr. Guangxiang Fan**, for supporting my studying abroad, for giving me consolation when I feel lost, and for making me who I am.

Bibliography

[1] SA Wolf, DD Awschalom, RA Buhrman, JM Daughton, von S von Molnár, ML Roukes, A Yu Chtchelkanova, and DM Treger. Spintronics: a spin-based electronics vision for the future. *Science*, 294(5546):1488–1495, 2001.

[2] Satoshi Sugahara and Junsaku Nitta. Spin-transistor electronics: an overview and outlook. *Proceedings of the IEEE*, 98(12):2124–2154, 2010.

[3] Supriyo Datta and Biswajit Das. Electronic analog of the electro-optic modulator. *Applied Physics Letters*, 56(7):665–667, 1990.

[4] Charles L Kane and Eugene J Mele. Quantum spin Hall effect in graphene. *Physical review letters*, 95(22):226801, 2005.

[5] MZ Hasan and CL Kane. Colloquium: topological insulators. *Reviews of Modern Physics*, 82(4):3045, 2010.

[6] CL Kane and EJ Mele. Z_2 Topological Order and the Quantum Spin Hall Effect. *Physical Review Letters*, 95:146802, 2005.

[7] B Andrei Bernevig, Taylor L Hughes, and Shou-Cheng Zhang. Quantum spin hall effect and topological phase transition in hgte quantum wells. *Science*, 314(5806):1757–1761, 2006.

[8] Markus König, Steffen Wiedmann, Christoph Brüne, Andreas Roth, Hartmut Buhmann, Laurens W Molenkamp, Xiao-Liang Qi, and Shou-Cheng Zhang. Quantum spin Hall insulator state in HgTe quantum wells. *Science*, 318(5851):766–770, 2007.

[9] CM Schneider and J Kirschner. Spin-and angle-resolved photoelectron spectroscopy from solid surfaces with circularly polarized light. *Critical Reviews in Solid State and Material Sciences*, 20(3):179–283, 1995.

[10] F Pezzoli, F Bottegoni, D Trivedi, F Ciccacci, A Giorgioni, P Li, S Cecchi, E Grilli, Y Song, and M Guzzi. Optical spin injection and spin lifetime in Ge heterostructures. *Physical Review Letters*, 108(15):156603, 2012.

[11] N Ogawa, MS Bahramy, Y Kaneko, and Y Tokura. Photocontrol of Dirac electrons in a bulk Rashba semiconductor. *Physical Review B*, 90(12):125122, 2014.

[12] S Giglberger, LE Golub, VV Bel'kov, SN Danilov, D Schuh, C Gerl, F Rohlfing, J Stahl, W Wegscheider, and D Weiss. Rashba and Dresselhaus spin splittings in semiconductors measured by spin photocurrents. *Physical Review B*, 75(3):035327, 2007.

[13] JW McIver, D Hsieh, H Steinberg, P Jarillo-Herrero, and N Gedik. Control over topological insulator photocurrents with light polarization. *Nature Nanotechnology*, 7(2):96–100, 2012.

[14] KN Okada, N Ogawa, R Yoshimi, A Tsukazaki, KS Takahashi, M Kawasaki, and Y Tokura. Enhanced photogalvanic current in topological insulators via fermi energy tuning. *Physical Review B*, 93(8):081403, 2016.

[15] H Yuan, X Wang, B Lian, H Zhang, X Fang, B Shen, G Xu, Y Xu, SC Zhang, HY Hwang, et al. Generation and electric control of spin–valley-coupled circular photogalvanic current in WSe_2. *Nature nanotechnology*, 9(10):851–857, 2014.

[16] M Eginligil, B Cao, Z Wang, X Shen, C Cong, J Shang, C Soci, and T Yu. Dichroic spin-valley photocurrent in monolayer molybdenum disulphide. *Nature Communications*, 6, 2015.

[17] V.M. Tuchkevich and V. Ya. Frenkel. *Semiconductor Physics*. New York : Consultants Bureau, 1986. Includes index.

[18] Jinling Yu, Kejing Zhu, Xiaolin Zeng, Lei Chen, Yonghai Chen, Yu Liu, Chunming Yin, Shuying Cheng, Yunfeng Lai, Jin Huang, et al. Helicity-dependent photocurrent of the top and bottom dirac surface states of epitaxial thin films of three-dimensional topological insulators Sb_2Te_3. *Physical Review B*, 100(23):235108, 2019.

[19] J Karch, P Olbrich, M Schmalzbauer, C Zoth, C Brinsteiner, M Fehrenbacher, U Wurstbauer, MM Glazov, SA Tarasenko, and EL Ivchenko. Dynamic hall effect driven by circularly polarized light in a graphene layer. *Physical Review Letters*, 105(22):227402, 2010.

[20] Jean Besbas, Karan Banerjee, Jaesung Son, Yi Wang, Yang Wu, Matthew Brahlek, Nikesh Koirala, Jisoo Moon, Seongshik Oh, and Hyunsoo Yang. Helicity-dependent photovoltaic effect in Bi_2Se_3 under normal incident light. *Advanced Optical Materials*, 4(10):1642–1650, 2016.

[21] J Duan, N Tang, X He, Y Yan, S Zhang, X Qin, X Wang, X Yang, F Xu, and Y Chen. Identification of helicity-dependent photocurrents from topological surface states in Bi_2Se_3 gated by ionic liquid. *Scientific Reports*, 4, 2014.

[22] Siyuan Luo. Infrared circular photogalvanic effect in topological insulators. In *AIP Conference Proceedings*, volume 1955, page 040086. AIP Publishing LLC, 2018.

[23] Lukas Braun, Gregor Mussler, Andrzej Hruban, Marcin Konczykowski, Thomas Schumann, Martin Wolf, Markus Münzenberg, Luca Perfetti, and

Tobias Kampfrath. Ultrafast photocurrents at the surface of the three-dimensional topological insulator Bi_2Se_3. *Nature communications*, 7(1):1–9, 2016.

[24] HA Kramers. General theory of paramagnetic rotation in crystals. In *Proc. Acad. Sci. Amsterdam*, volume 33, page 959, 1930.

[25] D Stein, KV Klitzing, and G Weimann. Electron spin resonance on GaAs− $al_xga_{1-x}As$ heterostructures. *Physical Review Letters*, 51:130–133, 1983.

[26] S LaShell, BA McDougall, and E Jensen. Spin Splitting of an Au(111) Surface State Band Observed with Angle Resolved Photoelectron Spectroscopy. *Physical Review Letters*, 77:3419–3422, 1996.

[27] L Petersen and P Hedegård. A simple tight-binding model of spin–orbit splitting of sp-derived surface states. *Surface Science*, 459(1–2):49 – 56, 2000.

[28] JD Jackson. *Electrodynamics*. Wiley Online Library, 1975.

[29] EI Rashba. Properties of semiconductors with an extremum loop. 1. cyclotron and combinational resonance in a magnetic field perpendicular to the plane of the loop. *Sov. Physical Solid State*, 2(6):1109–1122, 1960.

[30] G Bihlmayer, YM Koroteev, PM Echenique, EV Chulkov, and S Blügel. The rashba-effect at metallic surfaces. *Surface Science*, 600(18):3888–3891, 2006.

[31] J Henk, M Hoesch, J Osterwalder, A Ernst, and P Bruno. Spin–orbit coupling in the l-gap surface states of Au(111): spin-resolved photoemission experiments and first-principles calculations. *Journal of Physics: Condensed Matter*, 16(43):7581, 2004.

[32] Michael Victor Berry and Mark Wilkinson. Diabolical points in the spectra of triangles. *Proceedings of the Royal Society of London. A. Mathematical and Physical Sciences*, 392(1802):15–43, 1984.

[33] Di Xiao, Ming-Che Chang, and Qian Niu. Berry phase effects on electronic properties. *Reviews of modern physics*, 82(3):1959, 2010.

[34] Michael Victor Berry. Quantal phase factors accompanying adiabatic changes. *Proceedings of the Royal Society of London. A. Mathematical and Physical Sciences*, 392(1802):45–57, 1984.

[35] FDM Haldane. Berry curvature on the Fermi surface: anomalous Hall effect as a topological Fermi-liquid property. *Physical review letters*, 93(20):206602, 2004.

[36] Naoto Nagaosa, Jairo Sinova, Shigeki Onoda, Allan H MacDonald, and Nai Phuan Ong. Anomalous Hall effect. *Reviews of modern physics*, 82(2):1539, 2010.

[37] Tsuneya Ando, Takeshi Nakanishi, and Riichiro Saito. Berry's phase and absence of back scattering in carbon nanotubes. *Journal of the Physical Society of Japan*, 67(8):2857–2862, 1998.

[38] Hai-Zhou Lu and Shun-Qing Shen. Weak localization and weak anti-localization in topological insulators. In *Spintronics Vii*, volume 9167, page 91672E. International Society for Optics and Photonics, 2014.

[39] Cheol-Hwan Park and Nicola Marzari. Berry phase and pseudospin winding number in bilayer graphene. *Physical Review B*, 84(20):205440, 2011.

[40] Ming-Che Chang. Effect of in-plane magnetic field on the spin Hall effect in a Rashba-Dresselhaus system. *Physical Review B*, 71(8):085315, 2005.

[41] Shun-Qing Shen. Spin Hall effect and Berry phase in two-dimensional electron gas. *Physical Review B*, 70(8):081311, 2004.

[42] Zengwei Zhu, Benoît Fauqué, Yuki Fuseya, and Kamran Behnia. Angle-resolved landau spectrum of electrons and holes in bismuth. *Physical Review B*, 84(11):115137, 2011.

[43] H Murakawa, MS Bahramy, M Tokunaga, Y Kohama, C Bell, Y Kaneko, N Nagaosa, HY Hwang, and Y Tokura. Detection of Berry's phase in a bulk Rashba semiconductor. *Science*, 342(6165):1490–1493, 2013.

[44] SD Ganichev, VV Bel'kov, LE Golub, EL Ivchenko, P Schneider, S Giglberger, J Eroms, J De Boeck, G Borghs, W Wegscheider, D Weiss, and W Prettl. Experimental Separation of Rashba and Dresselhaus Spin Splittings in Semiconductor Quantum Wells. *Physical Review Letters*, 92:256601, 2004.

[45] SD Ganichev and LE Golub. Interplay of Rashba/Dresselhaus spin splittings probed by photogalvanic spectroscopy–A Review. *Physica Status Solidi (B)*, 251(9):1801–1823, 2014.

[46] Paul Adrien Maurice Dirac. The quantum theory of the electron. *Proceedings of the Royal Society of London. Series A, Containing Papers of a Mathematical and Physical Character*, 117(778):610–624, 1928.

[47] Paul Adrien Maurice Dirac. *The principles of quantum mechanics*. Number 27. Oxford university press, 1981.

[48] Shun-Qing Shen, Wen-Yu Shan, and Hai-Zhou Lu. Topological insulator and the Dirac equation. In *Spin*, volume 1, pages 33–44. World Scientific, 2011.

[49] Shun-Qing Shen. *Topological insulators*, volume 174. Springer, 2012.

[50] H Zhang, CX Liu, XL Qi, X Dai, Z Fang, and SC Zhang. Topological insulators in Bi_2Se_3, Bi_2Te_3 and Sb_2Te_3 with a single Dirac cone on the surface. *Nature Physics*, 5(6):438–442, 2009.

[51] C Jozwiak, CH Park, K Gotlieb, C Hwang, DH Lee, SG Louie, JD Denlinger, CR Rotundu, RJ Birgeneau, and Z Hussain. Photoelectron spin-flipping and texture manipulation in a topological insulator. *Nature Physics*, 9(5):293–298, 2013.

[52] D Hsieh, D Qian, L Wray, YQ Xia, YS Hor, RJ Cava, and MZ Hasan. A topological Dirac insulator in a quantum spin Hall phase. *Nature*, 452(7190):970–974, 2008.

[53] David Hsieh, Yuqi Xia, Dong Qian, L Wray, JH Dil, Fedorov Meier, J Osterwalder, L Patthey, JG Checkelsky, Nai Phuan Ong, et al. A tunable topological insulator in the spin helical Dirac transport regime. *Nature*, 460(7259):1101–1105, 2009.

[54] YL Chen, James G Analytis, J-H Chu, ZK Liu, S-K Mo, Xiao-Liang Qi, HJ Zhang, DH Lu, Xi Dai, Zhong Fang, et al. Experimental realization of a three-dimensional topological insulator, Bi_2Te_3. *Science*, 325(5937):178–181, 2009.

[55] Liang Fu. Hexagonal warping effects in the surface states of the topological insulator Bi_2Te_3. *Physical review letters*, 103(26):266801, 2009.

[56] Emmanouil Frantzeskakis and Marco Grioni. Anisotropy effects on Rashba and topological insulator spin-polarized surface states: a unified phenomenological description. *Physical Review B*, 84(15):155453, 2011.

[57] PDC King, RC Hatch, M Bianchi, R Ovsyannikov, C Lupulescu, G Landolt, B Slomski, JH Dil, D Guan, and JL Mi. Large tunable rashba spin splitting of a two-dimensional electron gas in Bi_2Se_3. *Physical Review Letters*, 107(9):096802, 2011.

[58] S Souma, K Kosaka, T Sato, M Komatsu, A Takayama, T Takahashi, M Kriener, Kouji Segawa, and Yoichi Ando. Direct measurement of the out-of-plane spin texture in the Dirac-cone surface state of a topological insulator. *Physical review letters*, 106(21):216803, 2011.

[59] Zhanybek Alpichshev, JG Analytis, J-H Chu, Ian R Fisher, YL Chen, Zhi-Xun Shen, Alan Fang, and Aharon Kapitulnik. STM imaging of electronic waves on the surface of Bi_2Te_3: topologically protected surface states and hexagonal warping effects. *Physical review letters*, 104(1):016401, 2010.

[60] Mei-Mei Wu, Zhi-Ming Yu, and Hui Pan. The anisotropic effect of hexagonal warping on the transport. *Physics Letters A*, 383(2-3):237–242, 2019.

[61] Chuang Li, Lun-Hui Hu, and Fu-Chun Zhang. Hexagonal warping effect on Majorana zero modes at the ends of superconducting vortex lines in doped strong 3D topological insulators. *SCIENCE CHINA Physics, Mechanics & Astronomy*, 62(11):117411, 2019.

[62] Mikhail I Dyakonov and VI Perel. Current-induced spin orientation of electrons in semiconductors. *Physics Letters A*, 35(6):459–460, 1971.

[63] Yuichiro K Kato, Roberto C Myers, Arthur C Gossard, and David D Awschalom. Observation of the spin Hall effect in semiconductors. *Science*, 306(5703):1910–1913, 2004.

[64] Yasuhiro Niimi and YoshiChika Otani. Reciprocal spin Hall effects in conductors with strong spin-orbit coupling: a review. *Reports on progress in physics*, 78(12):124501, 2015.

[65] Robert Karplus and JM Luttinger. Hall effect in ferromagnetics. *Physical Review*, 95(5):1154, 1954.

[66] Jinwu Ye, Yong Baek Kim, AJ Millis, BI Shraiman, P Majumdar, and Z Tešanović. Berry phase theory of the anomalous Hall effect: Application to colossal magnetoresistance manganites. *Physical review letters*, 83(18):3737, 1999.

[67] T Tanaka, Hiroshi Kontani, Masayuki Naito, T Naito, Dai S Hirashima, K Yamada, and J Inoue. Intrinsic spin Hall effect and orbital Hall effect in 4d and 5d transition metals. *Physical Review B*, 77(16):165117, 2008.

[68] M Morota, Y Niimi, Kohei Ohnishi, DH Wei, T Tanaka, H Kontani, Takashi Kimura, and Y Otani. Indication of intrinsic spin Hall effect in 4d and 5d transition metals. *Physical Review B*, 83(17):174405, 2011.

[69] Jan Smit. The spontaneous Hall effect in ferromagnetics II. *Physica*, 24(1-5):39–51, 1958.

[70] Luc Berger. Side-jump mechanism for the hall effect of ferromagnets. *Physical Review B*, 2(11):4559, 1970.

[71] A Crépieux and P Bruno. Theory of the anomalous Hall effect from the Kubo formula and the Dirac equation. *Physical Review B*, 64(1):014416, 2001.

[72] Cong Xiao, Yi Liu, Zhe Yuan, Shengyuan A Yang, and Qian Niu. Temperature dependence of the side-jump spin Hall conductivity. *Physical Review B*, 100(8):085425, 2019.

[73] Albert Fert and Peter M Levy. Spin Hall effect induced by resonant scattering on impurities in metals. *Physical review letters*, 106(15):157208, 2011.

[74] Naoto Nagaosa, Jairo Sinova, Shigeki Onoda, Allan H MacDonald, and Nai Phuan Ong. Anomalous Hall effect. *Reviews of modern physics*, 82(2):1539, 2010.

[75] Peter Schwab, Roberto Raimondi, and Cosimo Gorini. Inverse spin Hall effect and anomalous Hall effect in a two-dimensional electron gas. *EPL (Europhysics Letters)*, 90(6):67004, 2010.

[76] EM Hankiewicz and Giovanni Vignale. Phase diagram of the spin Hall effect. *Physical review letters*, 100(2):026602, 2008.

[77] Roberto Raimondi and Peter Schwab. Tuning the spin Hall effect in a two-dimensional electron gas. *EPL (Europhysics Letters)*, 87(3):37008, 2009.

[78] RH Silsbee. Theory of the detection of current-induced spin polarization in a two-dimensional electron gas. *Physical Review B*, 63:155305, 2001.

[79] HS Robert. Spin–orbit induced coupling of charge current and spin polarization. *Journal of Physics: Condensed Matter*, 16(7):R179, 2004.

[80] VM Edelstein. Spin polarization of conduction electrons induced by electric current in two-dimensional asymmetric electron systems. *Solid State Communications*, 73(3):233–235, 1990.

[81] HJ Zhang, S Yamamoto, B Gu, H Li, M Maekawa, Y Fukaya, and A Kawasuso. Charge-to-spin conversion and spin diffusion in Bi/Ag bilayers observed by spin-polarized positron beam. *Physical Review Letters*, 114(16):166602, 2015.

[82] JR Sánchez, L Vila, G Desfonds, S Gambarelli, JP Attané, JM De Teresa, and A Fert C Magén. Spin-to-charge conversion using Rashba coupling at the interface between non-magnetic materials. *Nature Communications*, 4, 2013.

[83] K Shen, G Vignale, and R Raimondi. Microscopic theory of the inverse Edelstein effect. *Physical Review Letters*, 112(9):096601, 2014.

[84] M Isasa, MC Martínez-Velarte, E Villamor, C Magén, L Morellón, J De Teresa, MR Ibarra, G Vignale, EV Chulkov, and EE Krasovskii. Origin of inverse Rashba-Edelstein effect detected at the Cu/Bi interface using lateral spin valves. *Physical Review B*, 93(1):014420, 2016.

[85] JR Sánchez, S Oyarzún, Y Fu, A Marty, C Vergnaud, S Gambarelli, L Vila, M Jamet, Y Ohtsubo, and A Taleb-Ibrahimi. Spin to charge conversion at room temperature by spin pumping into a new type of topological insulator: α-Sn films. *Physical Review Letters*, 116(9):096602, 2016.

[86] S Caprara. Oxide interfaces: Spin-to-charge current conversion. *Nature Materials*, 15(12):1224–1225, 2016.

[87] Chao-Xing Liu, Xiao-Liang Qi, HaiJun Zhang, Xi Dai, Zhong Fang, and Shou-Cheng Zhang. Model Hamiltonian for topological insulators. *Physical Review B*, 82(4):045122, 2010.

[88] Mikhail A Kats and Federico Capasso. Optical absorbers based on strong interference in ultra-thin films. *Laser & Photonics Reviews*, 10(5):735–749, 2016.

[89] SG Tomlin. Optical reflection and transmission formulae for thin films. *Journal of Physics D: applied Physics*, 1(12):1667, 1968.

[90] Oliver S Heavens. *Optical properties of thin solid films*. Courier Corporation, 1991.

[91] Anatoly Barybin and Victor Shapovalov. Substrate effect on the optical reflectance and transmittance of thin-film structures. *International Journal of Optics*, 2010, 2010.

[92] Mikhail A Kats, Romain Blanchard, Patrice Genevet, and Federico Capasso. Nanometre optical coatings based on strong interference effects in highly absorbing media. *Nature materials*, 12(1):20–24, 2013.

[93] Yves Joly. Interaction matter-polarized light, 2009.

[94] Alexandra Junck. *Theory of photocurrents in topological insulators*. PhD thesis, 2015.

[95] CR Hammond, JR Jenkins, and CR Stanley. Optical rectification in tellurium from 10.6 μm. *Opto-electronics*, 4(3):189–196, 1972.

[96] RW Boyd. *Nonlinear optics*. Academic press, 2003.

[97] AM Glass, D Von der Linde, DH Auston, and TJ TJ Negran. Excited state polarization, bulk photovoltaic effect and the photorefractive effect in electrically polarized media. *Journal of Electronic Materials*, 4(5):915–943, 1975.

[98] VI Belinicher and BI Sturman. The photogalvanic effect in media lacking a center of symmetry. *Physics-Uspekhi*, 23(3):199–223, 1980.

[99] M Bieler, K Pierz, and U Siegner. Simultaneous generation of shift and injection currents in (110)-grown GaAs/AlGaAs quantum wells. *Journal of Applied Physics*, 100(8):083710, 2006.

[100] E Hecht. Note on an operational definition of the stokes parameters. *American Journal of Physics*, 38(9):1156–1158, 1970.

[101] H Fujiwara. *Spectroscopic ellipsometry: principles and applications*. John Wiley & Sons, 2007.

[102] EL Ivchenko. expression. *Physics-Uspekhi*, 45(12):1299–1303, 2002.

[103] EL Ivchenko and G Pikus. New photogalvanic effect in gyrotropic crystals. *JETP Lett*, 27(11):604–608, 1978.

[104] EL Ivchenko, G, and Pikus. *Superlattices and other heterostructures: symmetry and optical phenomena*, volume 110. Springer Science & Business Media, 2012.

[105] JE Sipe and AI Shkrebtii. Second-order optical response in semiconductors. *Physical Review B*, 61(8):5337, 2000.

[106] SD Ganichev, SN Danilov, VV Bel'kov, EL Ivchenko, H Ketterl, LE Vorobjev, M Bichler, W Wegscheider, and W Prettl. Nonlinear photogalvanic effect induced by monopolar spin orientation of holes in qws. *Physica E: Low-dimensional Systems and Nanostructures*, 10(1):52–56, 2001.

[107] SD Ganichev, EL Ivchenko, and W Prettl. Photogalvanic effects in quantum wells. *Physica E: Low-dimensional Systems and Nanostructures*, 14(1):166–171, 2002.

[108] SD Ganichev, VV Bel'kov, P Schneider, EL Ivchenko, SA Tarasenko, W Wegscheider, D Weiss, D Schuh, EV Beregulin, and W Prettl. Resonant inversion of the circular photogalvanic effect in n-doped quantum wells. *Physical Review B*, 68:035319, 2003.

[109] SD Ganichev, EL Ivchenko, SN Danilov, J Eroms, W Wegscheider, D Weiss, and W Prettl. Conversion of spin into directed electric current in quantum wells. *Physical Review Letters*, 86:4358–4361, 2001.

[110] Jinling Yu, Lijia Xia, Kejing Zhu, Qingao Pan, Xiaolin Zeng, Yong-Hai Chen, Yu Liu, Chunming Yin, Shuying Cheng, Yunfeng Lai, et al. Control of circular photogalvanic effect of surface states in the topological insulator Bi_2Te_3 via spin injection. *ACS Applied Materials & Interfaces*, 2020.

[111] YQ Huang, YX Song, SM Wang, IA Buyanova, and WM Chen. Spin injection and helicity control of surface spin photocurrent in a three dimensional topological insulator. *Nature communications*, 8(1):1–8, 2017.

[112] Hana Hirose, Naoto Ito, Masashi Kawaguchi, Yong-Chang Lau, and Masamitsu Hayashi. Circular photogalvanic effect in cu/bi bilayers. *Applied Physics Letters*, 113(22):222404, 2018.

[113] MM Glazov and SD Ganichev. High frequency electric field induced nonlinear effects in graphene. *Physics Reports*, 535(3):101–138, 2014.

[114] AF Gibson and MF Kimmitt. Photon drag detection. *Infrared and Millimeter Waves*, 3:181–217, 1980.

[115] VA Shalygin, H Diehl, C Hoffmann, SN Danilov, T Herrle, SA Tarasenko, D Schuh, C Gerl, W Wegscheider, and W Prettl. Spin photocurrents and the circular photon drag effect in (110)-grown quantum well structures. *JETP Letters*, 84(10):570–576, 2007.

[116] SN Danilov II Farbshtein LE Golub VA Shalygin, MD Moldavskaya. Circular photon drag effect in bulk tellurium. *Physical Review B*, 93(4):045207, 2016.

[117] H Plank, LE Golub, S Bauer, VV Bel'kov, T Herrmann, P Olbrich, M Eschbach, L Plucinski, CM Schneider, and J Kampmeier. Photon drag effect in $(Bi_{1-x}Sb_x)_2Te_3$ three-dimensional topological insulators. *Physical Review B*, 93(12):125434, 2016.

[118] Chongyun Jiang, VA Shalygin, V Yu Panevin, Sergey N Danilov, MM Glazov, Rositsa Yakimova, Samuel Lara-Avila, Sergey Kubatkin, and SD Ganichev. Helicity-dependent photocurrents in graphene layers excited by midinfrared radiation of a co_2 laser. *Physical Review B*, 84(12):125429, 2011.

[119] Peter Olbrich, Christoph Drexler, Leonid E Golub, Sergey N Danilov, VA Shalygin, Rositsa Yakimova, Samuel Lara-Avila, Sergey Kubatkin, B Redlich, Rupert Huber, et al. Reststrahl band-assisted photocurrents in epitaxial graphene layers. *Physical Review B*, 88(24):245425, 2013.

[120] AA Bakun, BP Zakharchenya, AA Rogachev, MN Tkachuk, and VG Fleisher. Observation of a surface photocurrent caused by optical orientation of electrons in a semiconductor. *JETP Lett*, 40(11), 1984.

[121] XW He, SB Shen, YH Chen, Q Zhang, K Han, CM Yin, N Tang, FJ Xu, CG Tang, and ZJ Yang. Anomalous photogalvanic effect of circularly polarized light incident on the two-dimensional electron gas in $Al_xGa_{1-x}N$/GaN heterostructures at room temperature. *Physical Review Letters*, 101(14):147402, 2008.

[122] F Mei, S Zhang, N Tang, J Duan, F Xu, Y Chen, W Ge, and B Shen. Spin transport study in a Rashba spin-orbit coupling system. *Scientific Reports*, 4:4030, 2014.

[123] Jinling Yu, Xiaolin Zeng, Liguo Zhang, Ke He, Shuying Cheng, Yunfeng Lai, Wei Huang, Yonghai Chen, Chunming Yin, and Qikun Xue. Photoinduced inverse spin Hall effect of surface states in the topological insulator Bi_2Se_3. *Nano letters*, 17(12):7878–7885, 2017.

[124] Di Fan, Rei Hobara, Ryota Akiyama, and Shuji Hasegawa. Inverse spin Hall effect induced by asymmetric illumination of light in topological insulator Bi_2Se_3. *Physical Review Research*, 2(2):023055, 2020.

[125] Peng Sheng, Yuya Sakuraba, Yong-Chang Lau, Saburo Takahashi, Seiji Mitani, and Masamitsu Hayashi. The spin nernst effect in tungsten. *Science advances*, 3(11):e1701503, 2017.

[126] Sibylle Meyer, Y-T Chen, Sebastian Wimmer, Matthias Althammer, T Wimmer, Richard Schlitz, S Geprägs, H Huebl, D Ködderitzsch, H Ebert, et al. Observation of the spin nernst effect. *Nature materials*, 16(10):977–981, 2017.

[127] Y Niinuma, Y Saisyu, T Hirahara, R Hobara, S Hasegawa, H Mizuno, and T Nagamura. Development of an UHV-SMOKE System Using Permanent Magnets. *e-Journal of Surface Science and Nanotechnology*, 8:298–302, 2010.

[128] Application Note. 3. about lock-in amplifiers. *Stanford Research Systems, Scientific and Engineering Instruments*, 1993:129, 1992.

[129] KG Libbrecht, ED Black, and CM Hirata. A basic lock-in amplifier experiment for the undergraduate laboratory. *American Journal of Physics*, 71(11):1208–1213, 2003.

[130] P Bak, C Tang, and K Wiesenfeld. Self-organized criticality: An explanation of the 1/f noise. *Physical Review Letters*, 59:381–384, 1987.

[131] S DeVore, A Gauthier, J Levy, and C Singh. Improving student understanding of lock-in amplifiers. *American Journal of Physics*, 84(1):52–56, 2016.

[132] MP Seah and WA Dench. Quantitative electron spectroscopy of surfaces: a standard data base for electron inelastic mean free paths in solids. *Surface and Interface Analysis*, 1(1):2–11, 1979.

[133] A Ichimiya and PI Cohen. *Reflection high-energy electron diffraction*. Cambridge University Press, 2004.

[134] Shuji Hasegawa. Reflection High-Energy Electron Diffraction. *Characterization of Materials*, pages 1–14, 2002.

[135] S Hasegawa, X Tong, S Takeda, N Sato, and T Nagao. Structures and electronic transport on silicon surfaces. *Progress in Surface Science*, 60(5):89–257, 1999.

[136] BA Joyce, PJ Dobson, JH Neave, K Woodbridge, Jing Zhang, PK Larsen, and B Bolger. RHEED studies of heterojunction and quantum well formation during MBE growth—from multiple scattering to band offsets. *Surface Science*, 168(1-3):423–438, 1986.

[137] Ph Hofmann. The surfaces of bismuth: Structural and electronic properties. *Progress in Surface Science*, 81(5):191–245, 2006.

[138] O. Madelung, U. Rössler, and M. Schulz, editors. *Bismuth (Bi) crystal structure, chemical bond*, pages 1–3. Springer Berlin Heidelberg, Berlin, Heidelberg, 1998.

[139] T Nagao, T Doi, T Sekiguchi, and S Hasegawa. Epitaxial growth of single-crystal ultrathin films of Bismuth on Si(111). *Japanese Journal of Applied Physics*, 39(7S):4567, 2000.

[140] C Bronner and P Tegeder. Relaxation dynamics of photoexcited charge carriers at the Bi (111) surface. *Physical Review B*, 89(11):115105, 2014.

[141] CA Hoffman, JR Meyer, FJ Bartoli, A Di Venere, XJ Yi, CL Hou, HC Wang, John B Ketterson, and GK Wong. Semimetal-to-semiconductor transition in bismuth thin films. *Physical Review B*, 48(15):11431, 1993.

[142] T Hirahara, K Miyamoto, I Matsuda, T Kadono, A Kimura, T Nagao, G Bihlmayer, EV Chulkov, S Qiao, K Shimada, H Namatame, M Taniguchi, and S Hasegawa. Direct observation of spin splitting in bismuth surface states. *Physical Review B*, 76:153305, 2007.

[143] YM Koroteev, G Bihlmayer, JE Gayone, EV Chulkov, S Blügel, PM Echenique, and Ph Hofmann. Strong Spin-Orbit Splitting on Bi Surfaces. *Physical Review Letters*, 93:046403, 2004.

[144] T Hirahara, K Miyamoto, I Matsuda, T Kadono, A Kimura, T Nagao, G Bihlmayer, EV Chulkov, S Qiao, K Shimada, et al. Direct observation of spin splitting in bismuth surface states. *Physical Review B*, 76(15):153305, 2007.

[145] A Takayama, T Sato, S Souma, and T Takahashi. Giant out-of-plane spin component and the asymmetry of spin polarization in surface rashba states of bismuth thin film. *Physical Review Letters*, 106:166401, 2011.

[146] Zheng Liu, Chao-Xing Liu, Yong-Shi Wu, Wen-Hui Duan, Feng Liu, and Jian Wu. Stable nontrivial z_2 topology in ultrathin bi(111) films: a first-principles study. *Physical review letters*, 107(13):136805, 2011.

[147] Dongchao Wang, Li Chen, Hongmei Liu, and Xiaoli Wang. Electronic structures and topological properties of bi(111) ultrathin films. *Journal of the Physical Society of Japan*, 82(9):094712, 2013.

[148] T Hirahara, N Fukui, T Shirasawa, M Yamada, M Aitani, H Miyazaki, M Matsunami, S Kimura, T Takahashi, S Hasegawa, et al. Atomic and electronic structure of ultrathin bi(111) films grown on bi_2te_3(111) substrates: Evidence for a strain-induced topological phase transition. *Physical review letters*, 109(22):227401, 2012.

[149] Toru Hirahara, Gustav Bihlmayer, Yusuke Sakamoto, Manabu Yamada, Hidetoshi Miyazaki, Shin-ichi Kimura, Stefan Blügel, and Shuji Hasegawa. Interfacing 2d and 3d topological insulators: Bi(111) bilayer on bi_2te_3. *Physical review letters*, 107(16):166801, 2011.

[150] MY Yao, F Zhu, CQ Han, DD Guan, C Liu, D Qian, and J Jia. Topologically nontrivial bismuth (111) thin films. *Scientific Reports*, 6, 2016.

[151] Suguru Ito, Bao-jie Feng, Masashi Arita, Akari Takayama, R-Y Liu, Takashi Someya, W-C Chen, Takushi Iimori, Hirofumi Namatame, Masaki Taniguchi, et al. Proving nontrivial topology of pure bismuth by quantum confinement. *Physical review letters*, 117(23):236402, 2016.

[152] D Hsieh, Y Xia, D Qian, L Wray, JH Dil, F Meier, J Osterwalder, L Patthey, JG Checkelsky, and NP Ong. A tunable topological insulator in the spin helical Dirac transport regime. *Nature*, 460(7259):1101–1105, 2009.

[153] Anna Pertsova and Carlo M Canali. Probing the wavefunction of the surface states in Bi_2Se_3 topological insulator: a realistic tight-binding approach. *New Journal of Physics*, 16(6):063022, 2014.

[154] Yi Zhang, Ke He, Cui-Zu Chang, Can-Li Song, Li-Li Wang, Xi Chen, Jin-Feng Jia, Zhong Fang, Xi Dai, Wen-Yu Shan, et al. Crossover of the three-dimensional topological insulator Bi_2Se_3 to the two-dimensional limit. *Nature Physics*, 6(8):584–588, 2010.

[155] Oleg V Yazyev, Joel E Moore, and Steven G Louie. Spin polarization and transport of surface states in the topological insulators Bi_2Se_3 and Bi_2Te_3 from first principles. *Physical review letters*, 105(26):266806, 2010.

[156] Z-H Pan, E Vescovo, AV Fedorov, D Gardner, YS Lee, S Chu, GD Gu, and T Valla. Electronic structure of the topological insulator Bi_2Se_3 using angle-resolved photoemission spectroscopy: evidence for a nearly full surface spin polarization. *Physical review letters*, 106(25):257004, 2011.

[157] H Zhang, CX Liu, and SC Zhang. Spin-orbital texture in topological insulators. *Physical Review Letters*, 111:066801, 2013.

[158] Y Cao, JA Waugh, XW Zhang, JW Luo, Q Wang, TJ Reber, SK Mo, Z Xu, A Yang, and J Schneeloch. Mapping the orbital wavefunction of the surface states in three-dimensional topological insulators. *Nature Physics*, 9(8):499–504, 2013.

[159] K Yaji, K Kuroda, S Toyohisa, A Harasawa, Y Ishida, S Watanabe, C Chen, K Kobayashi, F Komori, and S Shin. Spin-dependent quantum interference in photoemission process from spin-orbit coupled states. *Nature Communications*, 8, 2017.

[160] Kenta Kuroda, Masashi Arita, Koji Miyamoto, Mao Ye, Jian Jiang, Akio Kimura, EE Krasovskii, EV Chulkov, Hideaki Iwasawa, Taichi Okuda, et al. Hexagonally deformed fermi surface of the 3d topological insulator Bi_2Se_3. *Physical review letters*, 105(7):076802, 2010.

[161] YH Wang, D Hsieh, D Pilon, L Fu, DR Gardner, YS Lee, and N Gedik. Observation of a warped helical spin texture in Bi_2 Se_3 from circular dichroism angle-resolved photoemission spectroscopy. *Physical Review Letters*, 107(20):207602, 2011.

[162] JA Sobota, SL Yang, AF Kemper, JJ Lee, FT Schmitt, W Li, RG Moore, JG Analytis, IR Fisher, and PS Kirchmann. Direct optical coupling to an unoccupied dirac surface state in the topological insulator Bi_2Se_3. *Physical Review Letters*, 111(13):136802, 2013.

[163] HM Benia, A Yaresko, AP Schnyder, J Henk, CT Lin, K Kern, and CR Ast. Origin of rashba splitting in the quantized subbands at the bi_2se_3 surface. *Physical Review B*, 88(8):081103, 2013.

[164] MS Bahramy, PDC King, Alberto De La Torre, J Chang, M Shi, L Patthey, Geetha Balakrishnan, Ph Hofmann, R Arita, N Nagaosa, et al. Emergent quantum confinement at topological insulator surfaces. *Nature communications*, 3(1):1–7, 2012.

[165] C Cacho, A Crepaldi, M Battiato, J Braun, F Cilento, M Zacchigna, MC Richter, O Heckmann, E Springate, Y Liu, et al. Momentum-resolved spin dynamics of bulk and surface excited states in the topological insulator Bi_2Se_3. *Physical review letters*, 114(9):097401, 2015.

[166] Chris Jozwiak, Jonathan A Sobota, Kenneth Gotlieb, Alexander F Kemper, Costel R Rotundu, Robert J Birgeneau, Zahid Hussain, Dung-Hai Lee, Zhi-Xun Shen, and Alessandra Lanzara. Spin-polarized surface resonances accompanying topological surface state formation. *Nature communications*, 7(1):1–7, 2016.

[167] Siyuan Zhu, Yukiaki Ishida, Kenta Kuroda, Kazuki Sumida, Mao Ye, Jiajia Wang, Hong Pan, Masaki Taniguchi, Shan Qiao, Shik Shin, et al. Ultrafast electron dynamics at the dirac node of the topological insulator Sb_2Te_3. *Scientific reports*, 5:13213, 2015.

[168] Guang Wang, Xiegang Zhu, Jing Wen, Xi Chen, Ke He, Lili Wang, Xucun Ma, Ying Liu, Xi Dai, Zhong Fang, et al. Atomically smooth ultrathin films of topological insulator sb_2te_3. *Nano Research*, 3(12):874–880, 2010.

[169] C Pauly, G Bihlmayer, M Liebmann, M Grob, A Georgi, D Subramaniam, MR Scholz, J Sánchez-Barriga, A Varykhalov, S Blügel, et al. Probing two topological surface bands of Sb_2Te_3 by spin-polarized photoemission spectroscopy. *Physical Review B*, 86(23):235106, 2012.

[170] D Niesner, Th Fauster, SV Eremeev, TV Menshchikova, YM Koroteev, AP Protogenov, EV Chulkov, OE Tereshchenko, KA Kokh, and O Alekperov. Unoccupied topological states on bismuth chalcogenides. *Physical Review B*, 86(20):205403, 2012.

[171] J Sánchez-Barriga, M Battiato, M Krivenkov, E Golias, A Varykhalov, A Romualdi, LV Yashina, J Minár, O Kornilov, H Ebert, et al. Subpicosecond spin dynamics of excited states in the topological insulator Bi_2Te_3. *Physical Review B*, 95(12):125405, 2017.

[172] Jinsong Zhang, Cui-Zu Chang, Zuocheng Zhang, Jing Wen, Xiao Feng, Kang Li, Minhao Liu, Ke He, Lili Wang, Xi Chen, et al. Band structure engineering in $(Bi_{1-x}Sb_x)_2Te_3$ ternary topological insulators. *Nature communications*, 2(1):1–6, 2011.

[173] Desheng Kong, Yulin Chen, Judy J Cha, Qianfan Zhang, James G Analytis, Keji Lai, Zhongkai Liu, Seung Sae Hong, Kristie J Koski, Sung-Kwan Mo, et al. Ambipolar field effect in the ternary topological insulator $(Bi_xSb_{1-x})_2Te_3$ by composition tuning. *Nature nanotechnology*, 6(11):705, 2011.

[174] Carsten Schinke, P Christian Peest, Jan Schmidt, Rolf Brendel, Karsten Bothe, Malte R Vogt, Ingo Kröger, Stefan Winter, Alfred Schirmacher, Siew Lim, et al. Uncertainty analysis for the coefficient of band-to-band absorption of crystalline silicon. *Aip Advances*, 5(6):067168, 2015.

[175] Wolfgang SM Werner, Kathrin Glantschnig, and Claudia Ambrosch-Draxl. Optical constants and inelastic electron-scattering data for 17 elemental metals. *Journal of Physical and Chemical Reference Data*, 38(4):1013–1092, 2009.

[176] M Eddrief, Franck Vidal, and B Gallas. Optical properties of Bi_2Se_3: from bulk to ultrathin films. *Journal of Physics D: Applied Physics*, 49(50):505304, 2016.

[177] JW McIver, David Hsieh, Steven G Drapcho, Darius Hosseinzadeh Torchinsky, Dillon Richard Gardner, Young S Lee, and Nuh Gedik. Theoretical and experimental study of second harmonic generation from the surface of the topological insulator Bi_2Se_3. *Physical Review B*, 86(3):035327, 2012.

[178] Qiuzhang Zhang and Tianshu Luo. Based on the refractive angle method of complex refractive index measurement. *Optik*, 174:692–697, 2018.

[179] W Weber, SD Ganichev, SN Danilov, D Weiss, W Prettl, ZD Kvon, VV Bel'kov, LE Golub, HI Cho, and JH Lee. Demonstration of rashba spin splitting in GaN-based heterostructures. *Applied Physics Letters*, 87(26):262106, 2005.

[180] J Yu, Y Chen, S Cheng, and Y Lai. Spectra of circular and linear photogalvanic effect at inter-band excitation in $In_{0.15}Ga_{0.85}As/Al_{0.3}Ga_{0.7}As$ multiple quantum wells. *Physica E: Low-dimensional Systems and Nanostructures*, 49:92–96, 2013.

[181] P Olbrich, LE Golub, T Herrmann, SN Danilov, H Plank, VV Bel'kov, G Mussler, Ch Weyrich, CM Schneider, J Kampmeier, et al. Room-temperature high-frequency transport of dirac fermions in epitaxially grown Sb_2Te_3-and Bi_2Te_3-based topological insulators. *Physical review letters*, 113(9):096601, 2014.

[182] L He, F Xiu, Y Wang, AV Fedorov, G Huang, X Kou, M Lang, WP Beyermann, J Zou, and KL Wang. Epitaxial growth of Bi_2Se_3 topological insulator thin films on Si (111). *Journal of Applied Physics*, 109(10):103702, 2011.

[183] MH Xie, X Guo, ZJ Xu, and WK He. Molecular-beam epitaxy of topological insulator Bi_2Se_3 (111) and (221) thin films. *Chinese Physics B*, 6:011, 2013.

[184] CL Song, YL Wang, YP Jiang, Y Zhang, CZ Chang, L Wang, K He, X Chen, JF Jia, and Y Wang. Topological insulator Bi_2Se_3 thin films grown on double-layer graphene by molecular beam epitaxy. *Applied Physics Letters*, 97(14):143118, 2010.

[185] HD Li, ZY Wang, X Kan, Xinli Guo, HT He, Zichen Wang, JN Wang, TL Wong, Ning Wang, and Mao Hai Xie. The van der waals epitaxy of Bi_2Se_3 on the vicinal Si(111) surface: an approach for preparing high-quality thin films of a topological insulator. *New Journal of Physics*, 12(10):103038, 2010.

[186] Yusuke Sakamoto, Toru Hirahara, Hidetoshi Miyazaki, Shin-ichi Kimura, and Shuji Hasegawa. Spectroscopic evidence of a topological quantum phase transition in ultrathin Bi_2Se_3 films. *Physical Review B*, 81(16):165432, 2010.

[187] M Vyshnepolsky, C Klein, F Klasing, A Hanisch-Blicharski, and M Horn-von Hoegen. Epitaxial growth of the topological insulator Bi_2Se_3 on Si(111): Growth mode, lattice parameter, and strain state. *Applied Physics Letters*, 103(11):111909, 2013.

[188] AV Matetskiy, IA Kibirev, T Hirahara, S Hasegawa, AV Zotov, and AA Saranin. Direct observation of a gap opening in topological interface states of $MnSe/Bi_2Se_3$ heterostructure. *Applied Physics Letters*, 107(9):091604, 2015.

[189] XY Peng, Q Zhang, B Shen, JR Shi, CM Yin, XW He, FJ Xu, XQ Wang, N Tang, CY Jiang, et al. Anomalous linear photogalvanic effect observed in a gan-based two-dimensional electron gas. *Physical Review B*, 84(7):075341, 2011.

[190] Dong-Xia Qu, Xiaoyu Che, Xufeng Kou, Lei Pan, Jonathan Crowhurst, Michael R Armstrong, Jonathan Dubois, Kang L Wang, and George F Chapline. Anomalous helicity-dependent photocurrent in the topological insulator $(Bi_0.5Sb_0.5)_2Te_3$ on a GaAs substrate. *Physical Review B*, 97(4):045308, 2018.

[191] Gennady M Mikheev, Aleksandr S Saushin, Viatcheslav V Vanyukov, Konstantin G Mikheev, and Yuri P Svirko. Femtosecond circular photon drag effect in the ag/pd nanocomposite. *Nanoscale research letters*, 12(1):1–7, 2017.

[192] AS Ketterl, Sebastian Otto, M Bastian, Beatrice Andres, Cornelius Gahl, Jan Minár, Hubert Ebert, Jürgen Braun, Oleg Evgenievich Tereshchenko, Konstantin A Kokh, et al. Origin of spin-polarized photocurrents in the topological surface states of Bi_2Se_3. *Physical Review B*, 98(15):155406, 2018.

[193] Hadas Soifer, Alexandre Gauthier, Alexander F Kemper, Costel R Rotundu, S-L Yang, Hongyu Xiong, Donghui Lu, Makoto Hashimoto, Patrick S Kirchmann, Jonathan A Sobota, et al. Band-resolved imaging of photocurrent in a topological insulator. *Physical review letters*, 122(16):167401, 2019.

[194] Anatoly A Grinberg and Serge Luryi. Theory of the photon-drag effect in a two-dimensional electron gas. *Physical Review B*, 38(1):87, 1988.

[195] Madhab Neupane, Anthony Richardella, Jaime Sánchez-Barriga, SuYang Xu, Nasser Alidoust, Ilya Belopolski, Chang Liu, Guang Bian, Duming Zhang, Dmitry Marchenko, et al. Observation of quantum-tunnelling-modulated spin texture in ultrathin topological insulator Bi_2Se_3 films. *Nature communications*, 5(1):1–7, 2014.

[196] Nardeep Kumar, Brian A Ruzicka, NP Butch, P Syers, K Kirshenbaum, J Paglione, and Hui Zhao. Spatially resolved femtosecond pump-probe study of topological insulator bi_2se_3. *Physical Review B*, 83(23):235306, 2011.

[197] RV Shchelushkin and Arne Brataas. Spin Hall effects in diffusive normal metals. *Physical Review B*, 71(4):045123, 2005.

[198] Toru Hirahara, Yusuke Sakamoto, Yasuo Takeichi, Hidetoshi Miyazaki, Shin-ichi Kimura, Iwao Matsuda, Akito Kakizaki, and Shuji Hasegawa. Anomalous transport in an n-type topological insulator ultrathin Bi_2 Se_3 film. *Physical Review B*, 82(15):155309, 2010.

[199] Praveen Deorani, Jaesung Son, Karan Banerjee, Nikesh Koirala, Matthew Brahlek, Seongshik Oh, and Hyunsoo Yang. Observation of inverse spin Hall effect in bismuth selenide. *Physical Review B*, 90(9):094403, 2014.

[200] Paul Seifert, Kristina Vaklinova, Sergey Ganichev, Klaus Kern, Marko Burghard, and Alexander W Holleitner. Spin Hall photoconductance in a three-dimensional topological insulator at room temperature. *Nature communications*, 9(1):1–7, 2018.

[201] T Schumann, N Meyer, G Mussler, J Kampmeier, D Grützmacher, E Schmoranzerova, Lukas Braun, Tobias Kampfrath, J Walowski, and M Münzenberg. Observation of spin Nernst photocurrents in topological insulators. *arXiv preprint arXiv:1810.12799*, 2018.

[202] Pavan Hosur. Circular photogalvanic effect on topological insulator surfaces: Berry-curvature-dependent response. *Physical Review B*, 83(3):035309, 2011.

[203] Zhurun Ji, Gerui Liu, Zachariah Addison, Wenjing Liu, Peng Yu, Heng Gao, Zheng Liu, Andrew M Rappe, Charles L Kane, Eugene J Mele, et al. Spatially dispersive circular photogalvanic effect in a Weyl semimetal. *Nature materials*, page 1, 2019.

[204] YM Koroteev, G Bihlmayer, JE Gayone, EV Chulkov, S Blügel, PM Echenique, and Ph Hofmann. Strong spin-orbit splitting on Bi surfaces. *Physical Review Letters*, 93:046403, 2004.

[205] C Zucchetti, M-T Dau, F Bottegoni, C Vergnaud, T Guillet, Alain Marty, C Beigné, S Gambarelli, A Picone, A Calloni, et al. Tuning spin-charge interconversion with quantum confinement in ultrathin bismuth films. *Physical Review B*, 98(18):184418, 2018.

[206] Zhou Li and JP Carbotte. Hexagonal warping on spin texture, Hall conductivity, and circular dichroism of topological insulators. *Physical Review B*, 89(16):165420, 2014.

[207] Su-Yang Xu, Madhab Neupane, Chang Liu, Duming Zhang, Anthony Richardella, L Andrew Wray, Nasser Alidoust, Mats Leandersson, Thiagarajan Balasubramanian, Jaime Sánchez-Barriga, et al. Hedgehog spin texture and Berry's phase tuning in a magnetic topological insulator. *Nature Physics*, 8(8):616–622, 2012.